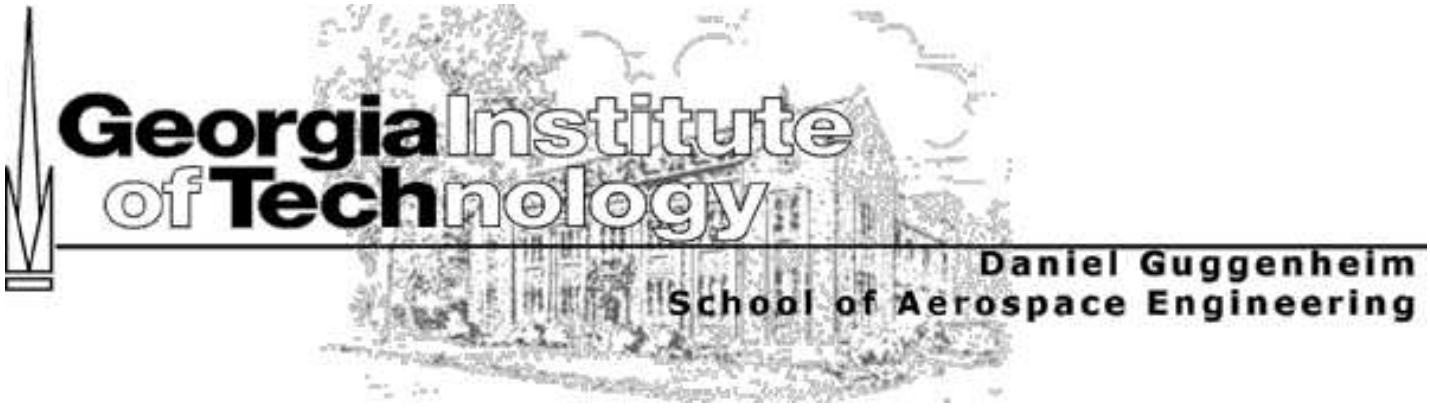

CCL Report CCL-TR-07-02

Two-level Simulations of High-Reynolds Number Wall-Bounded Shear Flows

Konstantin A. Kemenov, Ayse G. Gungor and Suresh Menon

Computational Combustion Laboratory
School of Aerospace Engineering
Georgia Institute of Technology
270 Ferst Drive
Atlanta, Georgia 30332-0150
http://www.ccl.gatech.edu

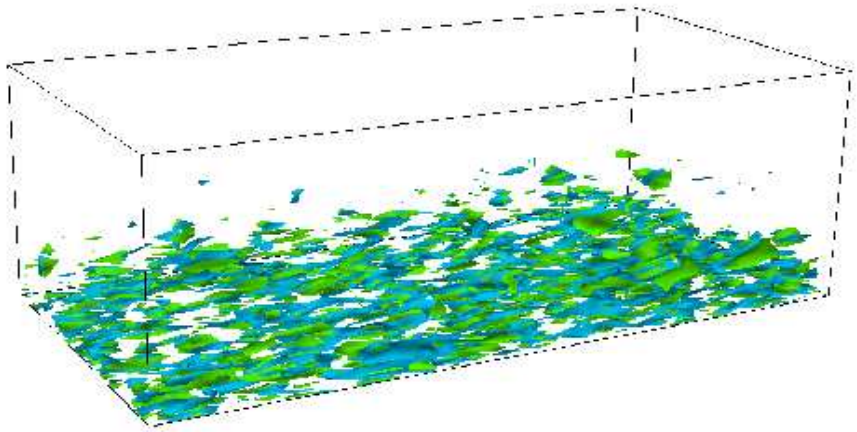

Sponsored by: *Office of Naval Research*
Contract Number: *N00014-03-1-0109*
Date: *February 2007*

TABLE OF CONTENTS

LIST OF FIGURES

LIST OF TABLES

CHAPTER I

INTRODUCTION

1.1 Background

Turbulent flows are widespread in nature and play an important role in engineering and earth science applications. In spite of a century of research efforts by engineers, physicists and mathematicians, our complete understanding of turbulent "laws" still remains elusive ([1]). On the other hand, engineers and scientists have been facing growing challenge to fully account for turbulent flow features, owing to the need for more efficient engineering designs or more accurate physical predictions.

Starting from the pioneering work of [2], numerical experiments with Navier-Stokes equations, or Direct Numerical Simulation (DNS), have become a major tool for studying the fundamental structure of turbulence. DNS of turbulent flows is computationally expensive because of the resolution requirement needed to accurately represent the whole range dynamically important scales. Even with the advent of massively parallel computers, DNS is still limited to relatively low Reynolds number (from engineering perspective) turbulent flows in particular simple geometries ([3], [4], [5]). Over thirty years, there has been a steady rise, in terms of the attainable Reynolds (Re) number, in DNS capabilities to simulate turbulent flows, largely as a result of the growth in computation power. The Reynolds number Re_λ, based on the Taylor microscale ($Re_\lambda \sim \sqrt{15}Re^{1/2}$), has increased from 35 in the work of Orszag and Patterson to 1217 in the simulation of [3]. The latter work, however, required the power of the Earth Simulator - a massively parallel 16.4 teraflop computer system, and the resolution of 4096^3 grid points. Nevertheless, the maximum value of the Reynolds number which is within the DNS reach, is still significantly below values ($Re \approx 10^5 - 10^8$) that typical for engineering applications.

Large eddy simulation (LES) approach, where only large, energy containing scales are simulated by Navier-Stokes like looking dynamic equations and the effect of the rest scales are modeled, has been at frontier of high Reynolds (Re) number turbulent research for long time. In LES the large scales are separated with help of filtering operation applied to the Navier-Stokes equations and the major effort is concentrated on modeling of the residual stress in terms of the large-scale (resolved) velocity (see, for example, recent reviews by [6] and [7]). The residual stress is usually referred as the subfilter stress (SFS), or the subgrid stress (SGS) depending on the meaning of the filtering operation. Proved to be very successfully for classical geometrically simple flows, LES has been still waiting to live up to expectations to be a viable method to simulate high-Re number complex industrial flows ([8]). In addition, traditional subgrid modeling always employs empirical arguments about unresolved velocity field, such as isotropy, and requires an introduction of arbitrary

model parameters. Most subgrid models possess different shortcomings such as inability to accommodate backscatter of energy, excessive dissipation in the presence of large coherent structures, poor correlation with real stresses, to name a few ([9]). To further discuss motivation of the current work, some limitations of LES approach are highlighted first in the following Section 1.2.

1.2 Motivation

LES aims to describe the dynamics of the large-scale (filtered) fields which are usually obtained by applying a filter to the actual fields to filter out the small-scales of the flow. For example, the filtered velocity is defined as:

$$\bar{u}_i(\mathbf{x}) = \int_\Omega u_i(\mathbf{y}) G(\mathbf{x}-\mathbf{y}, \Delta) \mathrm{d}\mathbf{y}, \quad \mathbf{x}, \mathbf{y} \in \Omega \subset \mathbb{R}^3, \tag{1.1}$$

Here, Δ is the filter width and Ω is flow domain. However the filtering procedure, being a convolution integral operation, introduces unclosed terms in the LES equations which results in a complex task of creating a suitable model for the residual stress. In addition to unavoidable phenomenology introduced by the residual stress model parameters, the filtering also creates extra difficulties associated with non-commutation of the filtering operation with spatial differentiation if the filter width is not uniform ([10, 11]). This makes it problematic to derive LES equations in consistent way without invoking additional assumptions. It is also very difficult to relate the statistics of the filtered fields to the statistics of the experimental or direct numerical simulation data ([12, 13]). Besides, majority of practical LES applications do not use explicit filtering in the numerical integration of the filtered governing equation. It is tacitly assumed that the discrete grid representation of the flow variables can be viewed as implicitly 'grid filtered', i.e., $\tilde{u}_i$, where tilde denotes implicit filtering ([14]). The implicit filtering operation can not be expressed in closed analytical form and depends on the underling grid.

Assuming that filtering and differentiation commutes, which is true only for constant width explicit filters in infinite or periodic domains, non-commutation between filtering and product operations gives rise to the introduction of the residual stress $\tau_{ij} = \overline{u_i u_j} - \bar{u}_i \bar{u}_j$ into the LES equations. This stress can be viewed as the commutator between filtering and product operations acting on the total velocity field u_i ([15, 16]). This residual stress is assumed to be computable during numerical simulations and needs to be modeled in terms of the resolved velocity $\tau_{ij}(\bar{u}_i)$ in order to close the LES equations. However, as it was pointed out in a number of recent works of [12, 17, 18], the replacement of $\overline{u_i u_j}$ by $\bar{u}_i \bar{u}_j + \tau_{ij}$ automatically leads to a mathematical inconsistency. This is because the convective product term $\bar{u}_i \bar{u}_j$ has the spectral support bigger than any other term in the filtered Navier-Stokes equations. As a result, the high wave number modes generated due to the non-linear interaction and extended beyond the smallest resolvable LES scale can not be fully computed by the LES equations. In spectral space, the convective product term $\bar{u}_i \bar{u}_j$ is represented by the convolution of spectral velocity with itself, and therefore, has twice bigger spectral

support than the filtered velocity $\bar{u}_i$ ([19]). As a result, in practical computations the high wave-number modes can alias back to the resolved part of the spectrum producing undesirable effects on the dynamics of the resolved turbulent scales. To alleviate this inconsistency and to retain the spectral content of the convective product term an additional explicit filtering is suggested in the form $\tau'_{ij} = \overline{u_i u_j} - \overline{\bar{u}_i \bar{u}_j}$. Additional explicit filtering has clear advantages over the implicit filtering allowing better control of the numerical error and consistent comparison of the LES results with the filtered DNS or experimental data ([17, 18]). However, there are still drawbacks of the explicit filtering approach. In addition to the higher computational cost, the new representation of the residual stress τ'_{ij} is not Galilean invariant unless the imposed filter is a spectral cut-off filter ([20, 17]). This effectively diminishes the capabilities of the explicit filtered LES to study turbulent flows in complex geometries, when finite volume or finite difference schemes are employed.

To accommodate the implicit filtering action of the grid into continuous LES equation the formal superposition of explicit and implicit filtering is usually considered which leads to the doubly filtered Navier-Stokes equations for $\tilde{\bar{u}}_i$ and $\tilde{\bar{p}}$ ([15]). Formally consistent, double filtering produces new types of stresses in the total residual stress decomposition. Indeed, the total residual stress arising from the double filtering can be written as a sum of sub-grid large scale stress (SGLS) and the grid filtered sub-filter stress (GFSFS), i.e., $\tilde{\bar{\tau}}_{ij} = \tilde{\bar{\sigma}}_{ij} + \widetilde{\overline{T}}_{ij}$, where $\tilde{\bar{\sigma}}_{ij} = \widetilde{\overline{\bar{u}_j \bar{u}_k}} - \widetilde{\tilde{\bar{u}}_j \tilde{\bar{u}}_k}$ and $\widetilde{\overline{T}}_{ij} = \widetilde{\overline{u_j u_k}} - \widetilde{\overline{\bar{u}_j \bar{u}_k}}$ (see, for example [18]). This procedure requires triple and quadruple filtering application which set additional challenges for viable modeling of the residual stresses. Furthermore, in practical application of the explicit filtering, in order to clean the highest wave number contributions, the explicit filtering is superimposed onto the implicit filtering which requires additional assumptions that the explicit and implicit filtering commute, i.e. $\tilde{\bar{u}}_i = \bar{\tilde{u}}_i$ ([15]).

There is yet another "non-commutative" feature of the filtering operation, which has received very little attention in the LES literature. In general, the filtering operation does not commute with differentiation unless the filter width is constant. Evidently, such filters are not well suited for LES studies of geometrically complex turbulent flows where high turbulence regions may coexist with weakly turbulent or laminar regions. Most works in this direction have been focused on two major approaches: the construction of explicit filters which can commute with differentiation, at least up to the order of accuracy of the numerical scheme, and the explicit adding of the non-commutation terms into the filtered Navier-Stokes equation. [21] proposed an explicit filtering scheme that results in the additional commutation terms which are of the second order with respect to the filter width. The construction of commutative non-uniform filters was further addressed by [22] and [20]. The later work uses mapping of the non-uniform grid in physical domain to the uniform grid in computational domain where the constant-width filtering can be performed. This approach was further generalized by [23] to construct commutative filters for unstructured grids. The second approach has received attention in the recent work of [16] who proposed the general LES equations with included non-commutative terms. The

authors emphasized, contrary to approaches which are based on the commutative filter construction, that the non-commutative terms do not vanish for any non-uniform filter and have to be accounted and modeled explicitly. However, the explicit adding of the non-commutation terms into the filtered Navier-Stokes system not only would complicate the LES equations but also would require additional modeling of these new terms analogous to the modeling of the residual stresses. A challenging task of modeling of the non-commutation terms has been further addressed in the work of [24].

Accounting for these new unclosed terms adds extra challenges to the LES methodology when modeling of the near-wall turbulence is required. This area is especially critical for LES in order to become a viable predictive tool for high-Re number engineering flows. The key difficulties originate in the presence of quasi-streamwise and hairpin vortices that play a dominant dynamic role in the near-wall turbulence. To resolve these structures, a fine (comparable to DNS) grid resolution is required not only in wall normal direction but also in the spanwise and streamwise direction. Computational complexity of resolving the wall layer (minimal number of the resolved scales) is Reynolds number dependent, and scales approximately as $Re^{1.8}$ ([25]). So far, most subgrid models perform poorly in the near-wall region when the grid resolution allows practically achievable computations.

Giving the facts that the filtering leads to extra assumptions in the derivation of the LES equations, as well as difficulties in their implementation at discrete level, it is therefore, not well suited framework for geometrically complex turbulent flows. The major objective of this work is to propose a framework which requires the least modeling efforts and allows treatment of complex geometry without adopting major assumptions or adding extra terms in the large-scale governing equations. Under the proposed framework the continuous large-scale equations are formulated without explicitly resorting to or using the classical LES filtering approach. Some earlier attempts of applying the current approach to simulate turbulent non-homogeneous flows, such as mixing layers or a channel flow, were reported elsewhere ([26, 27]).

1.3 Outline

This report is organized as follows:

- Chapter 2 summarizes the key technical objectives of this report.
- Chapter 3 provides a brief introduction to the existing decomposition methods that serve as alternatives to the standard LES or DNS approaches. Some limitations that may prevent these methods to be extended to simulate turbulent flows in complex geometries are discussed.
- In Chapter 4, the large-scale and small-scale governing equations are formulated without invoking the concept of filtering. It is shown that if the large-scale field is defined as the filtered quantity, then the large-scale equations produce the standard LES equations. Furthermore, to reduce computational complexity,

the 3D small-scale equations are introduced on a family of 1D lines. Such a representation requires modeling of the transverse small-scale velocity gradients on the lines. A simple model that is based on *a priori* analysis of the DNS data sets is proposed and its implications are discussed. Finally, numerical algorithm for the coupled integration of the large-scale and the simplified small-scale governing equations is presented.

- Chapter 5 gives a background information on the numerical methods employed for integration of the large-scale and the small-scale governing equations.

- Chapter 6 describes in detail the application of the current methodology to different types of turbulent flows. A particular simple case of the randomly forced 1D Burgers equation is discussed first, with a focus on the small-scale solution. The Burgers equation remains a popular toy model for testing turbulence theories of Navier-Stokes equations. Being different in physics, the Burgers turbulence possesses some general turbulent properties like nonlinear redistribution of energy over range of scales, dissipation of energy at small scales due to viscosity, and intermittency. The Burgers turbulence provides a case where the small-scale equation can be studied without any modeling assumptions. Here, the effects of neglecting various non-linear small-scale terms on the small-scale solution are discussed also. The current approach is further tested by a simulation of the forced homogeneous and isotropic turbulence. Non-homogeneous turbulence of the well developed channel flow and the temporal mixing layer provides other benchmark cases for evaluating capabilities of the current approach. These cases are discussed in the last two sections of Chapter 6.

- Chapter 7 describes the coupling of the TLS and LES approaches and implementation of this hybrid TLS-LES model for near-wall applications.

- Chapter 8 presents the results for turbulent channel flow and three-dimensional bump flow obtained by the hybrid TLS-LES model.

- Chapter 9 contains concluding remarks, and Chapter 10 outlines possible directions for the future research.

CHAPTER II

TECHNICAL OBJECTIVES

The key technical objectives of this two-year (FY05-FY06) research are:

- To develop a mathematically consistent two-scale modeling approach to simulate both the large-scale and small-scale flow field within a single formulation.

  This objective was succesfully achieved in FY06 [28, 29]. The mathematical formulation and the details of the model is described in the next section.

- To apply the TLS method to high Re wall-bounded flows and demonstrate its ability.

  Results are discussed here for high Re channel flows [29, 30].

- To apply the TLS method to high Re flows without walls to demonstrate its generality.

  Results obtained in high-Re isotropic turbulence and mixing layers are reported here[29, 28, 30].

- To investigate and develop advanced near-wall modeling approach for wall-bounded flows based on the TLS approach.

  Accurate modeling of the near-wall region constitutes the most difficult problem for LES. The maximum production of turbulent kinetic energy occurs in the inner layer where, very high resolution is needed to accurately predict the small but dynamically important eddies in the near-wall region. Most popular methods to overcome this problem very often fail to represent the correct near-wall dynamics when the two way inner/outer layer interactions are present.

  A new approach is to apply TLS as a near-wall LES sub-grid closure in order to increase accuracy of near-wall turbulence, which is able to produce DNS-comparable results for real engineering flow applications but with less costly computational resources using DNS.

  The first step towards the achievement of this goal is the generalization of TLS equations for compressible flows. The mathematical formulation of compressible TLS equations and coupled TLS-LES equations are described here.

- To validate the capabilities of TLS-LES approach for wall-bounded turbulence.

  The fully-developed turbulent channel flow for a range of Reynolds numbers is analyzed for this purpose. Detailed analysis of TLS-LES results are reported here[31, 32].

- To demonstrate capabilities and limitations of TLS-LES approach for flows around complex geometries at high Reynolds number.

  These types of flows contain the complex phenomena with unsteady separations and reattachments, wakes and vortex interactions. This task focused on the high Reynolds number flow past a spherical bumps recently studied by Simpson et al.[33] and simulated using the more conventional localized dynamic LES model[34].

  The effect of the near-wall TLS-LES approach is analyzed in terms of accuracy of prediction versus measured data and computational cost. The preliminary results are reported here[32].

CHAPTER III

DECOMPOSITION METHODS FOR TURBULENT FLOWS

3.1 Introduction

The current approach, called Two Level Simulation (TLS), does not require explicit or implicit filtering, and provides more freedom to describe the contribution of the unresolved (small-scales) scales. It can be related to multiscale decomposition methods. In these methods the total flow fields (for example velocity) are decomposed into the large-scale (resolved) and the small-scale (unresolved) components:

$$u_i = u_i^L + u_i^S, \tag{3.1}$$

and then the coupled system of the large-scale and small-scale governing equations is derived.

Multiscale description of turbulent flows have been proposed recently by several authors including, among others, [35] as the Additive Turbulent Decomposition approach; [36], [37], [38] as the Dynamic Multilevel Method; [39], [40], [41] as the Variational Multiscale Method; [42], [43], [44] as the Rapid Distortion Theory model.

3.2 Overview of Existing Approaches

Most of these multiscale methods, with the exception of the Rapid Distortion Theory (RDT) model, adopt the weak formulation of the Navier-Stokes equations, which allows to view the large-scale field as a projection on a subspace spanned by the first elements of the adopted functional basis, and the small-scale field as a projection on the compliment subspace. The common feature of these methods is the derivation of the small-scale governing equation which is needed for explicit computation of the small scales. As the result, the large-scale equation can be treated as closed, since the residual stress is directly computable once the small-scale field is known.

The full coupled simulation of the large-scale and the small-scale governing equations is clearly computationally not viable since it will require DNS-like resolution to accurately represent the small-scale motions. Therefore, some physical reasoning is usually invoked to simplify the small-scale governing equation and make it computationally tractable. For example, in the RDT model the scales are separated using standard LES filtering, and the small-scale equation is derived by subtraction of the filtered (large-scale) equation from the full Navier-Stokes equation. The small-scale equation can be simplified further by retaining only the nonlinear products of the large-scale and the small-scale velocities, while all other product terms can be modeled using a turbulent viscosity and stochastic forcing, which leads to the linear form

of the small-scale equation and resembles the RDT equation ([42]). The approach was applied to study several cases of 2D turbulent flows as well as more complex case of the 3D decaying, isotropic turbulence, though in spectral representation. Simultaneous numerical treatment of the coupled large-scale and the small-scale equations led to an increase in computational time by a factor of 3 (!) over standard DNS ([43]). The linear structure of the small-scale RDT equation was further exploited by implementing the Lagrangian time integration scheme to the Gabor transformed form of the small-scale equation ([45]). Such procedure resulted in substantial saving in computational time (up to a factor of 100) for 2D turbulent simulation compared DNS. However, in spite of the simplified linear structure of the small-scale RDT equation, it still remains to be seen if the model would be applicable to treat non-homogeneous turbulent flows in complex geometries.

Another class of multiscale numerical strategies referred as the Dynamic Multilevel Methods (DML) originates from the dynamical systems theory and the utilizes the mathematical concept of approximate inertial manifold (AIM) that can be introduced to approximate the attractor of Navier-Stokes equations ([46]). Qualitatively, it can be thought as a state where the small-scales are slaved to the large-scales leading to an approximate relation (slaving law) $u_i^S = \Psi(u_i^L)$ which defines the AIM of the Navier-Stokes system in the infinite-dimensional phase space. Simplification of the small-scale equation based on physical grounds ([47, 48]), and obtained by neglecting the non-stationary term, the mixed large-scale/small-scale term and the mutual small-scale product term, leads to a relation for the AIM providing the closure for the large-scale dynamic equations. The DML approach has been developed and applied to simulation of 2D and 3D turbulent flows by [36, 37, 38], and resulted in the reduction of computational time up to a factor of 3 compared to DNS. However, most DML applications have been implemented in spectral space for homogeneous isotropic flows in periodic domains. Spectral extension of the DML to treat non-homogeneous direction in turbulent channel flow has been reported by [49]). Based on results of this work the authors suggest that the DML needs to be replaced by the multi-domain decomposition technique to separate scales in order to treat flow in complex geometries.

Recognizing high computational cost of the explicit simulation of the small-scale equation, a different approach was adopted by [39] in developing the Variational Multiscale Method (VMS). Instead of resolving all dynamically relevant small-scale motions, the small-scale equation is solved on a relatively coarse grid, while the "unresolved" part of the small-scale residual stress is modeled by using the Smagorinsky eddy viscosity model. To separate the scales, the large-scale equation is treated on an even coarser grid, for example twice coarser grid. Thus, in the VMS approach all modeling is confined to the small-scales equations only, while the large-scale equations are closed ([39]). However, as it was pointed out by [50], this is only partially true. Clearly, since the small-scales are represented by resolved modes, the unresolved portion of the small-scales still affect the large scales, and therefore corresponding terms requires modeling rather than being neglected. The spectral VMS method with the Smagorinsky model has been successfully applied to simulate 3D decaying isotropic turbulence ([40]) and low Reynolds number 2D turbulent channel flow ([41]).

The other possible drawbacks of the VMS approach are worth mentioning. First, adding non-linear viscosity term, in the form of the Smagorinsky model, to the small-scale equations ensure extra dissipation at the small scales, but suppress a possible backscattering of energy at the grid cut-off level, i.e., from the unresolved small-scales to the resolved small-scales. This may be important for complex, wall-bounded flows, especially taking into account that the small-scale equations is solved on a relatively coarse grid. Second, it is difficult to decide how coarse the resolution of the large-scale grid should be relative to that of the small-scale grid which is already coarse and limited by computational cost. If the large-scale grid is too coarse, the small-scale equations, which is forced by the large-scales, may lead to unphysical small-scale solution. Finally, an extension of the VMS method for finite volume or finite difference codes implemented in physical, rather than spectral space, is a very non-trivial task. Being formulated in the weak sense, the VMS method requires construction of the complete hierarchical functional bases in physical space to separate scales by projection, which is difficult to reconcile with the finite volume or finite difference discrete representation.

The present (TLS) approach follows the general logic of multiscale decomposition methods assuming that flow fields are split into the large-scale and the small-scale components. However, they are two major distinctions from others multi-scale methodologies. The TLS governing equations are formulated in the strong sense, i.e., without resorting to integral form representation over corresponding trial functional spaces, and do not use notion of filtering to separate scales. Instead, the large-scale fields are defined based on an underlying coarse grid. This makes the approach easily adaptable for the finite volume and finite difference methods on geometrically complex, non-uniform grids. In order to reduce computational costs the small-scale equations are solved on a "reduced" 3D domain, rather than the full 3D flow domain. This domain represents a collection of intersecting lines embedded in the 3D domain. As a result, the small-scale governing equations along these lines can be treated in a parallel fashion, making the TLS approach computationally feasible.

CHAPTER IV

MATHEMATICAL FORMULATION

4.1 Decomposition of Governing Equations

Decomposition approach is quite common in derivation of various governing equations in fluid mechanics ranging from acoustics equations to Reynolds averaged equations for turbulent flows. Here, we consider a case of the incompressible turbulent flow with uniform density ρ which can be described by velocity and pressure fields (u_i, p) and governed by Navier-Stokes equations in 3D domain Ω.

$$\frac{\partial u_i}{\partial t} + \frac{\partial u_i u_j}{\partial x_j} = -\frac{1}{\rho}\frac{\partial p}{\partial x_i} + \nu \frac{\partial^2 u_i}{\partial x_j^2}, \quad \frac{\partial u_i}{\partial x_i} = 0 \tag{4.1}$$

To ease further notations, we also drop density in the pressure gradient term assuming that it is included in the pressure field. When kinematic viscosity $\nu = \mu/\rho$, characteristic length L and velocity U scales of a problem are such that the Reynolds number $Re = UL/\nu$ is sufficiently high then the flow is turbulent. The challenge here is to demonstrate a computationally feasible method that can be used to simulate high-Re flows.

In the LES approach, the grid resolution requirement can be substantially lowered by considering filtered fields $(\bar{u}_i, \bar{p})$. However, the large-scale field can also be obtained without using filters. A discrete LES approach, which based on sampling of the total velocity instead of filtering has been proposed by [51] and alleviates some difficulties of the traditional LES. Very often in practical computations or experiments, flow field is known on the coarse (large-scale) grid and can be thought of as the approximations to the sampled values of the true flow fields (u_i, p). Clearly, such an interpretation of the large-scale velocity is more consistent with probe measurement in experiments than the filtered velocity field.

In order to formulate TLS governing equations without invoking a concept of filtering, a class of the large-scale (LS) functions $mathcalF^L$ is introduced first. Any LS quantity which belongs to this class is denoted by superscript L, i.e., $u_i^L \in \mathcal{F}^L$ represents the LS velocity. Before defining the main property of the class $\mathcal{F}^L$, we present two examples of the LS functions which can be viewed as members of $\mathcal{F}^L$. The first one is the filtered LES velocity defined by Eq. (1.1). The second example can be constructed based on the underlying LS grid G^Δ and the total velocity u_i with help of the LS operator $\mathcal{L}^\Delta$:

$$u_i^L(\mathbf{x}) = \mathcal{L}^\Delta u_i(\mathbf{x}) = \mathcal{I}^\Delta \circ \mathcal{S}^\Delta[u_i(\mathbf{x})], \tag{4.2}$$

$$\mathcal{S}^\Delta : u_i(\mathbf{x}) \longrightarrow u_i^L(\mathbf{x}_\mathrm{k}), \quad \mathcal{I}^\Delta : u_i^L(\mathbf{x}_\mathrm{k}) \longrightarrow u_i^L(\mathbf{x}),$$

$$\mathbf{x}_\mathrm{k} \in G^\Delta \equiv \{\mathbf{x}_1, \ldots, \mathbf{x}_N\} \subset \Omega$$

Here, $\mathcal{S}^\Delta$ is a local averaging operator, $\mathcal{I}^\Delta$ is analogous to interpolation operator and acts on discrete function $u_i^L(\mathbf{x}_\mathrm{k})$ mapping it to continuous LS velocity $u_i^L(\mathbf{x})$. The local averaging operator $\mathcal{S}^\Delta$ can be quite general and time dependent. It depends on the LS grid G^Δ and the algorithm how the discrete LS value is actually obtained. The simplest case of $\mathcal{S}^\Delta$ is the sampling operator when the LS velocity values is defined as the velocity values at the nodes of G^Δ, i.e., $u_i^L(\mathbf{x}_\mathrm{k}) = u_i(\mathbf{x}_\mathrm{k})$. In more complex cases, the local averaging over some line directions (one or several) or volume can be applied. The LS quantity given by Eq. (4.2) is unique when the averaging operator $\mathcal{S}^\Delta$ and the operator $\mathcal{I}^\Delta$ are fixed. In terms of "degrees of freedom" this construction is similar to traditional filtering, since the filtered field is also defined uniquely when two parameters are specified (the functional form of filter G and the filter width Δ). However, the construction (4.2) is more versatile since it can allow non-uniform grids with different local clustering, thus resolving different range of scales in various parts of the flow domain.

There are infinite number of possibilities to define $\mathcal{L}^\Delta$, and generally, its exact structure is not known. Therefore, a class $\mathcal{F}^L$ is not defined based on operator form as given by Eq. (4.2) or (1.1). In addition, $\mathcal{F}^L$ may contain some other LS fields which can not be represented in operator form, whether they are obtained by convolution with a filter or by means of a composite operator $\mathcal{L}^\Delta$. Instead, we will assume that for a given LS grid G^Δ, $\mathcal{F}^L \subset \mathbb{C}^n\big[\Omega \times (0,\infty)\big]$ and consist of fields with "approximately" bounded spectral support. That means that the spectral energy content of the second derivative of the LS field decays sufficiently fast beyond the maximal grid resolvable mode k_Δ such that we can consider the LS field and its derivatives (first and second) to have the same support. This assumption can be motivated by the fact that differentiation in physical space is equivalent to multiplication by wavenumber k in a spectral space, and therefore it does not enlarge the spectral support (as oppose to product operation) but merely amplify the energy content of the smallest modes.

A class of the LS fields $\mathcal{F}^L$ gives rise to a class of the the small-scale (SS) fields $\mathcal{F}^S$ based on decomposition:

$$u_i^S = u_i - u_i^L, \quad p^S = p - p^L \tag{4.3}$$

In other words, for any LS field $u_i^L \in \mathcal{F}^L$ the difference $u_i - u_i^L \in \mathcal{F}^S$ is considered to be the SS field and denoted by superscript S.

In spectral space, the SS field, being the complement to the total field, dominates dynamically (relative to the LS field) for modes beyond k_Δ. There also exists a δ-region around k_Δ, which corresponds to the smallest LS eddy size, where the SS field is energetically comparable with the LS field. Schematically it can be written as:

$$\begin{cases} e^L(k) \gg e^S(k), & k < k_\Delta - \delta/2, \\ e^L(k) \approx e^S(k), & k_\Delta - \delta/2 < k < k_\Delta + \delta/2, \\ e^L(k) \ll e^S(k), & k > k_\Delta + \delta/2 \end{cases}$$

where e^L and e^S are spectral energies of the LS and the SS fields. This is further illustrated in Fig. 4.1 for the case of isotropic turbulence. The LS field is explicitly computed based on 32^3 uniform grid from a forced isotropic DNS data set given

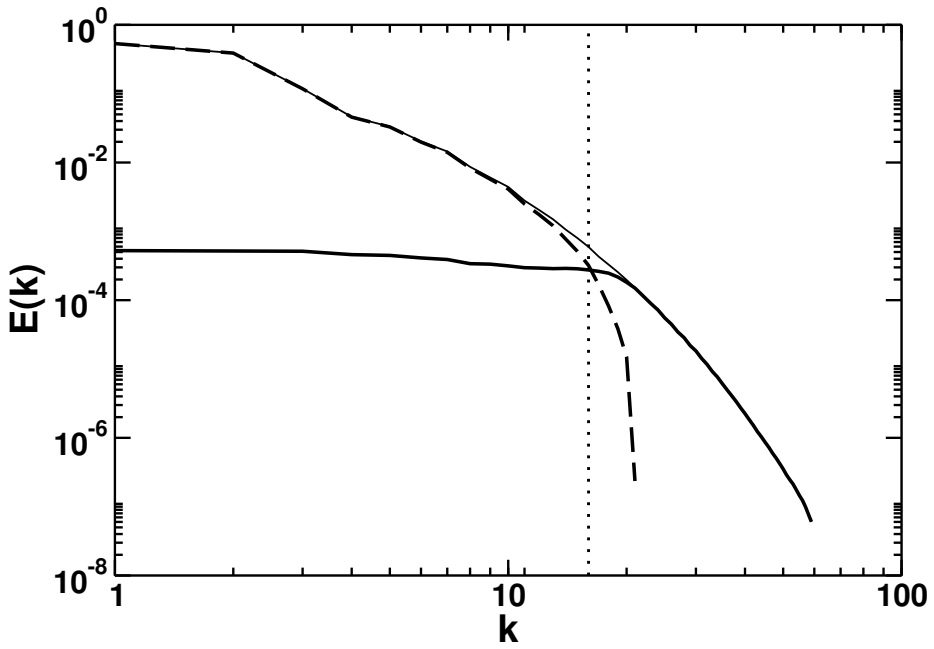

Figure 4.1: SS energy (solid line), LS energy (dashed line) and total DNS energy (thin solid line) spectra for the case of isotropic turbulence. Maximal grid resolvable mode k_Δ is shown by dotted vertical line.

on 128^3 grid ([52]). The operator $\mathcal{S}^\Delta$ is the averaging along three orthogonal lines parallel to coordinates and intersecting at the LS grid cell. The operator $\mathcal{I}^\Delta$ is chosen to be the cubic spline interpolation and extend the LS field onto the DNS grid. Note that this choice of the splitting produces the SS field such that the SS energy of the modes with $k<k_\Delta$ (LS modes) is greater then the SS energy of the modes with $k>k_\Delta$ which correspond to the SS motions. In case of non-homogeneous turbulence, when non-uniform grids are used, all considerations stay the same with the exception that the LS and the SS energies are functions in 3D spectral space, i.e. $e^L(k_1, k_2, k_3)$, $e^S(k_1, k_2, k_3)$ and k_Δ is defined as a closed surface $k_\Delta(k_1, k_2, k_3) = 0$. It is also clear that the SS field solely depends on the LS field through decomposition Eq. (4.3), and can be quite large and even comparable to the LS field in magnitude. Nevertheless, the notion of "small-scale" is consistently used to refer to such fields.

Note that in constructing the classes $\mathcal{F}^L$ and $\mathcal{F}^S$ the corresponding mathematical rigor is *not* pursued. Instead, in this work we focus on developing a generic *computational* framework which does not depend on filtering to describe the dynamics of the LS turbulent fields.

Decomposition similar to Eq. 4.3 can be also applied to a product fields obtained from u_i and p. For example, the nonlinear product of velocities $u_i u_j$ can be written as the sum of the LS and the SS components:

$$(u_i u_j)^L + (u_i u_j)^S = [(u_i^L + u_i^S)(u_j^L + u_j^S)]^L + [(u_i^L + u_i^S)(u_j^L + u_j^S)]^S \qquad (4.4)$$

To substitute the original problem given by Navier-Stokes equation the following

coupled system of the LS and the SS equations is proposed:

Proposition 1 *Let the LS and the SS velocity and pressure fields be such that* $u_i = u_i^L + u_i^S$, $p = p^L + p^S$, *and* u_i^L, $p^L \in \mathcal{F}^L$, u_i^S, $p^S \in \mathcal{F}^S$. *Then a coupled system of the LS and the SS equations:*

$$\frac{\partial u_i^L}{\partial t} + \frac{\partial}{\partial x_j}\Big[(u_i^L + u_i^S)(u_j^L + u_j^S)\Big]^L = -\frac{\partial p^L}{\partial x_i} + \nu\frac{\partial^2 u_i^L}{\partial x_j^2} \tag{4.5}$$

$$\frac{\partial u_i^S}{\partial t} + \frac{\partial}{\partial x_j}\Big[(u_i^L + u_i^S)(u_j^L + u_j^S)\Big]^S = -\frac{\partial p^S}{\partial x_i} + \nu\frac{\partial^2 u_i^S}{\partial x_j^2} \tag{4.6}$$

is equivalent to the original Navier-Stokes equation.

To show that Eqs. (4.5) and (4.6) can be obtained from the original Navier-Stokes equations one can substitute Eq. (4.3) into Eq. (4.1). Rearranging terms produces the coupled set of the LS and the SS equations:

$$\frac{\partial u_i^L}{\partial t} + \frac{\partial}{\partial x_j}(u_i^L + u_i^S)(u_j^L + u_j^S) = -\frac{\partial p^L}{\partial x_i} + \nu\frac{\partial^2 u_i^L}{\partial x_j^2} + F_i^S(u_i^S, p^S) \tag{4.7}$$

$$\frac{\partial u_i^S}{\partial t} + \frac{\partial}{\partial x_j}(u_i^L + u_i^S)(u_j^L + u_j^S) = -\frac{\partial p^S}{\partial x_i} + \nu\frac{\partial^2 u_i^S}{\partial x_j^2} + F_i^L(u_i^L, p^L) \tag{4.8}$$

where the forcing terms are given as:

$$F_i^L(u_i^L, p^L) = -\frac{\partial u_i^L}{\partial t} - \frac{\partial p^L}{\partial x_i} + \nu\frac{\partial^2 u_i^L}{\partial x_j^2} \tag{4.9}$$

$$F_i^S(u_i^S, p^S) = -\frac{\partial u_i^S}{\partial t} - \frac{\partial p^S}{\partial x_i} + \nu\frac{\partial^2 u_i^S}{\partial x_j^2} \tag{4.10}$$

The LS and the SS velocities affect each other through F_i^S, F_i^L, which both explicitly depend only on the corresponding LS or SS fields, and the nonlinear product term. It is seen that Eqs. (4.7), (4.8) represent the same Navier-Stokes equation, and only written for different velocities u_i^L or u_i^S. In spite of the similar functional form, Eqs. (4.7), (4.8) would describe different LS and SS evolution problems since they are subject to different boundary conditions and different forcing given by F_i^L and F_i^S respectively. Note that these intermediate LS and SS equations are dictated by decomposition $u_i = u_i^L + u_i^S$. This equation can be viewed as a redundant change of variables from u_i to twice bigger set of variables (u_i^L, u_i^S). As a result, one needs to specify six governing equations to describe the problem. However, introduction of twice bigger set of variables leads to increase of dimensionality of phase space. We make use of this redundancy by exploiting properties of the LS and the SS fields to simplify Eqs. (4.7), (4.8).

Explicitly expressing the LS and the SS parts of the nonlinear term in both equations according to Eq. (4.4) gives another set of the LS and the SS equations:

$$\frac{\partial u_i^L}{\partial t} + \frac{\partial}{\partial x_j}\Big[(u_i^L + u_i^S)(u_j^L + u_j^S)\Big]^L = -\frac{\partial p^L}{\partial x_i} + \nu\frac{\partial^2 u_i^L}{\partial x_j^2} + G_i^S(u_i^L, u_i^S, p^S) \tag{4.11}$$

$$\frac{\partial u_i^S}{\partial t} + \frac{\partial}{\partial x_j}\Big[(u_i^L + u_i^S)(u_j^L + u_j^S)\Big]^S = -\frac{\partial p^S}{\partial x_i} + \nu\frac{\partial^2 u_i^S}{\partial x_j^2} + G_i^L(u_i^L, u_i^S, p^L) \tag{4.12}$$

Here, the LS and the SS forcing terms G_i^L, G_i^S are given by:

$$G_i^L(u_i^L, u_i^S, p^L) = F_i^L(u_i^L, p^L) - \frac{\partial}{\partial x_j}\Big[(u_i^L + u_i^S)(u_j^L + u_j^S)\Big]^L \tag{4.13}$$

$$G_i^S(u_i^L, u_i^S, p^S) = F_i^S(u_i^S, p^S) - \frac{\partial}{\partial x_j}\Big[(u_i^L + u_i^S)(u_j^L + u_j^S)\Big]^S, \tag{4.14}$$

Both Eqs. (4.11) and (4.12) are still equivalent to the original Navier-Stokes Eq. (4.1) and can be re-written in a compact form:

$$G_i^L(u_i^L, u_i^S, p^L) + G_i^S(u_i^L, u_i^S, p^S) = 0 \tag{4.15}$$

It is seen that, under our assumption, G_i^L and G_i^S represent the LS and the SS fields, since all terms in their definitions belong to $\mathcal{F}^L$ and $\mathcal{F}^S$ class, respectively. In particularly, Eq. (4.15) holds if both the LS and the SS parts are equal to zero simultaneously:

$$G_i^L(u_i^L, u_i^S, p^L) = 0, \quad G_i^S(u_i^L, u_i^S, p^S) = 0 \tag{4.16}$$

To present some supportive arguments that solution given by Eq. (4.16) is a good candidate to be a unique solution of Eq. (4.15) we use a proof by contradiction. We assume that Eq. (4.16) is not true, i.e., $G_i^L \neq 0$. As a result, G_i^L, being the LS field, has substantial non-zero energy in LS modes. Without loss of generality one can assume that most energy is concentrated at some wavenumber $k_L < k_\Delta$ which is well into the LS spectral content, as shown schematically in Fig. 4.2(a). From Eq. (4.12) it is seen that G_i^L is the forcing term for the SS velocity field u_i^S. Therefore, the solution of the SS equation subject to the LS forcing would cause the SS energy e^S not to be small in comparison with the LS energy e^L for the LS mode spectral content ($k<k_\Delta$), which contradicts to the definition of the SS velocity field since $u_i^S \notin \mathcal{F}^S$.

Thus the LS spectral content of G_i^L should be negligible or zero in the neighborhood of k_L. If one moves k_L towards the cut-off wave number k_Δ, then it is clear that the same reasoning can be applied up to the δ-neighborhood of k_Δ. As a result, G_i^L should be zero function, or a function which is negligible everywhere, except the δ-neighborhood of k_Δ, as shown in Fig. 4.2(b). From Eq. (4.15), it is seen that G_i^S should be also zero function, or the same function as G_i^L (with an opposite sign) and with the same spectral content negligible everywhere and peaking at k_Δ. This can be written schematically as:

$$\begin{cases} e^L(k) \approx & e^S(k) \approx \varepsilon, \quad k < k_\Delta - \delta/2, \\ e^L(k) \approx & e^S(k) \approx e^\Delta, \quad k_\Delta - \delta/2 < k < k_\Delta + \delta/2, \\ e^L(k) \approx & e^S(k) \approx \varepsilon, \quad k > k_\Delta + \delta/2 \end{cases}$$

with $\varepsilon \ll e^\Delta$.

It is now seen that being this non-zero function, G_i^L and G_i^S lose their LS and SS properties, and do not belong to $\mathcal{F}^L$ and $\mathcal{F}^S$ classes anymore. Clearly, G_i^L and

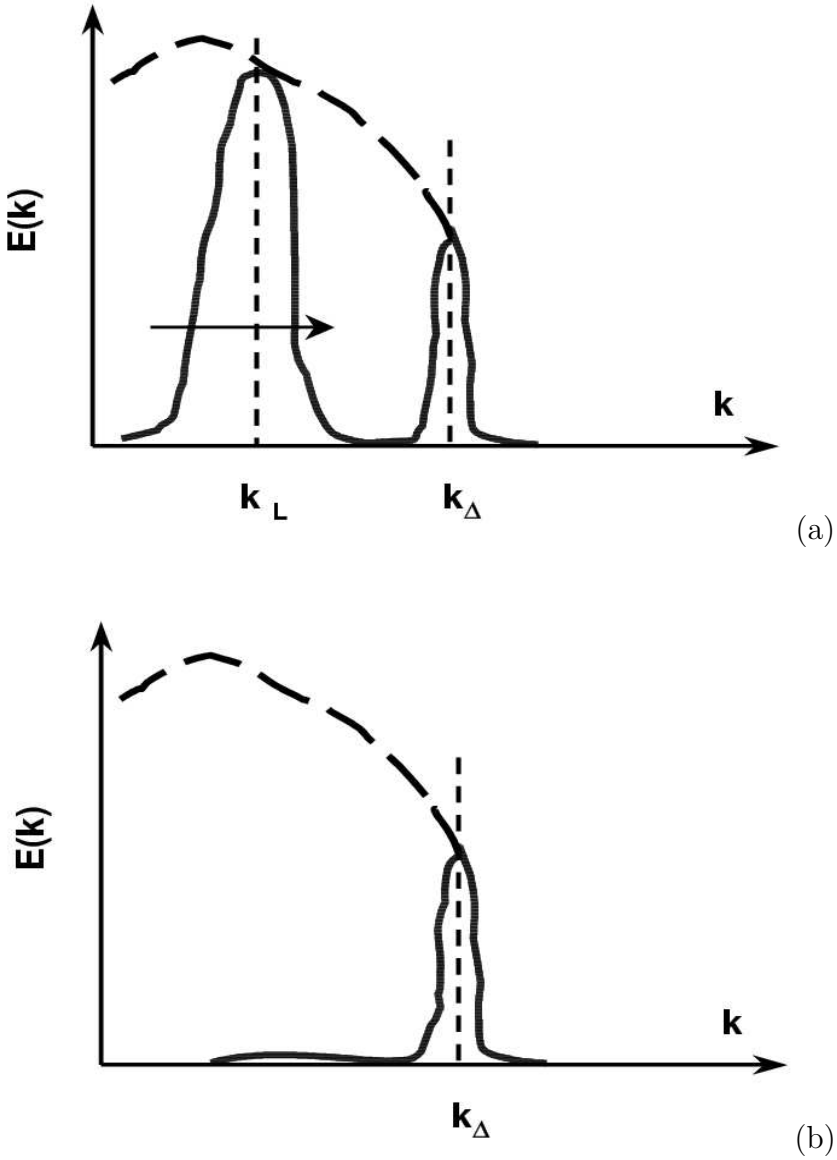

Figure 4.2: (a) Sketch of the assumed spectral energy of G_i^L forcing term; (b) sketch of a possible spectral energy of G_i^L which would satisfy $G_i^L + G_i^S = 0$. Note that G_i^L does not represent neither the LS field nor the SS field. Typical spectral energy of the LS field is shown by dashed line. Maximal grid resolvable mode k_Δ and LS mode k_L are shown by dashed vertical lines.

G_i^S do not have substantial LS or SS energy contents over the corresponding range of scales, thus $G_i^L \notin \mathcal{F}^L$ and $G_i^S \notin \mathcal{F}^S$. In fact, they become indistinguishable, and the decomposition loses its meaning. Therefore, Eq. (4.16) must be hold, since zero function is the only element which belongs to both $\mathcal{F}^L$ and $\mathcal{F}^S$ classes simultaneously. Substituting Eq. (4.16) into Eqs. (4.11, 4.12) gives the LS equation (4.5) and the SS equation (4.6). Note that the spectral overlap between u_i^L and u_i^S does not affect these arguments since they are applied to the forcing terms G_i^L and G_i^S only.

A proof in the opposite direction follows immediately if one adds Eqs. (4.5) and (4.6). Then, it is seen that the sum of the LS and the SS solutions $u_i^L + u_i^S$, $p^S + p^L$ satisfies the original Navier-Stokes equation.

Note, that the forcing terms F_i^S, F_i^L can also be written in alternative form. Equations (4.13, 4.14) give:

$$F_i^L = \frac{\partial}{\partial x_j}\Big[(u_i^L + u_i^S)(u_j^L + u_j^S)\Big]^L, \quad F_i^S = \frac{\partial}{\partial x_j}\Big[(u_i^L + u_i^S)(u_j^L + u_j^S)\Big]^S \tag{4.17}$$

As a result, the nonlinear convective term in the SS equation represents the SS part of the total convective term and can be further rewritten in a more convenient form. Substituting Eq. (4.17) into Eq. (4.6) gives the equivalent form of the SS equation:

$$\frac{\partial u_i^S}{\partial t} + \frac{\partial}{\partial x_j}(u_i^L + u_i^S)(u_j^L + u_j^S) = -\frac{\partial p^S}{\partial x_i} + \nu\frac{\partial^2 u_i^S}{\partial x_j^2} + F_i^L \tag{4.18}$$

The LS Eq. (4.5) is, in fact, the standard LES equation. Rewriting the LS equation using LES notation, i.e., $u_i^L \to \bar{u}_i$, $u_i^S \to u_i'$, $p^L \to \bar{p}$ gives:

$$\frac{\partial \bar{u}_i}{\partial t} + \frac{\partial}{\partial x_j}\overline{\bar{u}_i\bar{u}_j} = -\frac{\partial \bar{p}}{\partial x_i} + \nu\frac{\partial^2 \bar{u}_i}{\partial x_j^2} - \frac{\partial}{\partial x_j}(\overline{u_i u_j} - \overline{\bar{u}_i\bar{u}_j}), \tag{4.19}$$

where the last term represents the derivative of the residual stress $\tau_{ij} = \overline{u_i u_j} - \overline{\bar{u}_i\bar{u}_j} = \overline{u_i' u_j'} + \overline{\bar{u}_i u_j'} + \overline{u_i'\bar{u}_j}$ In LES, Eq. (4.19) is usually derived by filtering of the original Navier-Stokes equations and assuming commutativity between filtering and differentiation. Similarly Eq. (4.5) can be formally obtained by applying $\mathcal{L}^\Delta$ to the original Navier-Stokes equation, and further assuming its commutativity with differentiation. However, the formal application of $\mathcal{L}^\Delta$ to derive the LS equation is questionable on at least two accounts. First, it implicitly assumes that the LS solution should be sought only in particular form, as defined by specific structure of $\mathcal{L}^\Delta$. This might effectively narrow the LS class $\mathcal{F}^L$. In addition, in general case the structure of $\mathcal{L}^\Delta$ is not known. Second, the intermediate presence of the discrete averaging operator $\mathcal{S}^\Delta$ might potentially destroy the well-posedness of the LS problem (which should be desired criterion for mathematically consistent LS models ([53]). For these reasons, in the present formulation the LS equations are not derived based on formal application of $\mathcal{L}^\Delta$, or filtering.

This can be further illustrated by considering a simple 1D diffusion equation $\partial_t u = \nu\partial_{xx}^2 u$ on an infinite domain. Let us further assume that $\mathcal{L}^\Delta$ is a composition of the interpolation cubic spline operator $\mathcal{I}^\Delta$ and the grid sampling operator $\mathcal{S}^\Delta$. If

one applies $\mathcal{L}^{\Delta}$ to derive the LS equation analogous to Eq. 4.5, the following formal LS equation is produced:

$$\partial_t u^L = \nu \partial^2_{xx} u^L - \Big(\mathcal{L}^{\Delta}[\partial_t u] - \partial_t u^L - \nu \mathcal{L}^{\Delta}[\partial^2_{xx} u] + \nu \partial^2_{xx} u^L \Big) \tag{4.20}$$

On the other hand, the LS diffusion equation $\partial_t u^L = \nu \partial^2_{xx} u^L$ has a solution given by the Poisson formula:

$$u^L(x,t) = \frac{1}{2\sqrt{\pi \nu t}} \int_{-\infty}^{+\infty} exp\Big[- \frac{(x-y)^2}{4\nu t} \Big] u_0^L(y) \mathrm{d}y.$$

It is seen that even if the LS initial condition is $u_0^L = \mathcal{L}^{\Delta}[u_0]$, the LS solution itself can not be exactly represented in the form $u^L(x,t) = \mathcal{L}^{\Delta}[u(x,t)]$, since it is a convolution integral of the fundamental solution with a cubic spline function u_0^L. It means that a class of functions u^L which is defined by $\mathcal{L}^{\Delta}$ (i.e., cubic-spline polynomials) where we look for solution of the LS equation, is too "narrow" and can not accommodate the actual solution u^L. This results in appearance of extra non-commutative terms in Eq. (4.20).

Similar qualitative reasoning which was used to justify Eq. 4.16 can be also applied to the continuity constraint, which leads to the LS and SS equations, $\nabla_i u_i^L = r$ and $\nabla_i u_i^S = -r$. Here, a function $r(\mathbf{x})$ is zero, or has a negligible energy content everywhere, except a neighborhood of k_{Δ}. To satisfy a requirement of being the LS and SS field simultaneously, one has to choose $r(\mathbf{x}) = 0$ which results in the LS and the SS continuity equations:

$$\frac{\partial u_i^L}{\partial x_i} = 0, \quad \frac{\partial u_i^S}{\partial x_i} = 0 \tag{4.21}$$

Physically, such an interpretation of $r(\mathbf{x})$ has also clear meaning by specifying incompressible the LS and the SS velocity fields, as opposed to a case where $r(\mathbf{x}) \neq 0$. By considering different k_{Δ}, it is seen that in latter case $r(\mathbf{x})$ should depend on k_{Δ} which leads to unclear physical constraints for the LS and the SS velocities.

In summary, the coupled system of Eqs. (4.5) and (4.18) along with the constraint (4.21) supplied by appropriate initial and boundary conditions completely defines evolution of the LS and the SS fields in TLS approach.

4.2 Treatment of Small-Scale Equation

Numerical simulation of the 3D SS equation is computationally challenging since it would require the resolution of the whole range of small scales. On the other hand, the LS equation is solved on a coarse LS grid with a time step comparable to the characteristic turnover time of the smallest resolvable LS eddy. As a result, the complete knowledge of the SS field in space and time is not necessary since one only needs to know the SS fields on the LS grid at the LS time scale in order to close the LS equation. Based on the premise that all SS nonlinear terms are important we propose to treat the SS equation on a "lower-dimensional" domain.

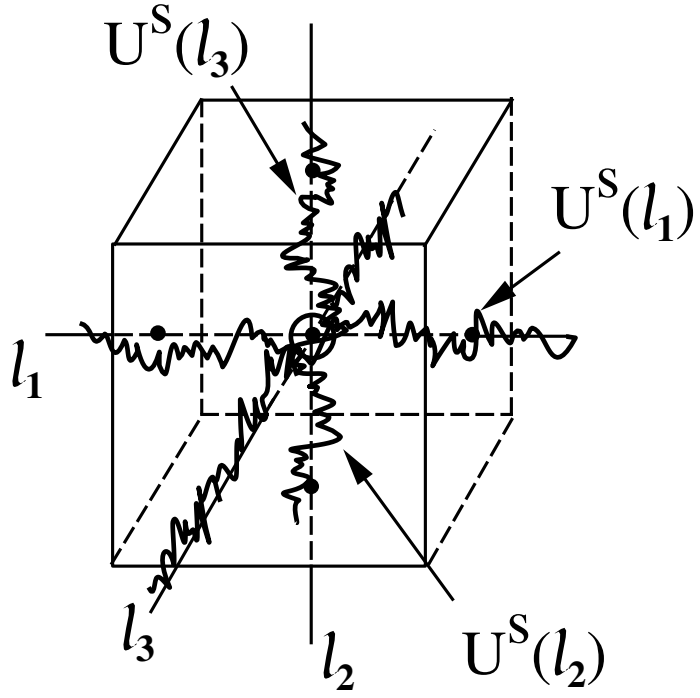

Figure 4.3: The SS line arrangement within a 3D LS cell. One component of the SS velocity is shown on each line schematically.

To reduce computational expenses, while retaining two-way coupling between the LS and the SS fields, the SS equation (Eq. (4.18)) is solved on a collection of 1D lines embedded in domain Ω, rather than in the whole domain Ω. In general, there are no any restrictions on the position of lines in Ω and their curvature. Here, for simplicity, we consider a family of lines $\Omega_l = \{l_k^j\}$, $k = 1, 2, 3$, $j = 1 \dots N_k$, where N_k denotes a number of lines parallel to the corresponding LS coordinates $\{x_k\}$. This family consists of $\sum_k N_k$ lines which intersect each other at the LS grid nodes, as shown in Fig. 4.3. The SS velocity fields defined on these lines as:

$$u_i^S(\mathbf{x}, t) \longrightarrow u_{i,l_k}^S(l_k, t), \qquad \mathbf{x} \in l_k \subset \Omega \tag{4.22}$$

The SS field u_{i,l_k}^S is viewed as a snapshot of the SS turbulent velocity along the line l_k.

In TLS, the SS field is computed in the domain Ω_l only, while the LS field is simulated in the whole 3D domain Ω. Assuming that one needs N_S^3 points to resolve the smallest dynamically important scales for DNS, and N_L^3 points to resolve the large scale dynamics, as in LES, results in the TLS resolution requirement of $N_L^3 + 3N_L^2 N_S$ points to represent both the LS and the SS fields. Thus, the TLS approach would fall in a category between DNS and LES. However, it is often the case for LES that N_L^3 has to be quite high ($N_L \to N_S$) in highly turbulent regions, for example near walls, to accurately predict the LS dynamics because of the inherent limitations of the SGS models ([54]). In TLS, since the LS and SS are explicitly coupled, the less

severe resolution requirements might be expected. In addition, simulation of the SS fields on the 1D lines, which requires $3N_L^2 N_S$ point resolution, can be done in parallel, thereby, reducing computational cost substantially.

Treating the SS fields on the reduced domain Ω_l is computationally more efficient, but there is a price to pay. When written on a line, say $l_1 = \{x_1, x_2 = C_2, x_3 = C_3\}$, where C_2, C_3 are constants, the SS Eq. (4.18) is not closed and requires knowledge of the first derivatives of the SS velocity and pressure, and the second derivatives of SS velocity in the directions l_2, l_3 (which are orthogonal to the line l_1). Thus, all derivatives of the SS fields in transversal directions to a given line have to be modeled, although, all derivatives along the line can be computed as a part of solution. The second difficulty arise from the fact that at the LS grid nodes, where the lines l_k intersect, the SS field becomes overdetermined since its values can be found from all three intersecting lines, and these values are not necessarily the same. Explicit requirement to have unique values of the SS fields at the LS grid points would lead to coupling of SS fields on different lines at those points, and therefore, is not viable computationally. Instead, we decouple the SS field computations on lines, which means that the SS fields do not interact each other if they belong to different lines. At the same time, all realizations (along all three lines) are still used to obtain the representation of the SS field on the LS grid. Thus, the value of the SS field at the node $\{\mathbf{x}_\mathrm{n}\}$ of the LS grid cell ΔV_n is defined as an average over all three lines belonging to ΔV_n and intersecting at $\{\mathbf{x}_\mathrm{n}\}$. For example,

$$[u_i^S]^L(\mathbf{x}_\mathrm{n}, t) \longleftarrow \Big[u_{i,l_k}^S(l_k, t)\Big]_{l_k}, \quad [u_i^S u_j^L]^L(\mathbf{x}_\mathrm{n}, t) \longleftarrow \Big[u_{i,l_k}^S u_{j,l_k}^L(l_k, t)\Big]_{l_k} \tag{4.23}$$

$$[u_i^S u_j^S]^L(\mathbf{x}_\mathrm{n}, t) \longleftarrow \Big[u_{i,l_k}^S u_{j,l_k}^S(l_k, t)\Big]_{l_k}, \quad \{\mathbf{x}_\mathrm{n}\} = \bigcap_{k=1}^{3} l_k, \quad l_k \cap \Delta V_\mathrm{n} \neq \emptyset$$

where the local average over intersecting orthogonal lines l_k in the cell ΔV_n is denoted as $[\quad]_{l_k}$. Note that in order to close the LS equations we need know the LS values of the mutual product of the SS velocities $u_i^S u_j^S$ and the mixed products $u_i^S u_j^L$, $u_i^L u_j^S$ rather than the SS velocity itself. Explicit computation of these SGS terms requires knowledge of the SS velocity on each line.

The following model assumptions provide necessary simplification for the SS equation (Eq. (4.18)) and allow to express the unknown (transverse) SS derivatives in terms of the known (longitudinal) SS derivatives. The model assumptions are justified, in part, by *a priori* analysis of DNS data and by *a posteriori* study of high-Re turbulent flows, and are following:

(i) For each SS velocity component u_i^S, the SS second derivative along the line l_k is equal to the averaged sum of the SS second derivatives along all three orthogonal directions:

$$\frac{\partial^2 u_i^S}{\partial x_k^2} = \frac{1}{3}\sum_{j=1}^{3} \frac{\partial^2 u_i^S}{\partial x_j^2}, \quad i, k = 1, 2, 3 \tag{4.24}$$

(ii) Changes of the SS part of the convective derivatives of the SS velocity components are neglected in directions transverse ($j \neq k$) to the line l_k:

$$\frac{\partial}{\partial x_j}\Big[(u_j^S + u_j^L)(u_i^S + u_i^L)\Big]^S = \frac{\partial}{\partial x_j}\Big[(u_j^S(l_k) + u_j^L)(u_i^S(l_k) + u_i^L)\Big]^S, \tag{4.25}$$

These assumptions lead to the following simplified SS governing equations on each line l_k:

$$\frac{\partial u_i^S}{\partial t} + \frac{\partial}{\partial x_j}\big(u_j^L + u_j^S(l_k)\big)\big(u_i^L + u_i^S(l_k)\big) = 3\nu\frac{\partial^2 u_i^S}{\partial x_k^2} + F_i^L(u_j^S(l_k), u_j^L), \tag{4.26}$$

where

$$F_i^L(u_j^S(l_k), u_j^L) = \frac{\partial}{\partial x_j}\Big[\big(u_j^L + u_j^S(l_k)\big)\big(u_i^L + u_i^S(l_k)\big)\Big]^L \tag{4.27}$$

Note, here k is a free index and refers to a line l_k which is parallel to the corresponding coordinate x_k. Thus, for different lines Eq. (4.26) produces different equations for the same SS velocity component. For example, for lines l_1, l_2 and u_1^S we have:

$$\frac{\partial u_1^S}{\partial t} + \frac{\partial}{\partial x_j}\big(u_j^L + u_j^S(l_1)\big)\big(u_1^L + u_1^S(l_1)\big) = 3\nu\frac{\partial^2 u_1^S}{\partial x_1^2} + F_1^L(u_j^S(l_1), u_j^L) \tag{4.28}$$

$$\frac{\partial u_1^S}{\partial t} + \frac{\partial}{\partial x_j}\big(u_j^L + u_j^S(l_2)\big)\big(u_1^L + u_1^S(l_2)\big) = 3\nu\frac{\partial^2 u_1^S}{\partial x_2^2} + F_1^L(u_j^S(l_2), u_j^L) \tag{4.29}$$

To solve Eq. (4.26), boundary conditions for the SS velocity field have to be specified. The SS boundary conditions are prescribed based on the line position and have to be consistent with the decomposition definition of the SS field according to Eq. (4.3).

In Eq. (4.26) the SS pressure gradient $\partial p^S/\partial x_i$ is explicitly excluded. In other words, we relax the divergence-free requirement for the SS velocity along the line l_k, i.e., $\partial u_j^S/\partial x_j \neq 0$. In principle, the SS pressure can be included in Eq. (4.26) by specifying the LS pressure, and an additional equation for the SS pressure. For example, taking the divergence of Eq. (4.7) and using Eq. (4.21) we have:

$$\frac{\partial^2 p^S}{\partial x_i^2} = -\frac{\partial^2 p^L}{\partial x_i^2} - \frac{\partial(u_i^L + u_i^S)}{\partial x_j}\frac{\partial(u_j^L + u_j^S)}{\partial x_i} \tag{4.30}$$

In our case, the non-enforcement of the SS continuity is an artifact of the incompressible fluid model and the adopted numerical approach. The continuity equation is used for the LS velocity only, and implemented according to the standard fractional step (projection) method by computing intermediate non-divergent LS velocity field. If the current approach is adopted for a compressible flow then the continuity requirement will appear naturally as a separate governing equation for the SS density.

There is a noticeable lack of comprehensive analysis of the SS velocity derivatives in LES literature. Most studies are concerned with modeling of the SGS stress which

represents the LS quantity and do not require explicit knowledge of the SS fields or their derivatives. Here, to justify the simplifying model assumptions from the physical point of view, *a priori* statistical analysis of high-Re turbulence data sets is conducted first. The first data set is obtained from the forced isotropic turbulence simulation of [52]. Turbulent velocity field corresponds to the Taylor scale Reynolds number $Re_\lambda \approx 140$ and is given on a box of 256^3 grid points. The LS field is computed based on the uniform 32^3 LS grid using cubic spline interpolation, and then subtracted from the total velocity to obtain the SS velocity. The second DNS data set corresponds to the non-homogeneous turbulent case of fully developed channel flow simulation of [55]. This DNS study was conducted at $Re_\tau = 640$ ($Re \approx 24300$) on the $512 \times 256 \times 256$ orthogonal grid stretched in wall-normal direction. The LS field is computed based on the $32 \times 40 \times 32$ LS grid, similar to the isotropic turbulence case.

4.2.1 Assumption (i)

The assumption (i), given by Eq. (4.24), corresponds to the case when the difference between the SS second derivative in particular direction l_k and the averaged sum of the SS second derivatives in all three directions is equal to zero, i.e., $S_{ik} = 0$ where $S_{ik} = \sum_{j=1}^{3} \partial^2 u_i^S/\partial x_j^2/3 - \partial^2 u_i^S/\partial x_k^2$. This is supported by Figures 4.4(a-c) where all nine $(i,k = 1,2,3)$ normalized probability density functions (PDF) $f(S_{ik})$ are shown for both isotropic and non-homogeneous cases, respectively. It is interesting to note they fit the Tsallis distribution quite well for wide range of probabilities. The Tsallis distribution was used in the context of turbulence by [56]. It has a form $P_T(\xi) = 1/(Z_q[1 + (1/2)\beta(q-1)\xi^2]^{1/(q-1)})$ with parameters q, β. Here, Z_q is a normalization constant and $\beta = 2/(5-3q)$ is chosen to give a unit variance. The Tsallis distribution reduces to a Gaussian distribution as $q \to 1$. It is also seen that the higher Re number case of the non-homogeneous turbulence is characterized by wider PDF tails emphasizing strong near-wall bursting events.

These figures show that the most probable state for the derivative differences S_{ik} is zero, or in other words, the second derivatives in orthogonal direction are equal each other with the highest probability. Therefore, the dissipative influence of low probable and rare events characterized by $S_{ik} \neq 0$ is excluded from consideration by adoption of Eq. 4.24. However, this approximation can still adequately account for the dissipative influence of high gradient events which dominate turbulent flow regions. Conceptually, one can divide events where $S_{ik} = 0$ in two qualitatively different groups. The first group represents a case when the SS second derivatives are small, so the difference S_{ik} is small too. Physically, points with this property would correspond to weakly turbulent flow regions which are already adequately represented by the resolved LS motion. The second group corresponds to a case when the SS second derivatives are not small and approximately equal each other. These flow regions are characterized by intense turbulence, high dissipation and the strong effect of the SS on the LS dynamics.

This can be clarified further by considering the joint PDFs of $\sum_{j=1}^{3} \partial^2 u_i^S/\partial x_j^2/3$ and $\partial^2 u_i^S/\partial x_k^2$ which are shown in Figs. 4.5-4.7.

It is seen that at the origin all PDF exhibits a characteristic spike. Contour lines

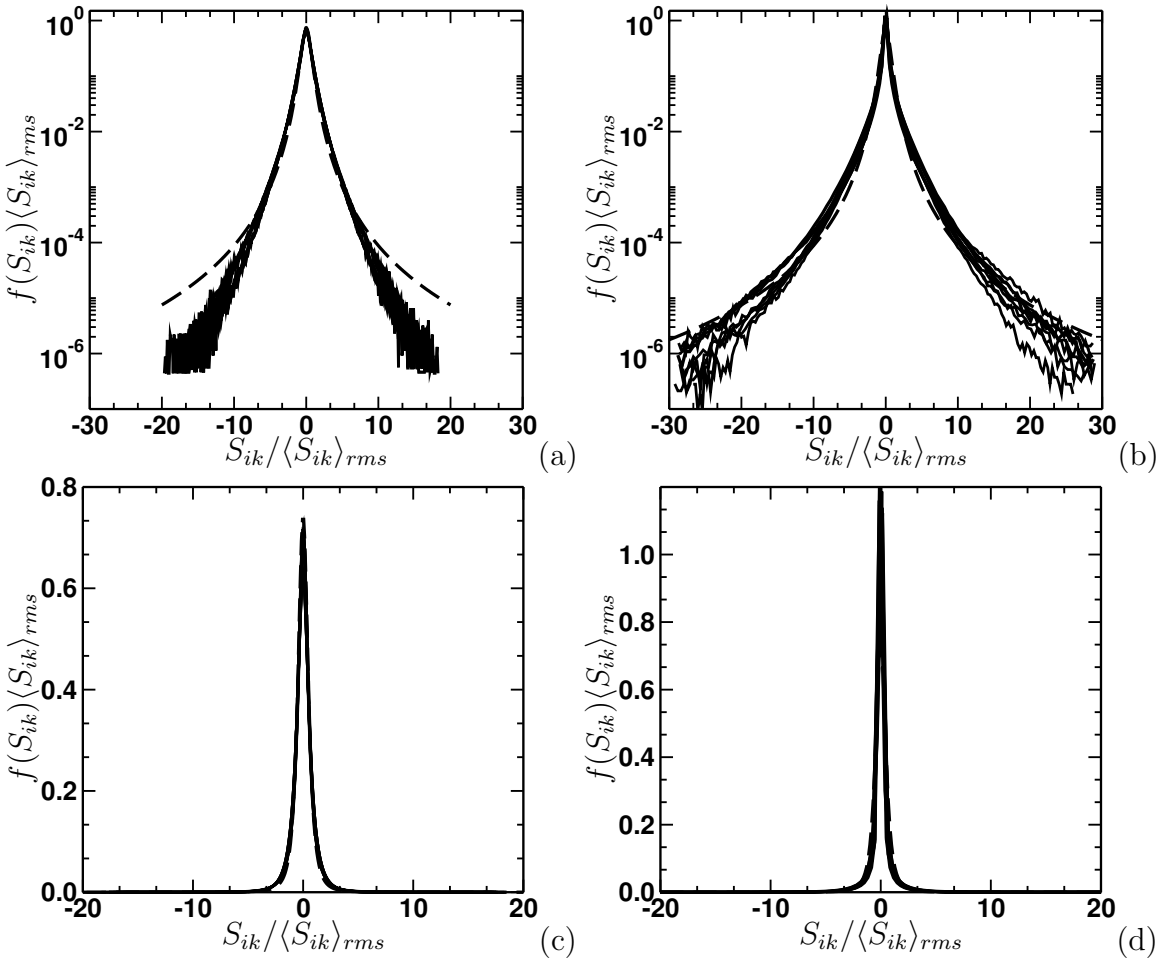

Figure 4.4: PDFs of the normalized differences of the second SS derivatives, $S_{ik} = \sum_{j=1}^{3} \partial^2 u_i^S/\partial x_j^2/3 - \partial^2 u_i^S/\partial x_k^2,\ i,k = 1,2,3$ compared with the Tsallis distribution (dashed line): forced isotropic turbulence (a), (c) and (b), (d) turbulent channel flow, in logarithmic and linear scales, respectively.

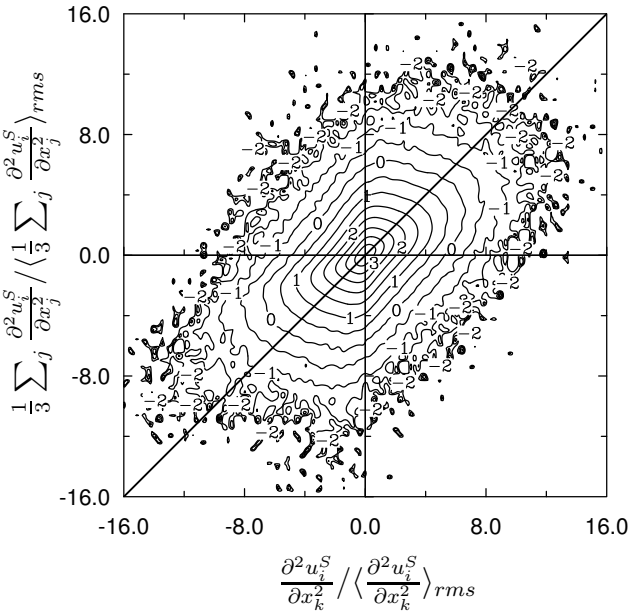

(a)

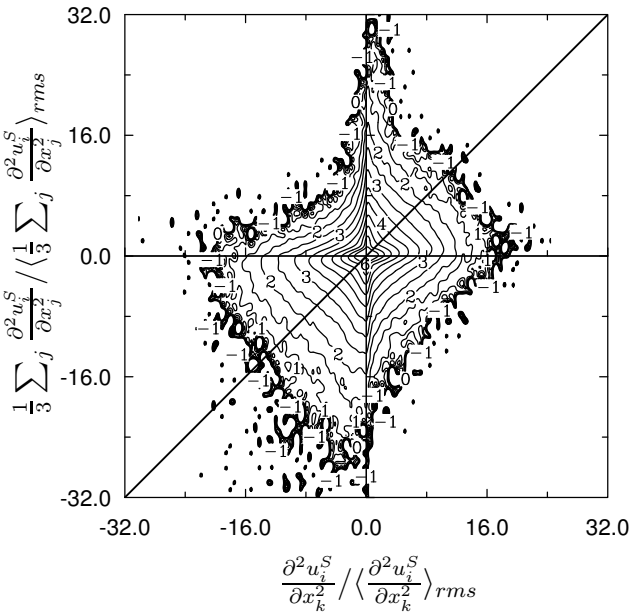

(b)

Figure 4.5: Contour plots of the logarithm of the joint PDF of the SS second derivative of the longitudinal velocity component ($i = k$, $i = 1$, $k = 1$) and the averaged sum of all SS second derivatives: (a) isotropic turbulence; (b) turbulent channel flow.

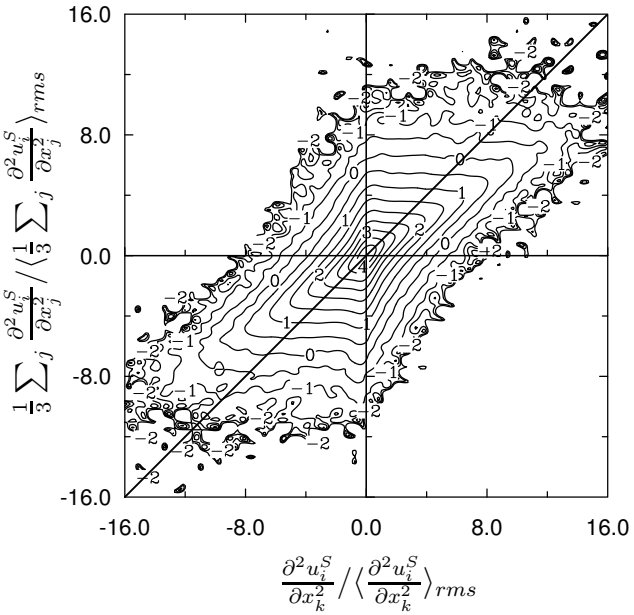

(a)

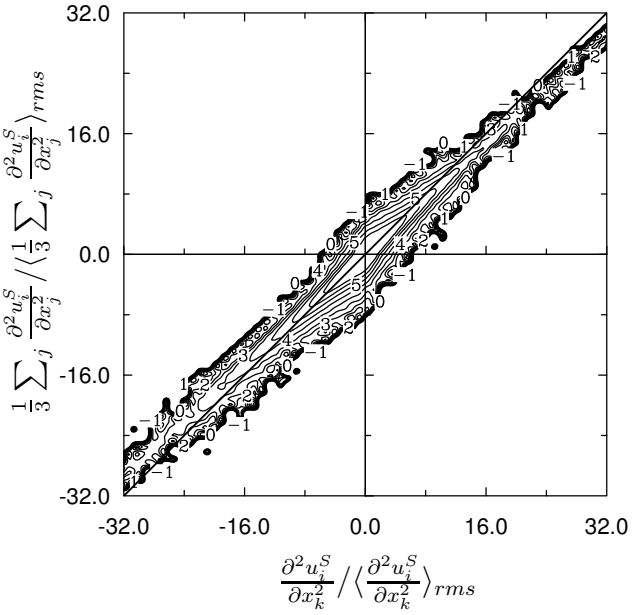

(b)

Figure 4.6: Contour plots of the logarithm of the joint PDF of the SS second derivative of the transverse velocity component ($i \neq k$, $i = 1$, $k = 2$) and the averaged sum of all SS second derivatives: (a) isotropic turbulence; (b) turbulent channel flow.

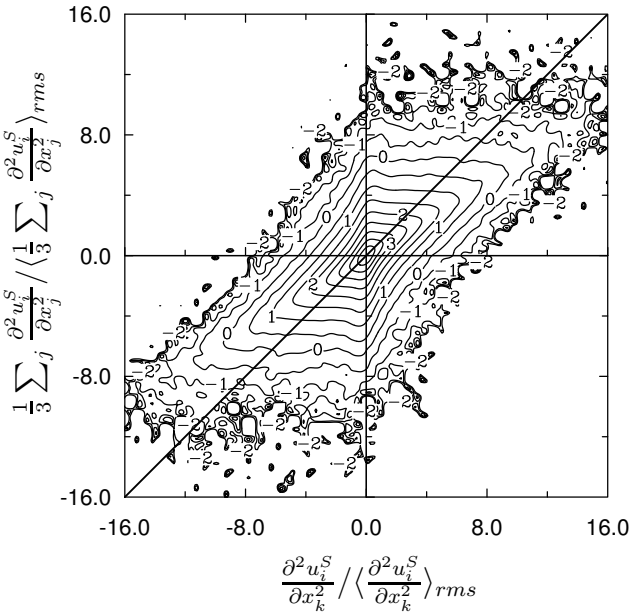

(a)

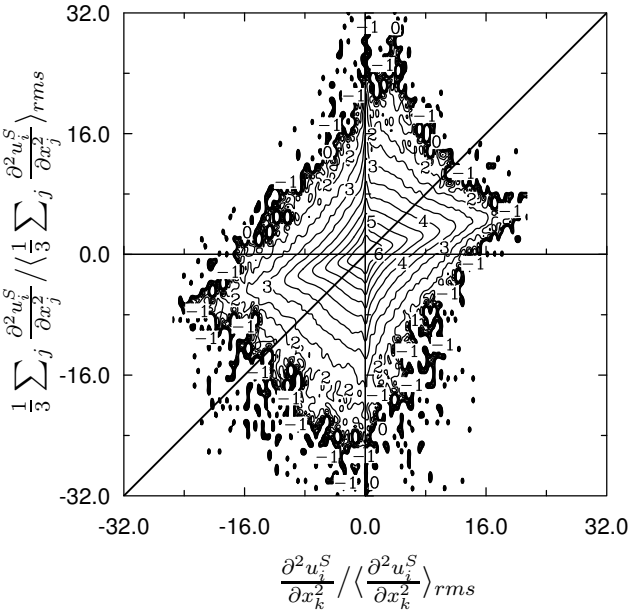

(b)

Figure 4.7: Contour plots of the logarithm of the joint PDF of the SS second derivative of the transverse velocity component ($i \neq k$, $i = 1$, $k = 3$) and the averaged sum of all SS second derivatives: (a) isotropic turbulence; (b) turbulent channel flow.

for high probabilities are approximately oval in shape and elongated along a diagonal of I and III quadrants. For lower values of probability the contour lines resemble parallelograms with smoothed corners. It is also seen that events where the second derivative $\partial^2 u_i^S/\partial x_k^2$ is large in magnitude and has the same sign as the averaged sum $\sum_{j=1}^{3} \partial^2 u_i^S/\partial x_j^2/3$ are more probable and provide major contribution to the tail of the joint PDF. From Fig. 4.6(b), the most prominent elongation of the PDF shape exhibits the SS second derivative of streamwise velocity in the wall-normal direction for a case of turbulent channel flow. This is consistent with the qualitative self-sustaining mechanism of the near-wall turbulence which is characterized by the bursting process in the wall-normal direction where up to 80% of the Reynolds stress is generated (see, for example [57], [58]). For the forced isotropic turbulence, Figs. 4.6(a) and 4.7(a) show that PDF's of the SS second derivatives in different transverse directions are the same which is consistent with isotropy.

Therefore, with high probability, one may expect that in intense turbulent regions if the second derivative of the SS velocity component is large in magnitude in one particular direction it should be large and has the same sign in other two orthogonal directions. This can be somewhat related to a qualitative geometrical picture of the small-scale turbulence which has been the subject of much numerical and experimental efforts. It is known that regions of high level vorticity form non-trivial geometrical pattern which is characterized by elongated vorticity tubes and ribbons called "worms" ([59], [60]), where high level of energy dissipation is concentrated. A line l_k arbitrarily placed in flow field would intersect low dissipation regions, where all SS second derivatives are small and also the intense small-scale structures - worms, where the SS dissipation is high, and therefore, the SS second derivatives are expected to be quite large. Note that the intense enstrophy regions (worms) do not necessarily coincide with the high dissipation regions since the high values of the SS derivatives do not always result in the high values of the SS vorticity. However, one can assume that much dissipation is located in the neighborhood of the SS vortex tubes, at the distance not exceeding the order of magnitude of the Kolmogorov scale. This is consistent with the DNS results of [61] as well as with the results based on the simple Burgers vortex model ([1]).

The bisector of I and III quadrants corresponds to the model assumption (i). It is seen that events from the first group occur in the neighborhood of the origin and happen with the highest probability. As one moves along the diagonal from the origin the magnitude of the SS second derivative increases, probability decreases, suggesting the presence of highly turbulent regions where the LS resolution becomes inadequate. Note that model assumption $S_{ik} = 0$ corresponds to the delta function PDF at the origin, see Figs. 4.4(a-d). As a result, all events which correspond to $S_{ik} \neq 0$ are formally excluded from the consideration. However, as suggested by Figs. 4.5-4.7 the model assumption is not "blind" to the presence of intense SS turbulent structures. Large values of the SS second derivatives are still allowed on the diagonal $S_{ik} = 0$. Figure 4.6(b) also suggests that the assumption (i) is more justified for the turbulent regions of the higher intensity.

For the further qualitative interpretation of the model assumption $S_{ik} = 0$ we

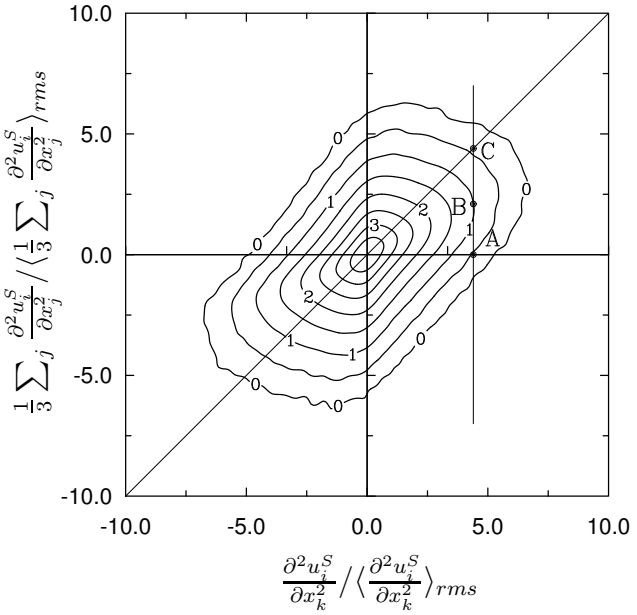

Figure 4.8: Point (B) - the most probable value of the averaged sum of the SS second derivatives given the value of the SS second derivative along the line l_k at point (A), point (C) corresponds to the model assumption.

consider the joint PDF as shown in Figure 4.8 for the case of the SS longitudinal derivative ($i = k$). Assume that the SS second derivative is sufficiently large and correspond to the point A suggesting the presence of the highly turbulent region. A vertical plane through A and orthogonal to the x-axis defines a conditional PDF $f((\sum_{j=1}^{3} \partial^2 u_i^S/\partial x_j^2)/3 | \partial^2 u_i^S/\partial x_k^2 = a)$. It is seen that this conditional PDF is positively skewed giving the the most probable value of the averaged sum $(\sum_{j=1}^{3} \partial^2 u_i^S/\partial x_j^2)/3$ around point B. On the other hand, the line defined by the model assumption $S_{ik} = 0$ intersects with the conditional plane at point C. Due to the shape of the joint PDF, point C will always stays higher (or lower) than the maximum point B if $\partial^2 u_i^S/\partial x_k^2$ is positive (or negative) and sufficiently large in magnitude. Thus, the model assumption $S_{ik} = 0$ makes the larger value of the sum of the SS second derivative more probable. This can be viewed as if the value of local viscosity is higher, which means that the SS vortical structures are more dissipative.

4.2.2 Assumption (ii)

The model assumption (ii) (Eq. 4.25) allows to represent the SS line equations in the closed form. Physically it means that the SS effects that are caused by advection of the SS velocity, in the line orthogonal directions, are small in comparison the SS effects due to advection of the LS field. To show this it is convenient to rewrite the assumption (ii) in non-conservative form with a help of the continuity equation:

$$\frac{\partial}{\partial x_j}\Big[(u_j^S + u_j^L)(u_i^S + u_i^L)\Big]^S = \frac{\partial}{\partial x_j}(u_j^S + u_j^L)(u_i^S + u_i^L) - F_i^L(u_i^L, u_i^S)$$
$$= (u_j^S + u_j^L)\frac{\partial}{\partial x_j}(u_i^S + u_i^L) - F_i^L = (u_j^S(l_k) + u_j^L)\frac{\partial}{\partial x_j}(u_i^S(l_k) + u_i^L) - F_i^L \quad (4.31)$$
$$= (u_k^S(l_k) + u_k^L)\frac{\partial}{\partial x_k}(u_i^S(l_k) + u_i^L) + \underbrace{(u_j^S(l_k) + u_j^L)\frac{\partial u_i^L}{\partial x_j}}_{j \neq k} - F_i^L$$

Note that the SS advection term is fully accounted along line l_k since derivatives of the SS velocity are always available.

Contours plots of the joint PDFs of the total SS convective terms and the modeled SS convective terms are exhibited in Figs. 4.9(a)-4.11(a) and Figs. 4.9(b)-4.11(b) for the forced isotropic turbulence and the turbulent channel, respectively. Since the wall-normal direction plays a special role for the turbulent channel the SS convective derivatives in non-homogeneous direction ($j = 2$) are considered. Three cases are shown which correspond to different orientation of velocity components and the streamwise line l_1. It is seen that contour lines have similar oval shapes for high probabilities corresponding to small values of the SS convective terms. As the magnitude of the SS convective terms grow and probability sharply decreases, the contour plots start resembling a parallelogram shape which is stretched along the diagonal of the I and III quadrants. The shape of PDFs is also almost independent on the direction of the SS convective derivatives, especially for the forced isotropic turbulence. SS events when both the total and the modeled SS convective terms have the same sign

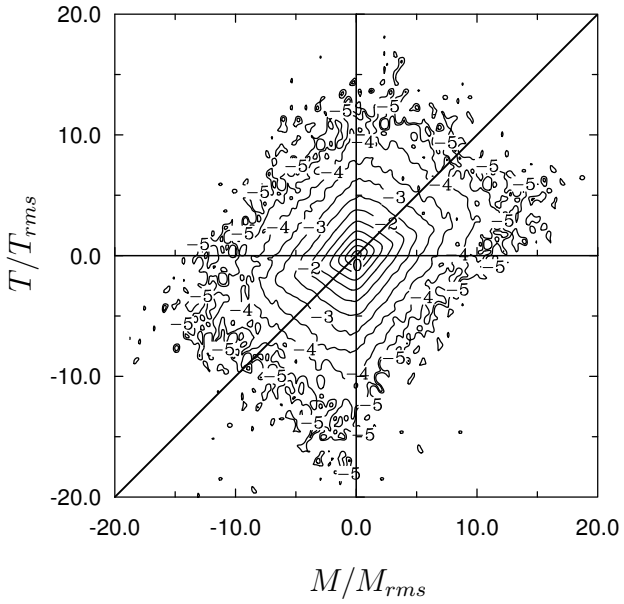

(a)

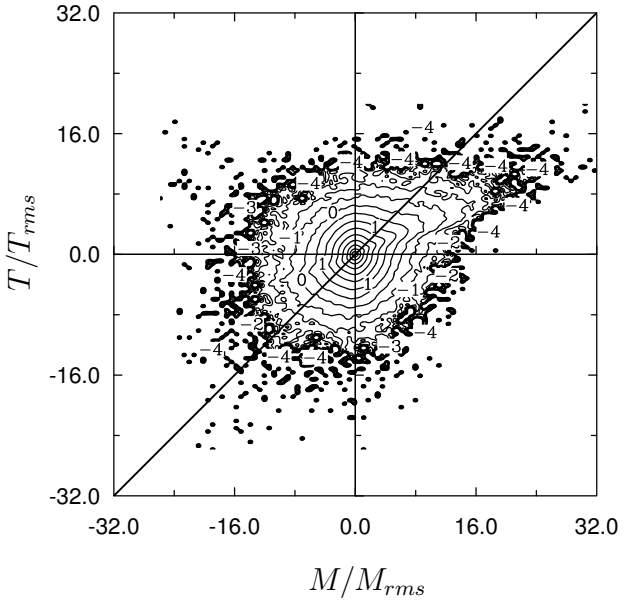

(b)

Figure 4.9: Contour plots of logarithm of the joint PDF of the total SS advection term T and the modeled SS advection term M for $i = k$, $j \neq k$ ($i = 1$, $k = 1$, $j = 2$): (a) forced isotropic turbulence; (b) turbulent channel flow.

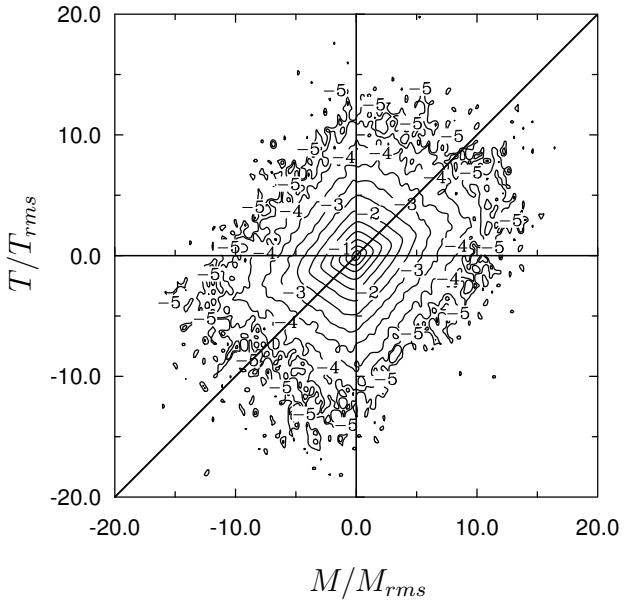

(a)

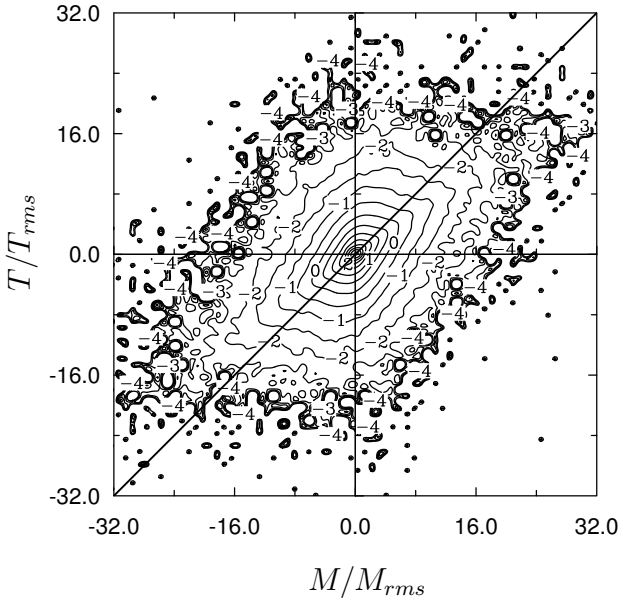

(b)

Figure 4.10: Contour plots of logarithm of the joint PDF of the total SS advection term T and the modeled SS advection term M for $i \neq j$, $j \neq k$ ($i = 3$, $k = 1$, $j = 2$): (a) forced isotropic turbulence; (b) turbulent channel flow.

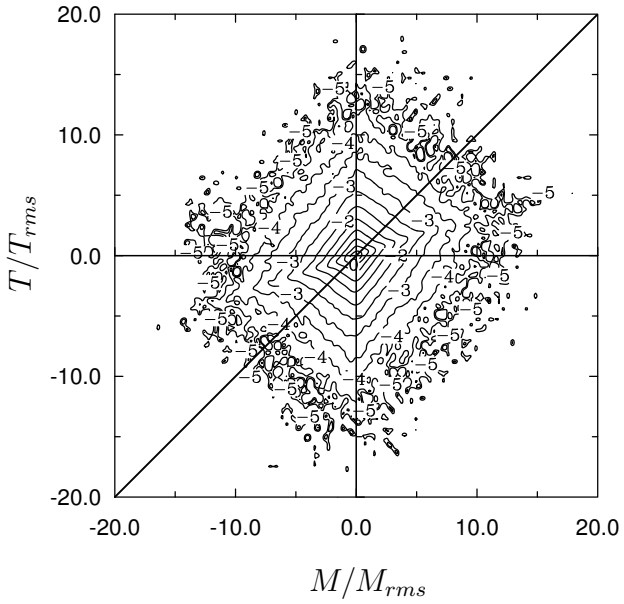

(a)

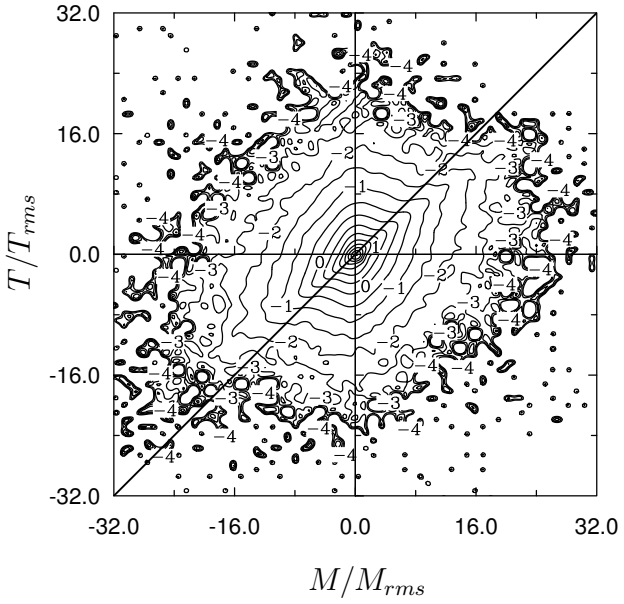

(b)

Figure 4.11: Contour plots of logarithm of the joint PDF of the total SS advection term T and the modeled SS advection term M for $i = j$, $j \neq k$ ($i = 2$, $j = 2$, $k = 1$): (a) forced isotropic turbulence; (b) turbulent channel flow.

are more dominant. The SS convective derivatives in other directions (streamwise and spanwise) exhibit similar qualitative behavior and are not shown for brevity. Because of this characteristic PDF shape, a similar qualitative reasoning, which has been used for the SS second derivatives, is applicable here too (see Figure 4.8). Therefore, the model assumption (ii) would correspond to a case when the SS convective derivatives consistently admit values higher in magnitude than the most probable values of the total SS convective derivatives. Qualitatively, it means that the modeled SS field is subject to higher distortion by the SS advection than the exact SS field.

The SS Eq. (4.26) allows reconstruction of the SS velocity on line l_k if the LS velocity is known. Physically, the LS velocity evolves on a slower time scale than the SS velocity and requires discretization with a bigger time step. To close the LS equation it is not necessary to resolve the fast SS dynamics at all times, one only needs to know the SS velocity field at particular instants of the slow LS time t^L. To achieve this, one can integrate Eq. (4.26) in small neighborhood of t^L_m treating the LS velocity as a locally time independent field. In other words, for any LS time t^L_m and a small parameter $\epsilon \ll 1$, we introduce a local time coordinate $t^S = \epsilon t$ according to the transformation: $t \longrightarrow t^L_m + t^S$ such that $u^L(l_k, t) \longrightarrow u^L(l_k, t^L_m)$ and $u^S(l_k, t) \longrightarrow u^S(l_k, t^L_m + t^S)$. The SS velocity evolves from zero initial state and depends only on the LS velocity and its derivatives.

Physically, evolution of the SS velocity according to Eq. (4.26) is interpreted as the propagation of energy disturbances down into the SS part of the turbulent spectrum due to non-linear interaction. Starting from a zero initial state, the SS velocity starts growing, continuously exciting smaller scales until the viscous dissipation region is reached. The term $[u^L_i u^L_j]^S$, which is the only non-zero term at $t^S = 0$, acts as a constant source of energy for the small scales, triggering the forward energy cascade. Note that even though the LS velocity is kept fixed in time t^S, this problem does not constitute an evolution of the SS velocity in the "frozen" LS environment. The time t^S corresponds to the time needed to "fill up" the SS part of the spectrum. As a result, the SS velocity at some instant of time t^L_m does not depend on the SS solution at previous time t^L_{m-1}, i.e., it is memoryless, and is solely defined by the LS velocity and its derivatives at t^L_m. The evolution time needed to reconstruct the SS velocity field is determined by matching the LS and the SS energies at the minimal scale resolvable by the LS grid. Clearly, this time is unique for different lines and fully defined by the LS velocity, its derivatives and viscosity. This is further illustrated in Figs. 6.6(a,b) and the corresponding discussion in Section 6.2.

4.3 TLS Numerical Algorithm

Numerical implementation of TLS is based on the simulation of the LS equations coupled with the simplified SS equations which approximate the SS turbulent fields on lines. The line arrangement constitutes an important part of the SS model. The optimal line placement and its affect on the reconstructed SS field, due to neglecting the transverse SS advection, on its own present non-trivial, challenging problem. The ideal line arrangement is the case when the lines are exact streamlines of the SS

velocity field. Here, the line arrangement depicted in Figure 4.3 is adopted. Given the LS grid and the SS line arrangement, there are four steps involved in the TLS algorithm:

(i) At the m-th time step t_m^L, interpolate u_i^L and p^L onto each line l_k, such that:

$$u_i^L(\mathbf{x}_\mathrm{n}, t_m^L) \longrightarrow u_{i,l_k}^L(l_k, t_m^L), \quad p^L(\mathbf{x}_\mathrm{n}, t_m^L) \longrightarrow p_{l_k}^L(l_k, t_m^L), \quad \mathbf{x}_\mathrm{n} \in l_k$$

(ii) Evolve Eq. (4.26) on each line l_k with zero initial condition and corresponding boundary conditions until the SS energy is matched with the LS energy at the LS grid minimal resolvable scale to obtain the SS velocity field $u_{i,l_k}^S(l_k, t_m^L)$;

(iii) For all LS grid points $\mathbf{x}_\mathrm{n}$ calculate the mutual tensor product of the SS velocity $[u_i^S u_j^S]^L$ as well as the mixed tensor products $[u_i^S u_j^L]^L$ and $[u_i^L u_j^S]^L$ by averaging over three lines intersecting at the LS grid point $\mathbf{x}_\mathrm{n}$ belonging to a cell ΔV_n, according to Eq. (4.24):

$$[u_i^S u_j^S]^L(\mathbf{x}_\mathrm{n}, t_m^L) \longleftarrow \left[u_{i,l_k}^S u_{j,l_k}^S(l_k, t_m^L)\right]_{l_k}, \quad [u_i^S u_j^L]^L(\mathbf{x}_\mathrm{n}, t_m^L) \longleftarrow \left[u_{i,l_k}^S u_{j,l_k}^L(l_k, t_m^L)\right]_{l_k}$$

(iv) Advance the LS fields $u_i^L(\mathbf{x}_\mathrm{n}, t_m^L)$, $p^L(\mathbf{x}_\mathrm{n}, t_m^L)$ to the next time level $t_{m+1}^L = t_m^L + \Delta t^L$ by integrating the LS equations (Eqs. (4.5), (4.21a)).

CHAPTER V

NUMERICAL METHOD

5.1 Large-Scale Equation

Incompressible flow constitutes an important model of fluid flow encountered in many real life situations, ranging from air and water flows in pipes and around low-speed vehicles till fish swimming and the blood flow in living organisms. As a result, extensive research efforts have been performed for decades to develop numerical algorithms and computational tools suitable for incompressible flow problems in both basic research and engineering applications (for reviews, see [62], [63]). In the present study, the incompressible, constant density Navier-Stokes equations are adopted to describe the LS dynamics of turbulent flows.

Major difficulty in treating the incompressible Navier-Stokes equations numerically stems from a lack of a natural evolution equation for pressure. Instead, pressure plays a corrective role for velocity field such that the continuity equation (incompressibility requirement) is satisfied everywhere in the flow field. Physically, it means that pressure disturbances travel at infinite speed, which leads to stringent requirements on numerical algorithms. In principle, pressure can be excluded from consideration by taking the curl of the momentum equation and introducing vorticity. This results in different sets of the governing equations and leads the vorticity-velocity or the vorticity-stream function methods (see, for example, [64], [65]). Giving physically appealing formulation for vortex-dominated flows and being successful for two-dimensional flows, the vorticity-velocity formulation has not gained much popularity for three-dimensional applications compared with traditional approaches based on primitive variables, i.e., velocity and pressure. One of the drawbacks of the vorticity-velocity methods is that the number of flow variables increases from four (u_i, p) to six (ω_i, u_i, $i = 1, 2, 3$). This makes the governing equations more expensive to solve numerically, especially in the context of high-Re number turbulent flows. Another common problem of these methods is the absence of boundary conditions for vorticity in the presence of solid walls. Some recent developments to reduce computational expenses by decoupling vorticity and velocity integration in space and time has been reported by [66]. There have been very few applications of the vorticity-velocity formulation to simulate high-Re number turbulent flows and the corresponding literature remains scarce. LES of spatially evolving 3D turbulent mixing layer was conducted by [67].

There are two approaches which allow to overcome numerical difficulty to enforce the incompressibility constraint. The first approach is known as the artificial compressibility method originally suggested by [68]. It uses an artificial compressibility parameter $\beta = c_0^2 \rho_0$, where c_0 is the artificial speed of sound, to couple the divergence of the velocity to a change of pressure in pseudo-time τ, thus providing an evolution

equation for pressure. Time accurate solution requires sub-iteration of the equation in pseudo-time until the divergence of velocity is reduced to the desired accuracy. The key difficulty here lies in constructing an iteration scheme and optimizing β and the time step Δ_τ that provides fast convergence to a stationary state ([69]). The time step Δ_τ is limited by the inverse of c_0^2 which results in very small time steps when simulating incompressibility $c_0 \to 0$. As a result, the artificial compressibility method can be very costly.

The second, and probably the most popular strategy is based on operator splitting. This means that the system of governing equations is split into series of simple standard equations such as advection equation, diffusion equation, advection-diffusion equation, Poisson equation, and combined with explicit/implicit updates in time. Then, it becomes much easier to construct an efficient numerical schemes for each equation separately than for the original system directly. Methods which belong to this category appear in literature under different names such as pressure-correction methods, projection methods, fractional step methods, or sometimes they are generally referred as the "pressure based" methods. A common feature of operator splitting methods is that at certain stage the predicted velocity field is computed neglecting the incompressibility condition. Then, the velocity is corrected by "projection" onto divergence free fields.

Historically, [70] were the first who suggested an operator splitting method in mid 60's. In this method, called MAC (marker-and-cell), the second order finite difference discretization of the governing equation is implemented on a staggered grid with explicit treatment of the nonlinear and viscous terms, and the implicit treatment of the pressure term. Application of the incompressibility constraint to the discretized momentum equation results in the discrete Poisson equation providing the effective decoupling of the computation of the momentum and kinematic equations. Many shortcomings of the MAC method such as inability to handle regular grids, low order time discretization, time consuming iterative procedure for pressure had been successfully addressed in the intervening years.

The widely used SIMPLE (semi-implicit method for pressure linked equations) method developed by [71] employs simplified iterative procedure to estimate the pressure correction. This significantly simplifies computation but with a price of introducing empirical assumptions in the method ([72]). In late 60's [73] and [74] introduced the projection method which allows implicit treatment of the viscous term. In the projection method the intermediate velocity field u_i^* is computed first using the momentum equation, in which the pressure gradient is excluded entirely, or computed based on pressure values at the previous time step. In the second step, the intermediate velocity u_i^* is projected onto the space of divergence-free vector fields to compute u_i by solving a Poisson equation for the pressure. This procedure is often referred literature as the fractional step method. However, the time splitting introduces a numerical boundary layer in pressure and the intermediate velocity fields. It signifies the main difficulty in implementation of the projection method which is the treatment of boundary conditions for the intermediate velocity and pressure. Structure of the numerical boundary layer is strongly affected by numerical boundary condition for pressure at the projection step ([75]).

There are three main ways to decouple pressure and velocity computations to achieve the second-order accuracy. These result in projection methods based on: (1) accurate boundary condition for the intermediate velocity field ([76]); (2) accurate boundary condition for pressure ([77]); (3) pressure increment formulation ([78], [79]). They are by far the most popular methods used for practical simulations of high-Re number turbulent flows since the strength of the numerical boundary layer decreases with the increase of the Reynolds number.

In the formulation developed by Kim and Moin pressure gradient does not appear in the momentum equation for the intermediate velocity. Homogeneous Neumann boundary condition for pressure is used together with an inhomogeneous boundary condition for u_i^* such that u_i at the boundary is of $\mathcal{O}(\Delta t^2)$ order of accuracy. In the formulation based on accurate pressure boundary condition, the homogeneous Dirichlet boundary condition for the intermediate velocity u_i^* is retained. An inhomogeneous Neumann boundary condition for pressure is introduced so that u_i at the boundary is of the second order of accuracy in time. In the incremental pressure projection methods, the projection step serves to compute an incremental correction of the pressure gradient. The accuracy of this method near the boundary was extensively discussed by several authors, including among others, [80] and [81].

In the present study, the incremental pressure projection method of [79] is used to solve the LS fields governing equations. In the following paragraphs, spatial and temporal discretization are briefly described.

5.1.1 Spatial Discretization

3D Cartesian grid with a staggered arrangement is employed for spatial discretization. The staggered grid arrangement has proven useful for LES and DNS. It naturally conserves mass, momentum, kinetic energy and avoids oscillatory or checkerboard pressure solutions encountered on regular grids ([82]). Figure 5.1(a) shows a staggered computational volume cell ΔV, where the LS pressure p^L is defined at the cell center and LS velocities u_i^L are defined at the corresponding cell faces.

The finite volume (FV) approach is employed for the spatial discretization of the LS governing equations. Accordingly, the LS continuity and the LS momentum equations can be rewritten as local conservation laws based on application of the Ostrogradsky-Gauss theorem to a computational volume cell ΔV. Namely, for a continuously differentiable vector field ψ_i one has:

$$\iiint_{\Delta V} \frac{\partial \psi_i}{\partial x_i} \mathrm{d}v = \iint_{\partial \Delta V} \psi_i n_i \mathrm{d}\sigma, \tag{5.1}$$

where n_i is a unit normal vector to surface $\partial \Delta V$. As a result, the spatially discretized LS Eq. (4.5), when it is written for a computational volume cell ΔV, takes the

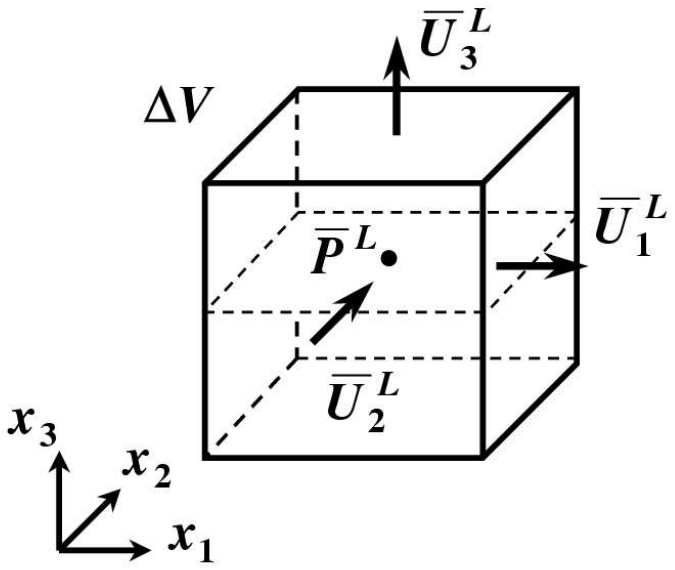

(a)

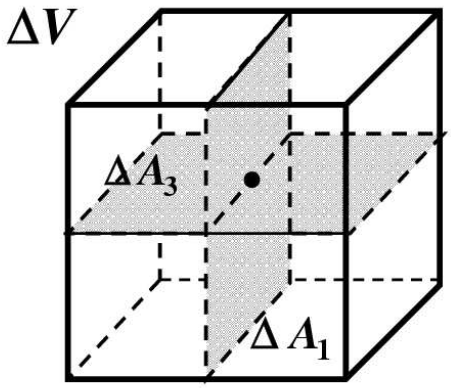

(b)

Figure 5.1: (a) A staggered grid arrangement in computational cell ΔV; (b) position of the orthogonal surfaces ΔA_i in computational cell ΔV

following form:

$$|\Delta V|\frac{\partial}{\partial t}\overline{u_i^L}^{\Delta V} = \sum_{j=1}^{3}\Big[|\Delta A_j^+|\Big(\overline{\nu D_{ij}^L}^{\Delta A_j^+} - \overline{\big[u_i^L u_j^L\big]^L}^{\Delta A_j^+} - \overline{\big[u_i^S u_j^S\big]^L}^{\Delta A_j^+} - \overline{\big[u_i^S u_j^L + u_i^L u_j^S\big]^L}^{\Delta A_j^+}\Big) - |\Delta A_j^-|\Big(\overline{\nu D_{ij}^L}^{\Delta A_j^-} - \overline{\big[u_i^L u_j^L\big]^L}^{\Delta A_j^-} - \overline{\big[u_i^S u_j^S\big]^L}^{\Delta A_j^-} - \overline{\big[u_i^S u_j^L + u_i^L u_j^S\big]^L}^{\Delta A_j^-}\Big)\Big] - \Big(|\Delta A_j^+|\overline{p^L}^{\Delta A_j^+} - |\Delta A_j^-|\overline{p^L}^{\Delta A_j^-}\Big). \tag{5.2}$$

Similarly, the mass conservation is given by:

$$\sum_{j=1}^{3}\Big[|\Delta A_j^+|\overline{u_j^L}^{\Delta A_j^+} - |\Delta A_j^-|\overline{u_j^L}^{\Delta A_j^-}\Big] = 0 \tag{5.3}$$

The diffusion term D_{ij}^L in Eq. (5.2) is expressed through the LS rate-of-strain tensor

$$D_{ij}^L = 2S_{ij}^L - \frac{2}{3}S_{kk}^L\delta_{ij}, \quad S_{ij}^L = \frac{1}{2}\Big(\frac{\partial u_i^L}{\partial x_j} + \frac{\partial u_j^L}{\partial x_i}\Big) \tag{5.4}$$

In these equations, ΔA_j^+ and ΔA_j^- denote surfaces of the computational volume ΔV which correspond to positive and negative directions of the flux caused by the j-th component of the LS velocity. The bar symbols stand for corresponding integral averages over the specified region of ΔV, for example:

$$\overline{\psi_i}^{\Delta V} = \frac{1}{|\Delta V|}\iiint_{\Delta V}\psi_i \mathrm{d}v, \quad \overline{\psi_i}^{\Delta A_j^+} = \frac{1}{|\Delta A_j^+|}\iint_{\Delta A_j^+}\psi_i \mathrm{d}\sigma \tag{5.5}$$

Note that, due to the staggered grid arrangement, the components of the LS velocity are defined on the corresponding surfaces of the pressure-centered volume cell ΔV. Therefore, the discrete momentum equation for the specific LS velocity component is derived based on integration over the corresponding computational volume cell which is centered around this component, as shown in Fig. 5.1(a). However, since the integration is performed over the surfaces as well as the volume of ΔV, the system of Eqs. (5.2), (5.3) contains more unknowns than equations. A necessary simplification is achieved by adopting the following approximation for any volume or surface averaged variable ψ_i:

$$\overline{\psi_i} = \overline{\psi_i}^{\Delta V} \approx \overline{\psi_i}^{\Delta A_j} \approx \overline{\psi_i}^{\Delta A_i} \tag{5.6}$$

For an orthogonal volume cell ΔV and orthogonal surfaces ΔA_i that pass through the cell center, as shown in Fig. 5.1(b), such an assumption results in a local error of order $\mathcal{O}(\Delta x_i^2)$, where Δx_i is the cell size in x_i coordinate direction. For example, for ΔV depicted in Fig. 5.1(b), one has:

$$\overline{\psi_i}^{\Delta V} = \frac{1}{|\Delta V|}\iiint_{\Delta V}\psi_i \mathrm{d}v = \frac{|\Delta A_1|}{|\Delta V|}\int_{\Delta x_1}\Big[\frac{1}{|\Delta A_1|}\iint_{\Delta A_1}\psi_i \mathrm{d}\sigma\Big]\mathrm{d}x_1 = \frac{|\Delta A_1|}{|\Delta V|}\int_{\Delta x_1}\overline{\psi_i}^{\Delta A_1}\mathrm{d}x_1 = \overline{\psi_i}^{\Delta A_1}(\xi), \quad \xi \in \Delta x_1$$

which gives $\mathcal{O}(\Delta x_i^2)$ error, if ξ is a center point of Δx_1 according to the midpoint rule of Newton-Cotes quadrature formula. In addition, the averaged LS nonlinear convective term can be further approximated as

$$\overline{[u_i^L u_j^L]^L}^{\Delta A_j} = \frac{1}{|\Delta A_j|}\iint_{\Delta A_j}\left[u_i^L u_j^L\right]^L \mathrm{d}\sigma = \frac{1}{|\Delta A_j|}\iint_{\Delta A_j}\left(u_i^L u_j^L - \left[u_i^L u_j^L\right]^S\right)\mathrm{d}\sigma =$$
$$\overline{u_i^L u_j^L}^{\Delta A_j} - \overline{\left[u_i^L u_j^L\right]^S}^{\Delta A_j} \approx \overline{u_i^L u_j^L}^{\Delta A_j}, \tag{5.7}$$

since the Leonard stress $[u_i^L u_j^L]^S$ is the SS quantity, and as a result, can not be fully captured on the LS grid ([12]).

Denoting all averaged quantities by the bar symbol, the LS system of continuity and momentum equations takes the following form:

$$\frac{\partial}{\partial t}\overline{u_i^L} = \frac{1}{|\Delta V|}\sum_{j=1}^{3}\Big[|\Delta A_j^+|\Big(\overline{\nu D_{ij}^L} - \overline{u_i^L u_j^L} - \overline{\left[u_i^S u_j^S\right]^L} - \overline{\left[u_i^S u_j^L + u_i^L u_j^S\right]^L}\Big)$$
$$-|\Delta A_j^-|\Big(\overline{\nu D_{ij}^L} - \overline{u_i^L u_j^L} - \overline{\left[u_i^S u_j^S\right]^L} - \overline{\left[u_i^S u_j^L + u_i^L u_j^S\right]^L}\Big)\Big] \tag{5.8}$$
$$-\frac{1}{|\Delta V|}\Big(|\Delta A_j^+|\overline{p^L} - |\Delta A_j^-|\overline{p^L}\Big),$$

$$\sum_{j=1}^{3}\Big[|\Delta A_j^+|\overline{u_j^L} - |\Delta A_j^-|\overline{u_j^L}\Big] = 0 \tag{5.9}$$

The spatially discretized (semi-discretized) form of the LS equations is obtained from Eqs. (5.8), (5.9) when the LS grid variable $\psi_{\mathrm{i,j,k}}$, associated with the cell center $\mathbf{x}_{\mathrm{i,j,k}}$ of ΔV, is considered to be an approximation to the averaged value $\overline{\psi}$. To complete the discretization, all fluxes at cell surfaces ΔA_i need to be defined based on values of dependent variables at adjacent cells. The convective and diffusion fluxes in Eq. (5.8) may be approximated in different ways. In the present work, all diffusion terms are computed using second order central differencing. The convective flux terms are reconstructed using third order polynomial interpolation resulting in the forth-order accurate central scheme.

5.1.2 Temporal Discretization

The third-order explicit Runge-Kutta scheme is employed in the time integration algorithm. Subsuming all terms on the right hand side of Eq. (5.8) in $\mathbf{F}(\overline{u_i^L}, t)$, the three-stage Runge-Kutta scheme to advance Eq. (5.8) over a step Δt is given by

$$\overline{u_i^L}^{n+1} = \overline{u_i^L}^n + \sum_{j=1}^{3} w_j \mathbf{K}_j, \quad \mathbf{K}_j = \Delta t \mathbf{F}\Big(\overline{u_i^L}^n + \sum_{l=1}^{j-1}\beta_{jl}\mathbf{K}_l, \quad t^n + \alpha_j \Delta t\Big), \quad \sum_{j=1}^{3} w_j = 1 \tag{5.10}$$

Here, coefficients w_j and β_{jl} have to be chosen in such a way that $\overline{u_i^L}^n$ approximates the solution to the appropriate order of accuracy. The coefficients α_j are given by the

row-sum conditions

$$\alpha_j = \sum_{l=1}^{j-1} \beta_{jl} \tag{5.11}$$

An efficient, low-storage variant of the Runge-Kutta scheme, initially proposed by [83], is defined by the following values of these coefficients

$$\begin{aligned} &w_1 = \frac{1}{6}, \quad w_2 = \frac{3}{10}, \quad w_3 = \frac{8}{15} \\ &\beta_{21} = \frac{1}{3}, \quad \beta_{31} = -\frac{3}{16}, \quad \beta_{32} = \frac{15}{16} \\ &\alpha_1 = 0, \quad \alpha_2 = \frac{1}{3}, \quad \alpha_3 = \frac{3}{4} \end{aligned} \tag{5.12}$$

In the present work, the three-stage Runge-Kutta scheme given by Eqs. (5.10), (5.12) is used to integrate the LS Eq. (5.8), with an exception of the diffusion terms in the transverse (wall-normal) direction x_3, which are treated implicitly using Crank-Nicoloson scheme. Equations (5.10), (5.12) results in three-step advancements scheme which is can be written as:

$$\begin{aligned} \overline{u_i^L}^{(1)} &= \overline{u_i^L}^n + \Delta t\Big[\gamma_1 \mathbf{N}(\overline{u_i^L}^n) + \frac{1}{2}\omega_1\Big(\mathbf{D}(\overline{u_i^L}^n) + \mathbf{D}(\overline{u_i^L}^{(1)})\Big)\Big] - \omega_1 \Delta t \mathbf{P}, \\ \overline{u_i^L}^{(2)} &= \overline{u_i^L}^{(1)} + \Delta t\Big[\gamma_2 \mathbf{N}(\overline{u_i^L}^{(1)}) + \xi_2 \mathbf{N}(\overline{u_i^L}^n) + \\ &+ \frac{1}{2}\omega_2\Big(\mathbf{D}(\overline{u_i^L}^{(1)}) + \mathbf{D}(\overline{u_i^L}^{(2)})\Big)\Big] - \omega_2 \Delta t \mathbf{P}, \\ \overline{u_i^L}^{n+1} &= \overline{u_i^L}^{(2)} + \Delta t\Big[\gamma_3 \mathbf{N}(\overline{u_i^L}^{(2)}) + \xi_3 \mathbf{N}(\overline{u_i^L}^{(1)}) + \frac{\xi_3\xi_2}{\gamma_2}\mathbf{N}(\overline{u_i^L}^n) + \\ &+ \frac{1}{2}\omega_3\Big(\mathbf{D}(\overline{u_i^L}^{(2)}) + \mathbf{D}(\overline{u_i^L}^{n+1})\Big)\Big] - \omega_3 \Delta t \mathbf{P} \end{aligned} \tag{5.13}$$

Here, $\mathbf{N}$ denotes all convective and diffusion terms in Eq. (5.8), except the implicitly treated diffusion terms in x_3 direction. $\mathbf{D}$ and $\mathbf{P}$ stand for the diffusion terms in x_3 direction and pressure terms respectively. Also, $\overline{u_i^L}^n$, $\overline{u_i^L}^{n+1}$ are the LS velocities at the beginning and end of the time step, and $\overline{u_i^L}^{(1)}$, $\overline{u_i^L}^{(2)}$ correspond to the LS velocities at intermediate substeps. The advancement procedure given by Eqs. (5.13) represents time integration with three time substeps $\Delta t^1 = \omega_1 \Delta t$, $\Delta t^2 = \omega_2 \Delta t$, $\Delta t^3 = \omega_3 \Delta t$. All time advancement parameters ξ_i, γ_i and ω_i are related to those in Eq. (5.12) ([83]), and given by

$$\begin{aligned} &\omega_1 = \alpha_2 = \frac{1}{3}, \quad \omega_2 = \alpha_3 - \alpha_2 = \frac{5}{12}, \quad \omega_3 = 1 - \alpha_3 = \frac{1}{4}, \\ &\gamma_1 = \beta_{21} = \frac{1}{3}, \quad \gamma_2 = \beta_{32} = \frac{15}{16}, \quad \gamma_3 = w_3 = \frac{8}{15}, \\ &\xi_2 = \frac{\beta_{32}}{w_2}(w_1 - \beta_{21}) = -\frac{25}{48}, \quad \xi_3 = w_2 - \beta_{32} = -\frac{51}{80} \end{aligned} \tag{5.14}$$

Due to the absence of a transport equation for the LS pressure, the fractional step method of [79] is used to satisfy the continuity constraint (Eq. (5.9)). The method

is based on introduction of the pressure increment ψ and applied at every discrete time instant t^k determined by the Runge-Kutta time substeps Δt^k (k = 1,2,3), i.e., $t^k = t^{k-1} + \Delta t^k$. Note that in this notation time instants $t^{(3)}$ and $t^{(0)}$ coincide with t^{n+1} and t^n respectively. The LS pressure during time integration substeps can be further split into some approximate value p_0^L and the pressure increment ψ

$$\Delta t^k \mathbf{P} = \int_{t^k}^{t^{k+1}} \frac{\partial \overline{p^L}}{\partial x_i} \mathrm{d}t = \Delta t^k \frac{\partial p_0^L}{\partial x_i} + \Delta t^k \frac{\partial \psi}{\partial x_i} \tag{5.15}$$

In the present implementation, the value of pressure from the previously computed time step is chosen as p_0^L, i.e., $p_0^L = \overline{p^L}^k$. However, different specifications of the approximate pressure p_0^L is possible ($p_0^L = 0$, for example) which lead to slightly different variations of the fractional step method ([76]).

Upon denoting all the convective and diffusion terms in squire brackets of Eq. (5.13) by $\mathbf{F}_k$ for brevity, and using Eq. (5.15), Eq. (5.13) takes the following form for each discrete instant of time t^k:

$$\overline{u_i^L}^{k+1} = \overline{u_i^L}^k + \Delta t \mathbf{F}_k - \Delta t^k \frac{\partial \overline{p^L}^k}{\partial x_i} - \Delta t^k \frac{\partial \psi}{\partial x_i} \tag{5.16}$$

Since the pressure correction ψ is not known at this stage, Eq. (5.16) is integrated in two steps, which gives rise to the intermediate LS velocity field $\overline{u_i^L}^*$ according to

$$\overline{u_i^L}^* = \overline{u_i^L}^k + \Delta t \mathbf{F}_k - \Delta t^k \frac{\partial \overline{p^L}^k}{\partial x_i}, \quad \overline{u_i^L}^*|_{\partial\Omega} = \overline{u_i^B} \tag{5.17}$$

$$\overline{u_i^L}^{k+1} = \overline{u_i^L}^* - \Delta t^k \frac{\partial \psi}{\partial x_i}, \quad \overline{u_i^L}^{k+1}|_{\partial\Omega} = \overline{u_i^B}, \tag{5.18}$$

where $\overline{u_i^B}$ is the corresponding LS velocity specified at the boundary $\partial\Omega$.

Enforcing the continuity constraint for the LS velocity at the next $k+1$ time level, by taking divergence of Eq. (5.18), results in the Poisson equation for ψ with homogeneous Neumann boundary condition.

$$\frac{\partial^2 \psi}{\partial x_i^2} = \frac{1}{\Delta t^k} \frac{\partial \overline{u_i^L}^*}{\partial x_i}, \quad \frac{\partial \psi}{\partial n}|_{\partial\Omega} = 0. \tag{5.19}$$

The prescribed boundary condition for ψ follows from Eq. (5.17) and the chosen boundary condition for $\overline{u_i^L}^*$. Equation (5.19) is solved for ψ, at each Runge-Kutta time step. The "corrected" value of the LS velocity at $k+1$ time level is then given by Eq. (5.18), and the LS pressure is updated as

$$\overline{p^L}^{k+1} = \overline{p^L}^k + \psi \tag{5.20}$$

While the adopted boundary condition for $\overline{u_i^L}^*$ guarantees the second order of accuracy in time ($\mathcal{O}(\Delta t^2)$) for velocity, the pressure is only of the first order accurate ([81]).

From taking gradient of Eq. (5.20) it is seen that the normal component of the pressure gradient remains the same ($\partial_n \overline{p^L}^{k+1} = \partial_n \overline{p^L}^k$), for all k, which is not true in general. Equation (5.20) is consequence of the definition of ψ given by Eq. (5.15). This equation is essentially the integral mean value theorem for $\overline{p^L}^{k+1}$ which gives $\mathcal{O}(\Delta t)$ accuracy in time. Diminishing accuracy in the pressure manifests itself as a numerical boundary layer which has been extensively analyzed in literature by [75], [80] and others. However, a simple modification to Eq. (5.20) given by

$$\overline{p^L}^{k+1} = \overline{p^L}^k + \psi - \frac{\nu \Delta t^k}{2} \nabla^2 \psi \tag{5.21}$$

restores the second order accuracy in the pressure ([81]). Note that the effect of the numerical boundary layer is less pronounced for high-Re flows and decreases with increasing Reynolds number which explains the popularity of the adopted approach for high-Re LES studies of incompressible flows.

The pressure increment Poisson Eq. (5.19) is solved by employing the standard fast Fourier transform in periodic directions and the tri-diagonal matrix algorithm for non-homogeneous directions.

5.2 Small-Scale Equation

The SS velocity field is reconstructed on lines by solving numerically the SS equation (Eq. (4.26)). While various numerical schemes can be proposed to integrate Eq. (4.26) depending on the required computational effectiveness and accuracy, two qualitative aspects of the SS velocity need to be taken into account in constructing numerical scheme. First, it is expected that the SS velocity can be highly intermittent, especially in flow regions with high LS velocity gradients. Thus, it is desirable to use a numerical scheme which does not introduce possible, spurious oscillations in presence of high gradients. The total variation diminishing (TVD) schemes, introduced by [84] and widely used for hyperbolic conservation laws, have this property of being oscillation-free across discontinuities. Second, due to expected uniqueness of the SS field in the decomposition Eq. (4.3), the SS might reach a stationary state. Therefore, a numerical scheme employed for numerical integration of Eq. (4.26) should recognize stationary solutions. In the present work, an explicit, two-step component-wise TVD scheme of [85] is employed to numerically integrate the SS Eq. (4.26), and is briefly described in what follows.

With respect to a line l_k Eq. (4.26) can be written on non-homogeneous conservative form

$$\frac{\partial u_i^S}{\partial t} + \frac{\partial}{\partial x_k} F_i(u_i^S, u_k^S) + S_i(u_i^S, u_k^S) = 3\nu \frac{\partial^2 u_i^S}{\partial x_k^2} + F_i^L, \tag{5.22}$$

where on the LS and SS velocities as follows

$$F_i = \big(u_k^L + u_k^S(l_k)\big)\big(u_i^L + u_i^S(l_k)\big), \quad S_i = \frac{\partial}{\partial x_j} \underbrace{\big(u_j^L + u_j^S(l_k)\big)\big(u_i^L + u_i^S(l_k)\big)}_{j \neq k} \tag{5.23}$$

In expression for the source term S_i summation over j index is assumed, however only for $j \neq k$.

The adopted two-step TVD scheme of [85] is based on the MacCormack scheme, and is constructed by adding a pure flux limiter to the second order antidiffusive term in the expression of the numerical fluxes. This TVD scheme has an advantage of not requiring the characteristic decomposition of usual TVD schemes, and employs component-wise flux limiting.

To ease notation, it is convenient to represent Eq. (5.22) in the vector form. Introducing column vectors: $\mathrm{U} = (u_1^S, u_2^S, u_3^S)^\top$, $\mathrm{S} = (S_1, S_2, S_3)^\top$, $\mathrm{F} = (F_1, F_2, F_3)^\top$ and $\mathrm{F}^L = (F_1^L, F_2^L, F_3^L)^\top$, one can rewrite Eq. (5.22) as

$$\frac{\partial \mathrm{U}}{\partial t} + \frac{\partial \mathrm{F}}{\partial x_k} + \mathrm{S} = 3\nu \frac{\partial^2 \mathrm{U}}{\partial x_k^2} + \mathrm{F}^L, \tag{5.24}$$

where

$$\begin{aligned}
F_1 &= \big(u_k^L + u_k^S\big)\big(u_1^L + u_1^S\big), \quad S_1 = \sum_{j\neq k} \frac{\partial}{\partial x_j}\big(u_j^L + u_j^S\big)\big(u_1^L + u_1^S\big), \\
F_2 &= \big(u_k^L + u_k^S\big)\big(u_2^L + u_2^S)\big), \quad S_2 = \sum_{j\neq k} \frac{\partial}{\partial x_j}\big(u_j^L + u_j^S\big)\big(u_2^L + u_2^S\big), \\
F_3 &= \big(u_k^L + u_k^S\big)\big(u_3^L + u_3^S\big), \quad S_3 = \sum_{j\neq k} \frac{\partial}{\partial x_j}\big(u_j^L + u_j^S\big)\big(u_3^L + u_3^S\big)
\end{aligned} \tag{5.25}$$

The predictor step of the second-order TVD scheme then takes the following form

$$\frac{\tilde{\mathrm{U}}_{\mathrm{j}}^{n+1} - \mathrm{U}_{\mathrm{j}}^n}{\Delta t} = -\frac{\big(\widehat{\mathrm{F}}_{\mathrm{j}+1/2} - \widehat{\mathrm{F}}_{\mathrm{j}-1/2}\big)}{l_{\mathrm{j}+1/2} - l_{\mathrm{j}-1/2}} - \mathrm{S}_{\mathrm{j}+1/2} + \mathrm{D}_{\mathrm{j}} + \mathrm{F}_{\mathrm{j}}^L \tag{5.26}$$

$$\widehat{\mathrm{F}}_{\mathrm{j}+1/2} = \mathrm{F}_{\mathrm{j}}^+ + \mathrm{F}_{\mathrm{j}+1}^-, \quad \mathrm{F}_{\mathrm{j}}^\pm = \frac{1}{2}\big(\mathrm{F}(\mathrm{U}_{\mathrm{j}}) \pm \alpha_{\mathrm{j}} \mathrm{U}_{\mathrm{j}}\big), \tag{5.27}$$

where l_{j} stands for a discrete value of the coordinate x_k and D_{j} is the discretized diffusion term at l_{j} node. The corrected value of the velocity vector $\mathrm{U}_{\mathrm{j}}^{n+1}$ is based on the predicted value $\tilde{\mathrm{U}}_{\mathrm{j}}^{n+1}$ and given by

$$\frac{\mathrm{U}_{\mathrm{j}}^{n+1} - \mathrm{U}_{\mathrm{j}}^n}{\Delta t} = -\frac{\big(\widehat{\mathrm{H}}_{\mathrm{j}+1/2} - \widehat{\mathrm{H}}_{\mathrm{j}-1/2}\big)}{l_{\mathrm{j}+1/2} - l_{\mathrm{j}-1/2}} - \frac{1}{2}\big(\mathrm{S}_{\mathrm{j}+1/2} + \tilde{\mathrm{S}}_{\mathrm{j}-1/2} - \mathrm{D}_{\mathrm{j}} - \tilde{\mathrm{D}}_{\mathrm{j}}\big) + \tilde{\mathrm{F}}_{\mathrm{j}}^L, \tag{5.28}$$

where the numerical flux $\widehat{\mathrm{H}}_{\mathrm{j}}$ is the modified $\widehat{\mathrm{F}}_{\mathrm{j}}$ flux according to

$$\widehat{\mathrm{H}}_{\mathrm{j}+1/2} = \widehat{\mathrm{F}}_{\mathrm{j}+1/2} + \frac{1}{2}\Big[\varphi\big(r_{\mathrm{j}+1/2}^+\big)\widehat{\mathrm{G}}_{\mathrm{j}+1/2}^+ - \varphi\big(r_{\mathrm{j}+1/2}^-\big)\widehat{\mathrm{G}}_{\mathrm{j}+1/2}^-\Big], \tag{5.29}$$

where the slope ratio is defined by

$$r_{\mathrm{j}+1/2}^+ = \frac{\widehat{\mathrm{G}}_{\mathrm{j}-1/2}^+}{\widehat{\mathrm{G}}_{\mathrm{j}+1/2}^+}, \quad r_{\mathrm{j}+1/2}^- = \frac{\widehat{\mathrm{G}}_{\mathrm{j}+3/2}^-}{\widehat{\mathrm{G}}_{\mathrm{j}+1/2}^-} \tag{5.30}$$

$$\widehat{\mathrm{G}}_{\mathrm{j}+1/2}^+ = \tilde{\mathrm{F}}_{\mathrm{j}+1}^+ - \mathrm{F}_{\mathrm{j}}^+, \quad \widehat{\mathrm{G}}_{\mathrm{j}+1/2}^- = \mathrm{F}_{\mathrm{j}+1}^- - \tilde{\mathrm{F}}_{\mathrm{j}}^- \tag{5.31}$$

Note that in case of $\varphi(r) = 1$, Eqs. (5.26), (5.28) lead to the standard MacCormack scheme. If a flux limiter $\varphi(r)$ is satisfied to the TVD constraint then the scheme may be referred as a two-step TVD scheme ([85]). A symmetric limiter of the following form is employed in calculation of the numerical flux $\widehat{\mathrm{H}}_{\mathrm{j}+1/2}$:

$$\varphi(r) = \begin{cases} r & \text{if} \quad |r| < 1, \\ 1 & \text{otherwise} \end{cases} \tag{5.32}$$

One of the advantages of the two-step TVD scheme given by Eqs. (5.26), (5.28) is that it does not use the full set of eigenvalues of the Jacobian matrix. However, as it is seen form Eq. (5.27) an appropriate flux splitting is required which is chosen to be a local Lax-Friedrichs splitting. Accordingly, α_{j} in Eq. (5.27) stands for a local value of the largest eigenvalue of the Jacobian matrix $\partial \mathrm{F}/\partial \mathrm{U}$. Note that from Eq. (5.23) it can be seen that the eigenvalues λ_k^i depend on the line l_k orientation and are given by

$$\lambda_k^1 = 2(u_k^S + u_k^L), \quad \lambda_k^2 = u_k^S + u_k^L, \quad \lambda_k^3 = u_k^S + u_k^L \tag{5.33}$$

The numerical capabilities of the adopted two-step TVD scheme to simulate the SS field is further tested for the nonlinear case given by randomly forced Burgers equation which is described in the following Section.

CHAPTER VI

APPLICATION OF TLS TO TURBULENT FLOWS

6.1 Forced Burgers Turbulence

The purpose of the present section is to study the SS equation in one dimensional domain without introducing any modeling assumptions. The randomly forced Burgers equation which is one dimensional analog of the pressureless Navier-Stokes equation is considered as an example. The LS random force $f^L(x,t)$ acting on the low wave numbers produces stationary turbulent state of the Burgers turbulence. Typical turbulent velocity profile is characterized by the presence of randomly located shocks and pre-shocks which define the SS structures. Thus, a solution of the SS equation is expected to reproduce the shock induced small-scale pattern accurately in order to provide the correct coupling effect on the LS motion.

Applying the decomposition procedure to the Burgers equation

$$\frac{\partial u}{\partial t} + \frac{1}{2}\frac{\partial uu}{\partial x} = \nu\frac{\partial^2 u}{\partial x^2} + f^L, \tag{6.1}$$

gives the following LS and the SS equations:

$$\frac{\partial u^L}{\partial t} + \frac{1}{2}\frac{\partial}{\partial x}\Big[(u^L+u^S)(u^L+u^S)\Big]^L = \nu\frac{\partial^2 u^L}{\partial x^2} + f^L, \tag{6.2}$$

$$\frac{\partial u^S}{\partial t} + \frac{1}{2}\frac{\partial}{\partial x}\Big[(u^L+u^S)(u^L+u^S)\Big]^S = \nu\frac{\partial^2 u^S}{\partial x^2} \tag{6.3}$$

In the present section, a numerical solution of the SS Burgers equation is studied first on the unit periodic domain discretized with $N_S = 16384$ points. The SS velocity field is reconstructed based on zero initial state $u^S(x, t^L_m; t^S) = 0$ and the fixed LS velocity profile $u^L(x, t^L_m)$ according to the procedure outlined at the end of Section 4.2. A two-step, component-wise TVD scheme of [85] is employed for integration as described in the previous Section.

The LS forcing $f^L(x,t)$ is explicitly simulated in spectral space and then transformed back to the physical space. At each time step the forcing represent an independent Gaussian realization with prescribed spectrum of the form $k/k_f exp(-k^2/k_f^2)$, as used by [86]. The mean square value of forcing σ^2 defines a velocity scale U which is chosen together with viscosity ν to have the Reynolds number Re equal to $Re = UL/\nu = \sigma^{1/2}L^{3/2}/\nu \approx 3\cdot 10^6$. The LS velocity field is defined based on the coarse uniform grid with resolution of $N_L = 512$ points. Cubic spline polynomials is used to interpolate the LS field onto the SS grid.

Results of the numerical integration of Eq. (6.3) are presented in Figs. 6.1(a,b). Figure 6.1(a) shows the SS velocity profiles at two early intermediate times, and the final stationary solution $u^S(x, t^L_m)$ in a representative portion of the computational domain. Note, the SS velocity profiles are shifted up-wards to enable comparison. Figure 6.1(b) shows the corresponding evolution of the SS energy spectrum. It is seen that as the solution advances in time t^S, the SS spikes start growing at shock locations and the SS energy is gradually filling up the SS part of the spectrum, finally recovering the SS spectrum with the correct slope.

The time evolution of the total SS energy is shown in Fig. 6.2(a) as the lowest curve ($u^S_0 = 0$). It is seen that the total SS energy tends to the limiting value which corresponds to the exact value of the total SS energy obtained based on the explicit decomposition of the DNS solution. These plots show that the solution of Eq. (6.3) captures the SS pattern in a correct manner. Figure 6.2(a) also shows the total SS energy evolution for the different (in l_2 norm) SS velocity initial conditions. The SS part of the random noise with different amplitudes is used to initialize the SS velocity field. Four different cases of the random initial conditions are considered, with the initial SS energy equal to 0.21%, 21%, 190% and 530% of the energy of the exact SS solution, respectively. This figure shows that the SS energy tends to the limiting value, recovering the same SS velocity profile regardless the initial conditions, suggesting that the SS solution of Eq. (6.3) is insensitive to the choice of initial conditions, and is fully defined by the LS velocity.

In order to study the simplified versions of the SS equations obtained by neglecting nonlinear interaction terms, Eq. (6.3) can be written by expanding the product term on the left hand side as:

$$\frac{\partial u^S}{\partial t} + \frac{1}{2}(L^S + M^S + S^S) = \nu \frac{\partial^2 u^S}{\partial x^2}, \tag{6.4}$$

where the SS non-linear interaction terms are defined as follows:

$$L^S = \frac{\partial}{\partial x}\Big[u^L u^L\Big]^S, \quad S^S = \frac{\partial}{\partial x}\Big[u^S u^S\Big]^S, \quad M^S = 2\frac{\partial}{\partial x}\Big[u^L u^S\Big]^S, \tag{6.5}$$

Equation (6.4) can be simplified by neglecting the interaction terms S^S and/or M^S, while retaining the energy suppling term L^S. Note that in LES literature L^S is derivative of the Leonard stress $\Big[u^L u^L\Big]^S$. If the spectral cutoff filter is used to separate the scales, the Leonard stress has an identical zero LS part and is associated with aliasing errors that can be removed easily at the numerical stage ([6]). In case of other types of filtering, which do not have a property of being projectors (i.e., $\Big[u^L u^L\Big]^S = u^L u^L - \Big[u^L u^L\Big]^L \neq 0$, for the LS modes), the Leonard stress is not zero (albeit small). However, the most of the inter-scale energy exchange due to the Leonard stress is residing in the SS modes, which clearly can not be parameterized by the LS velocity, as assumed in constructing of the SGS models ($\tau_{ij} = \tau_{ij}(\bar{u}_i)$), highlighting an ambiguity in the traditional LES formulation.

It is instructive to compare a solution of the full SS equation with solutions of the

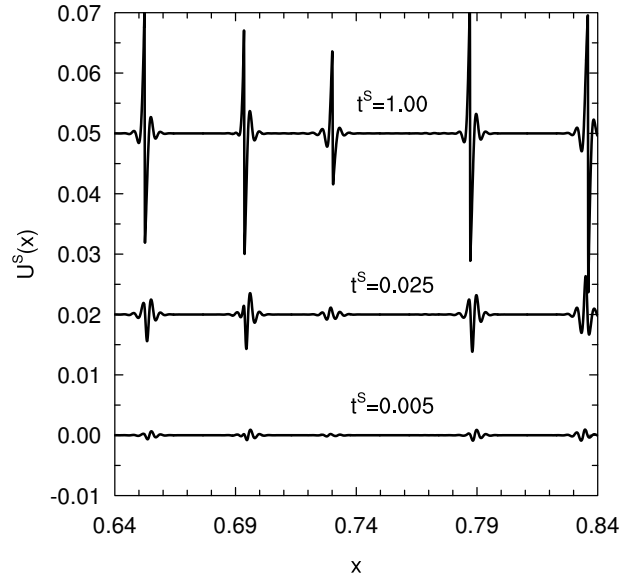

(a)

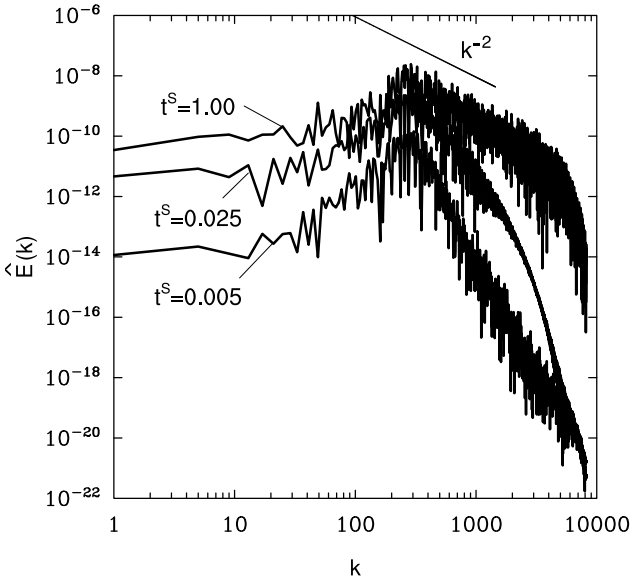

(b)

Figure 6.1: Time evolution of the SS velocity at $t^S = 0.005$, 0.025, 1.00: (a) SS velocity profiles, two upper curves are shifted upwards to ease comparison; (b) The SS energy spectra. Straight line shows slope of -2.

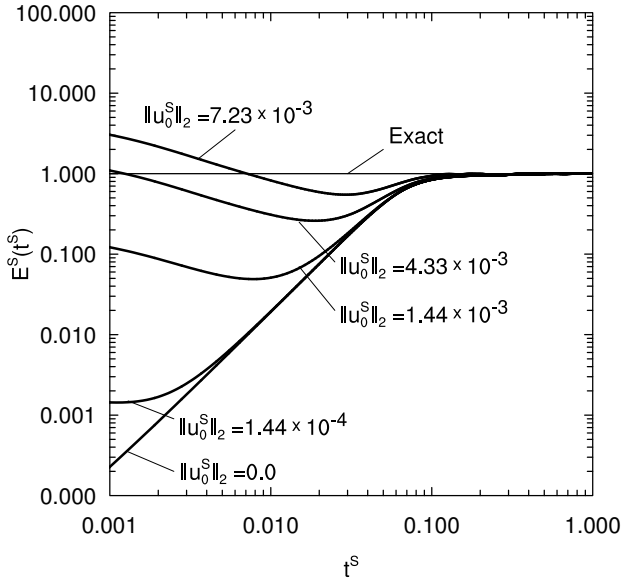

(a)

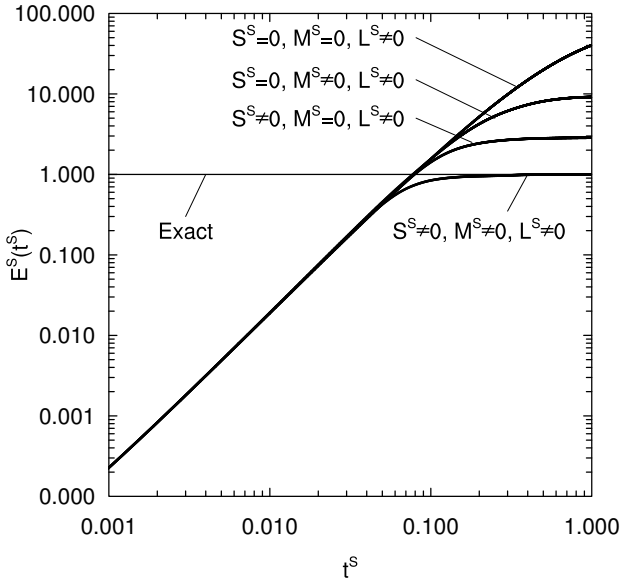

(b)

Figure 6.2: Time evolution of the normalized SS energy for: (a) different values of initial velocity u_0^S; (b) different forms of the simplified SS equation. The horizontal line shows the energy of the exact SS solution.

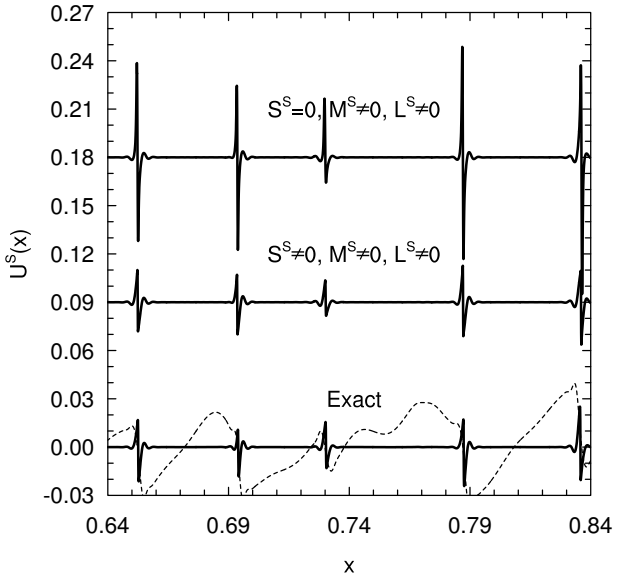

(a)

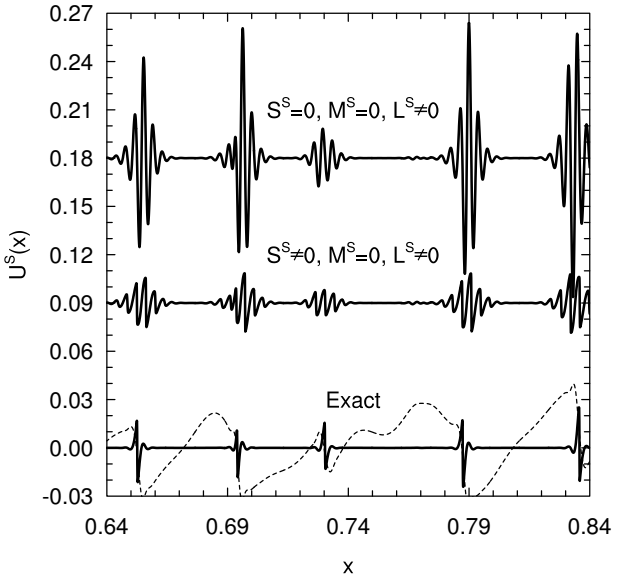

(b)

Figure 6.3: The SS velocity for different forms of the SS equations, from bottom to top: (a) exact SS velocity; Eq. (6.4); Eq. (6.7); (b) exact SS velocity; Eq. (6.8); Eq. (6.6). Two upper SS profiles are shifted upwards to enable comparison. Dashed line shows the LS velocity.

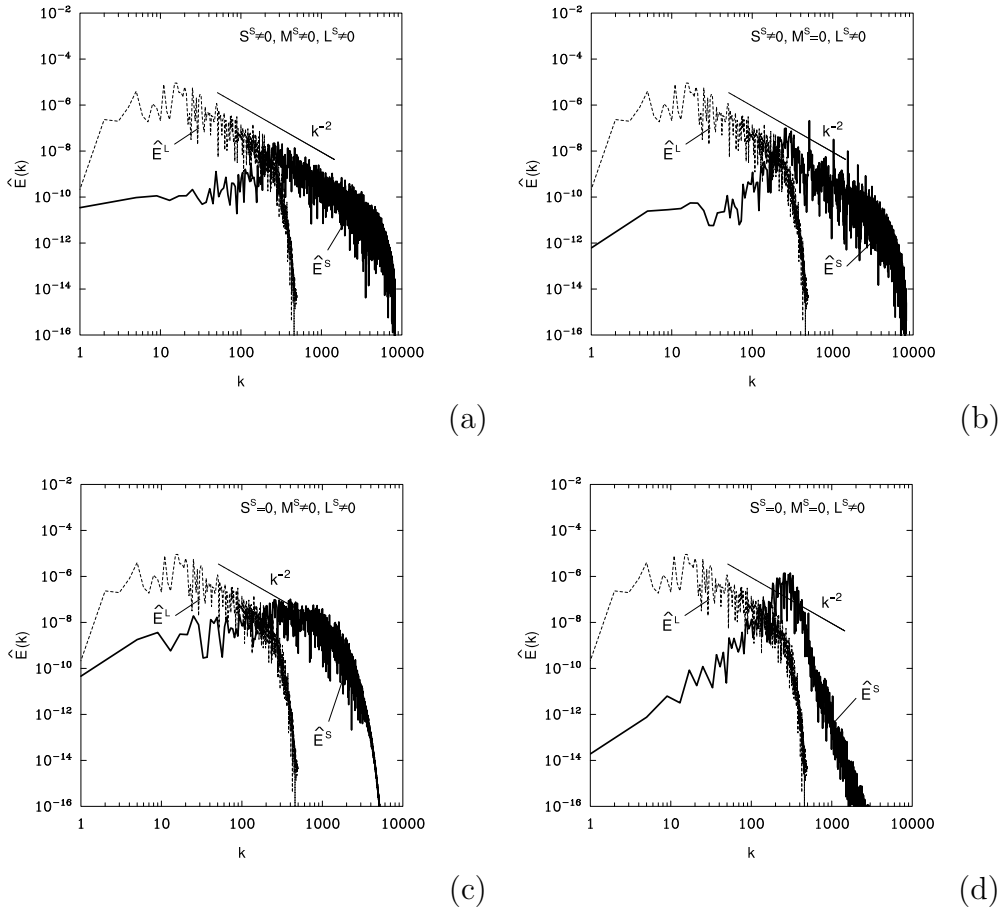

Figure 6.4: The LS (light dashed line) and the SS (solid line) energy spectra for: (a) Eq. (6.4); (b) Eq. (6.8); (c) Eq. (6.7); (d) Eq. (6.6).

following simplified SS equations:

$$\frac{\partial u^S}{\partial t^S} = -\frac{1}{2}L^S + \nu\frac{\partial^2 u^S}{\partial x^2}, \tag{6.6}$$

$$\frac{\partial u^S}{\partial t^S} = -\frac{1}{2}(L^S + M^S) + \nu\frac{\partial^2 u^S}{\partial x^2}, \tag{6.7}$$

$$\frac{\partial u^S}{\partial t^S} = -\frac{1}{2}(L^S + S^S) + \nu\frac{\partial^2 u^S}{\partial x^2} \tag{6.8}$$

These types of the simplified SS equations have been used previously in literature to model the SS dynamics in the context of 2D and 3D incompressible turbulence. For example, the stationary form of Eq. (6.6) was used by [47, 48] to derive the AIM for 2D turbulent flows. Equation (6.7), where the mutual SS-SS interaction term S^S is neglected, was proposed by [42, 43] as the RDT model to study 2D and 3D isotropic turbulent flows.

The snapshots of the SS velocity for all four cases (Eqs. (6.4), (6.6)-(6.8)) are

shown in Figs. 6.3 (a,b) together with the exact SS velocity explicitly computed from the full DNS solution. It is seen that the solution of Eq. (6.4) provides the best agreement with the exact SS solution. This is also evident from the time evolution of the total SS energy shown in Fig. 6.2(b). The only SS solution which exhibits an asymptotic convergence to the exact SS solution corresponds to the case when all interaction terms are retained (Eq. 6.4). All three approximate forms of the SS equation (Eqs. (6.6)-(6.8)) are characterized by slow growth of the SS energy. The growth is largest for the case of Eq. (6.6) when both the interaction terms M^S and S^S are zero. This is further supported by the instantaneous energy spectra plots shown in Figs. 6.4(a-d) that are computed at the time when the solution of the full SS equation reaches a stationary state.

This behavior can be understood by considering the role of interaction terms L^S, M^S and S^S in the SS energy equation. The LS and the SS energy interaction terms can be defined in spectral space as:

$$\widehat{E}^L_L = -\frac{1}{2}(\widehat{L}^L\widehat{u}^{L*} + \widehat{L}^{L*}\widehat{u}^L), \quad \widehat{E}^L_M = -\frac{1}{2}(\widehat{M}^L\widehat{u}^{L*} + \widehat{M}^{L*}\widehat{u}^L), \tag{6.9}$$

$$\widehat{E}^L_S = -\frac{1}{2}(\widehat{S}^L\widehat{u}^{L*} + \widehat{S}^{L*}\widehat{u}^L), \quad \widehat{E}^S_L = -\frac{1}{2}(\widehat{L}^S\widehat{u}^{S*} + \widehat{L}^{S*}\widehat{u}^S), \tag{6.10}$$

$$\widehat{E}^S_M = -\frac{1}{2}(\widehat{M}^S\widehat{u}^{S*} + \widehat{M}^{S*}\widehat{u}^S), \quad \widehat{E}^S_S = -\frac{1}{2}(\widehat{S}^S\widehat{u}^{S*} + \widehat{S}^{S*}\widehat{u}^S), \tag{6.11}$$

where $\widehat{u}^L$ and $\widehat{u}^S$ are the Fourier transform of the LS and the SS velocities respectively, and the star symbol denotes the complex conjugate. These energy interaction terms represent the source terms in the LS and the SS energy evolution equations. Denoting the LS and the SS spectral energy as $e^L(k,t) = \widehat{u}^L\widehat{u}^{L*}$ and $e^S(k,t) = \widehat{u}^S\widehat{u}^{S*}$, and the spectral energy term due to the LS forcing by $\widehat{F}^L(k,t)$, the LS and SS spectral energy equations can be written as:

$$\frac{\partial e^L}{\partial t} = \widehat{E}^L_L + \widehat{E}^L_M + \widehat{E}^L_S - 2\nu k^2 e^L + \widehat{F}^L(k,t), \tag{6.12}$$

$$\frac{\partial e^S}{\partial t} = \widehat{E}^S_L + \widehat{E}^S_M + \widehat{E}^S_S - 2\nu k^2 e^S. \tag{6.13}$$

A sign of the energy interaction terms determines a direction in which energy is transferred between scales due to an action of the corresponding LS or SS nonlinear interaction term.

The time averaged spectra of these energy interaction terms are presented in Figs. 6.5(a-c). The spectra are computed by averaging of instantaneous spectra after the stationary turbulent state is reached. It is seen that both M^S and S^S redistribute energy in favor of the smaller scales. On the other hand, the derivative of the Leonard stress L^S supplies energy to the small scales at wave-numbers adjacent to the scale separation wavenumber k^L, as shown in Fig. 6.5(a). The spectral support of the Leonard stress L^S is approximately bounded by $2k^L$ and does not overlap the dissipation range, since $k^L \sim N^L/2$ is chosen to resolve just the beginning of the inertial range. Therefore, when the energy redistributing mechanism (removal due to

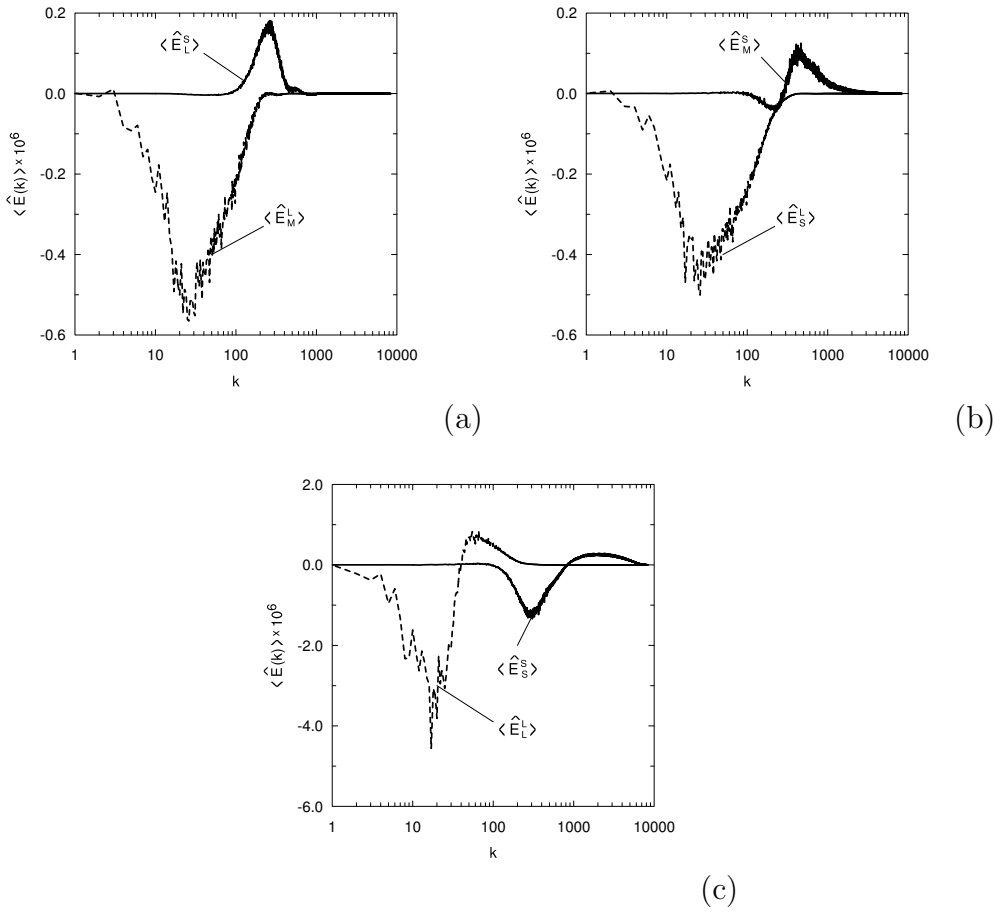

Figure 6.5: Time averaged spectra of the energy interaction terms: (a) $\langle \widehat{E}_M^L \rangle$ (dashed line) due to M^L and $\langle \widehat{E}_L^S \rangle$ (solid line) due to L^S; (b) $\langle \widehat{E}_S^L \rangle$ (dashed line) due to S^L and $\langle \widehat{E}_M^S \rangle$ (solid line) due to M^S; (c) $\langle \widehat{E}_L^L \rangle$ (dashed line) due to L^L and $\langle \widehat{E}_S^S \rangle$ (solid line) due to S^S. The spectrum $\langle \widehat{E}_S^S \rangle$ is multiplied by a factor of 10 to enable comparison.

the interaction terms M^S, S^S or dissipation due to the viscous term) is absent, the energy of the small scales grows steadily, as is evident from Figs. 6.4(b,d). The SS interaction term S^S plays an important role in stabilizing the SS solution in spite of the fact that S^S is much smaller in spectral magnitude compared with M^S and L^S. The counterpart of this term in the SS energy equation, i.e., $\widehat{E}_S^S$, is only an order of magnitude smaller than $\widehat{E}_M^S$ or $\widehat{E}_L^S$, as evident from Figs. 6.5(a-c). Figure 6.5(c) shows that S^S redistribute energy similar to its LS counterpart L^L by removing the SS energy from the near-cutoff region and cascading it down to the smaller scales. Neglecting S^S, as it would be suggested in context of the RDT model, leads to an excessive accumulation of energy in the SS which could have an adverse effect on the LS velocity.

6.2 Forced Isotropic Turbulence

The forced isotropic turbulence presents the important ideal case to evaluate approximate turbulence modeling approaches. TLS of the forced isotropic turbulent flow has been conducted to study the ability of the model to sustain the stationary turbulent state at the LS and SS levels, and to provide an adequate energy coupling between the LS and SS.

First of all the stand-alone SS Eq. (4.26) has been integrated numerically to study the model capability to reconstruct the SS velocity on lines. Similar to the Burgers case the SS velocity evolves from zero initial state, and requires the LS velocity and its derivatives as the only input parameters. The LS velocity field is computed on the uniform 32^3 grid and obtained from 256^3 DNS data set according to the averaging procedure given by Eq. (4.24). Typical results are exhibited in Figs. 6.6(a,b) where evolution of the SS spectral energy and the SS velocity profiles are shown for three consecutive instants of time t^S. Due to nonlinear interactions between the LS and the SS fields, energy starts cascading down to the SS part of spectrum till it is dissipated at the viscous dissipation range, eventually creating the SS velocity field. It is seen that at the final stage the SS energy spectrum matches the SS part of DNS spectrum quite well. The evolution time needed to reconstruct the SS velocity field is determined by matching the LS and the SS energies at the minimal scale resolvable by the LS grid. Isotropic velocity field and parallel line arrangements allow us to consider an average energy along lines which is exhibited in Figure 6.7. Here, the averaged (along l_1 lines) SS spectrum is shown with the DNS and exact SS energy spectra. The exact SS field is computed explicitly from the DNS velocity field. It is seen that overall comparison of the SS spectra is quite satisfactory. However, the averaged SS spectrum exhibits small deviation the exact SS spectrum by redistributing more SS energy in favor of smaller scales, closer to dissipation range. This is probably manifestation of the adopted assumption given by Eq. (4.25).

The uniform 32^3 LS grid is used to discretize 2π cubic domain. Two cases for the Taylor scale Reynolds number $Re_\lambda \approx 65$ and 114 are considered. All TLS lines have uniform resolution of 128 and 256 grid points for the low and high Reynolds number cases, respectively. A matching DNS for the low Reynolds number case has been also performed by applying the same forcing on 128^3 grid for comparison purposes. For the chosen LS grid resolution, TLS code requires about one single-processor hour on IBM SP4 to reach the stationary turbulent state, while it takes almost 17 hours of CPU time for DNS. Both codes were run in serial mode with the exception of the SS computation for the TLS model, which is done in parallel using 48 processors.

Both simulations start with zero initial conditions and periodic in space. The force is concentrated around small wave numbers and gradually drives the flow to the stationary state. Here, the forcing scheme of [87] is adopted. The random force of the form $\hat{f}_i(\mathbf{k},t) = (\delta_{ij} - k_i k_j/k^2) w_j(\mathbf{k},t) \times [\Theta(\mathbf{k}) - \Theta(\mathbf{k}-\mathbf{k}_F)]$ is used, where w_j is Uhlenbeck-Ornstein stochastic process, δ_{ij} is the Kronecker delta and Θ is the Heaviside function. The process is of diffusion type, has zero mean and correlated over time with a chosen time scale τ. For a given grid resolution, three parameters define the intensity of forcing: the amplitude σ, the time-scale τ and the maximum

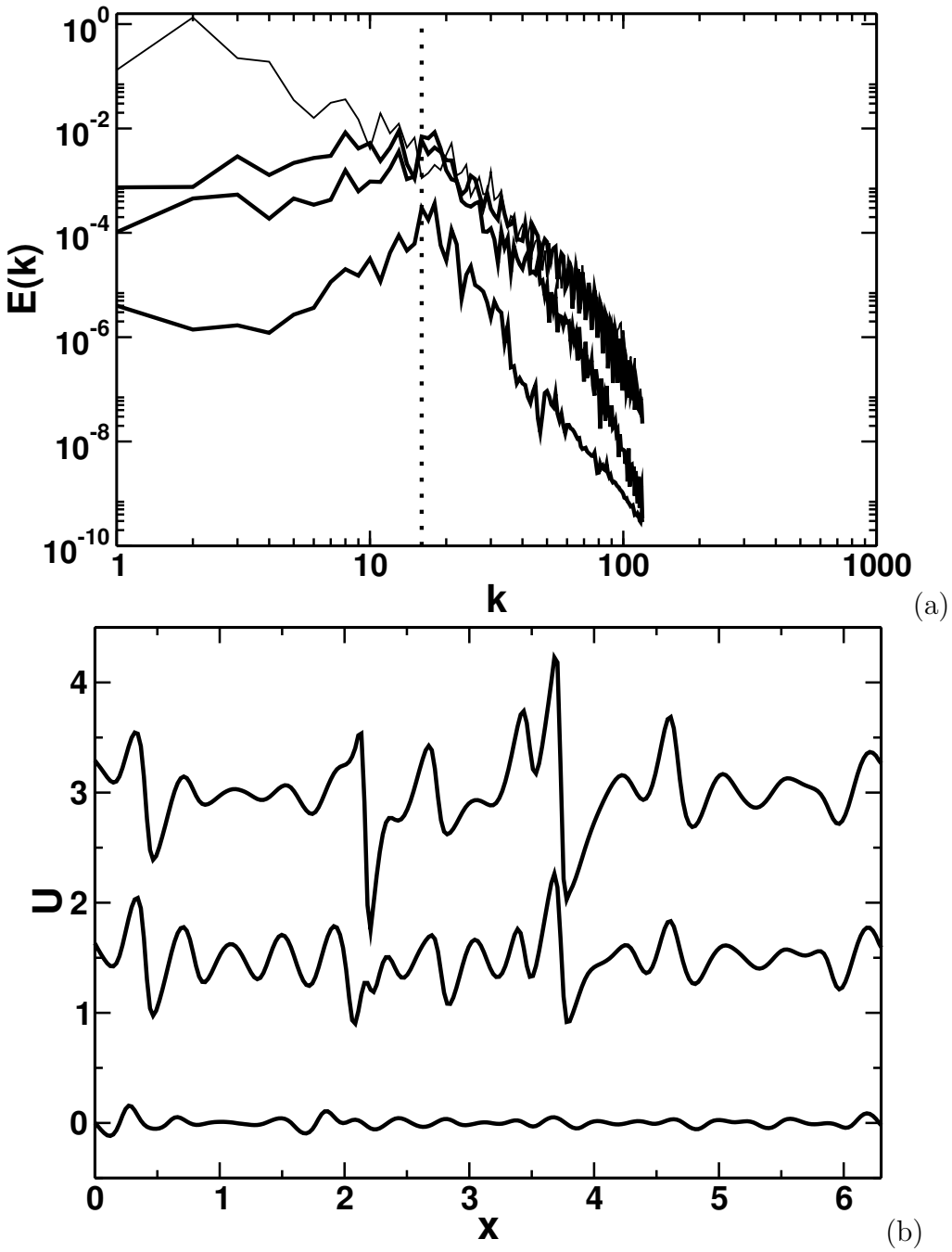

Figure 6.6: (a) Instantaneous SS energy spectra (solid line) compared with the DNS spectrum (thin solid line); (b) corresponding reconstructed SS velocity profiles on a line for three consecutive time instants. LS grid resolution is shown by dotted vertical line.

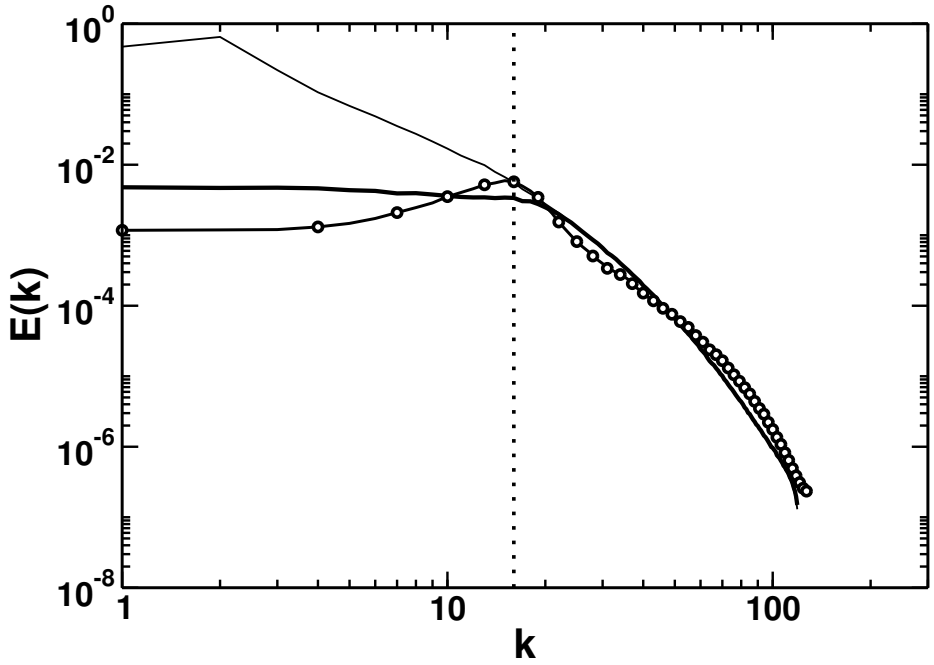

Figure 6.7: Average line energy spectra: DNS (thin solid line), exact SS (solid line), reconstructed SS (circles). The LS grid resolution level is shown by dotted vertical line.

wave number of the forced modes k_F. Here, we have taken the value of k_F, normalized by the lowest wavenumber, to be equal to $\sqrt{2}$. With the time scale $\tau = 0.95$ and 0.8, and the amplitude $\sigma = 0.04$ and 0.007, the forcing scheme produces the isotropic turbulent fields with $Re_\lambda \approx 65$ and 114, respectively. However, as it was pointed out by [88] who used this method to study LES subgrid models, the same forcing cannot be guaranteed for different grid resolutions even with the same forcing parameters. As a result, the DNS case only approximately achieves $Re_\lambda \approx 60$ which is less then $Re_\lambda \approx 65$ of the TLS case. Nevertheless, for comparison purposes it does not appear to be a serious issue.

The LS turbulent kinetic energy and the dissipation rate are shown in Figs. 6.8(a,b) as functions of time. It is seen that the stationary state is reached at time $T \approx 8$ for both cases. The case with higher Reynolds number is characterized by more intense fluctuations of the kinetic energy and the dissipation rate in time. Time evolution of the RMS of the LS velocity components $\langle u_i^L \rangle_{rms}$ along with the averaged rms-velocity scale are shown in Fig. 6.9(a). These figures suggest that TLS is able to sustain the turbulent stationary state well and the SS coupling does not destroy the isotropy of the LS flow.

Figure 6.9(b) shows the TLS and DNS compensated energy spectra versus the wavenumber normalized by the Kolmogorov dissipation scale η, after a stationary state is reached. Both TLS energy spectra approximates the DNS spectrum quite satisfactorily, although they results in a small build-up of energy near the LS cut-off wavenumber. It can be related to the fact that the SS velocity field might be

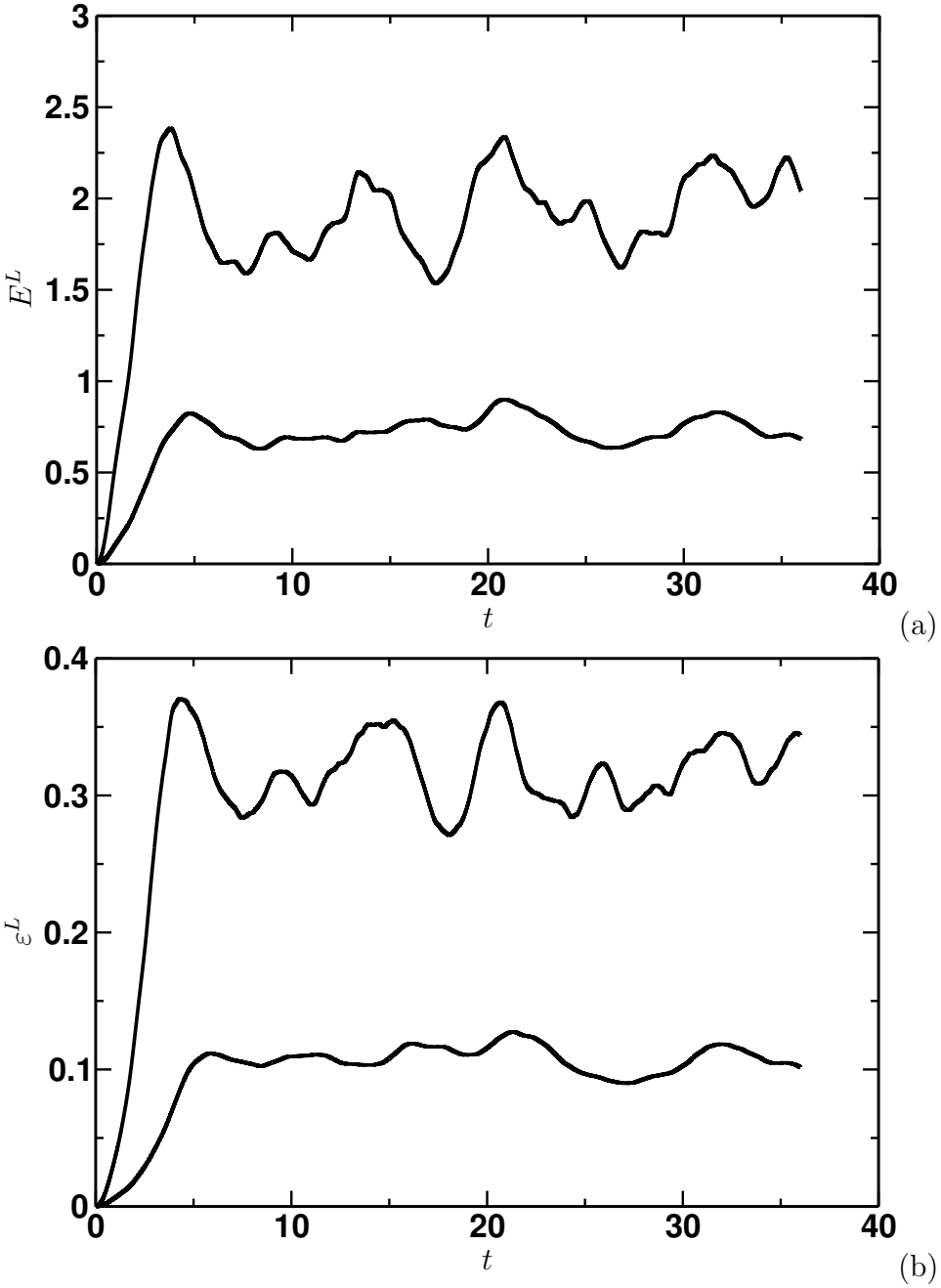

Figure 6.8: (a) Time evolution of the turbulent kinetic energy $E^L(t)$ of the LS for $Re_\lambda = 65$ (lower line) and 114 (upper line); (b) LS dissipation rate $\varepsilon^L(t)$ for $Re_\lambda = 65$ and 114.

underestimated on some lines, thus providing diminished dissipative effects on scales at the LS grid cut-off level. In TLS, the SS fields are evolving from zero to the point when the LS and SS spectra are matched at the minimum resolvable LS scales. Generally, the SS evolution time, which is required to match LS and SS spectra, is different for various lines. Matching spectral condition is important to simulate correct coupling between the LS and the SS velocity fields. If the SS field grows too much it would produce unphysical effects on the LS field by backscattering extra energy at the LS grid level, eventually contaminating the LS field. On the other hand, if the SS field is underpredicted in spectral magnitude at the LS grid cut-off level, it would not provide enough dissipation to the LS field causing the energy pile-up by blocking forward cascade.

The SS evolution time is also a function the local Reynolds number and the LS grid resolution. The more LS are resolved the less time is needed to reconstruct the SS field and vice versa. On the other hand, the higher the Reynolds number, the larger is the range of scales that is needed, and longer time is required to fill up the modeled SS part of the spectrum. Further study is needed to address the SS evolution time sensitivity to the LS grid resolution and the Reynolds number.

Snapshots of the LS vorticity magnitude isosurfaces at the level of $\omega^L = 6.5$ and $\omega^L = 10.0$ are shown in Figs. 6.10(a) and 6.11(a) for $Re_\lambda \approx 65$ and 114, respectively. The higher Reynolds number case is characterized by more intense LS vorticity level and the presence of more LS vortical structures. In spite of the fact that the full SS vorticity is not available in TLS, because the SS derivatives are known along lines only, it can be computed at the LS grid level where orthogonal lines intersect each other. Such a LS "footprint" of the SS vorticity is shown in Figs. 6.10(b) and 6.11(b). Isosurfaces of the resolved SS vorticity magnitude are computed at the level of $[\omega^S]^L = 0.46$ and $[\omega^S]^L = 0.70$ for $Re_\lambda \approx 65$ and 114, respectively. It is seen that the resolved SS vorticity field responds to the LS vorticity in qualitatively correct way, by creating more intensive and more dense SS vortical structures.

6.3 Turbulent Channel Flow

A well-developed turbulent channel flow is simulated to assess a capability of TLS approach to capture essential features of the near-wall turbulence.

A flow domain of $2\pi \times 2 \times \pi$ is discretized with the LS orthogonal grid of $32 \times 40 \times 32$ cells, with no stretching in the streamwise and the spanwise directions, and only a nominal stretching in the wall-normal direction, from the wall to the centerline of the channel. The width of the first near-wall cell is chosen to be about $\Delta^L x_3^+ \approx 19$ in wall units so that the inner layer is not well resolved. The important Reynolds number $Re_\tau = u_\tau h/\nu$ is based on the friction velocity u_τ and the channel half-width h, and is typically 20-30 times smaller then the centerline velocity based Reynolds number $Re = U_0 h/\nu$. For the chosen Reynolds number Re_τ=590, this near-wall resolution is very coarse even for LES. The corresponding DNS resolution would require $384 \times 257 \times 384$ grid ([89]). As a result of the chosen LS grid, the near-wall turbulent field is not expected to be captured completely by the LS simulation and the

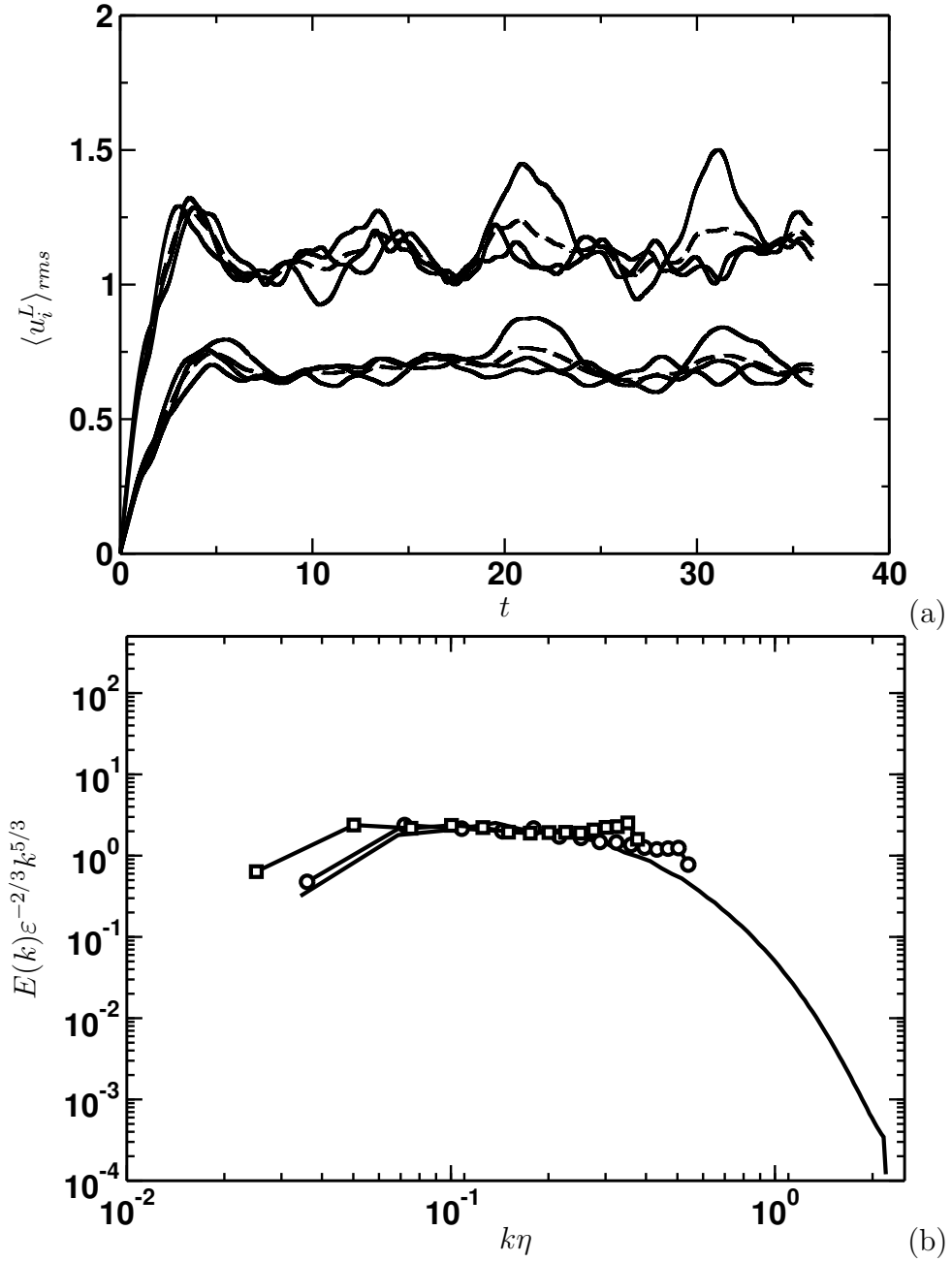

Figure 6.9: (a) Time evolution of the LS rms velocities $\langle u_i^L \rangle_{rms}(t)$ (solid line) and the LS rms-velocity scale v_{rms} (dashed line) for $Re_\lambda = 65$ (lower lines) and 114 (upper lines); (b) Compensated energy spectrum $E(k)\varepsilon^{-2/3}k^{5/3}$ of TLS for $Re_\lambda = 65$ (circles), 114 (squares) and DNS (solid line).

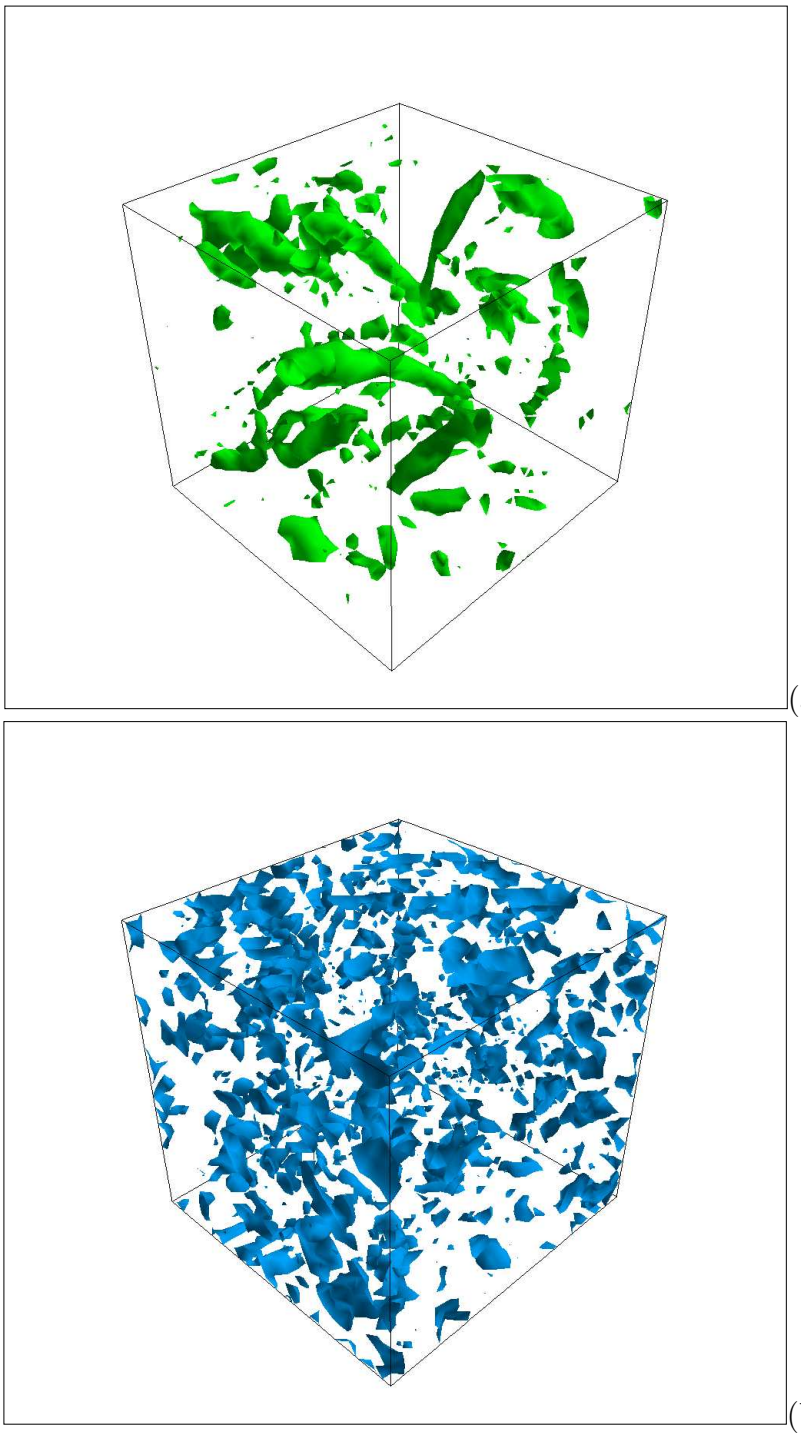

Figure 6.10: Isosurfaces of vorticity magnitude for $Re_\lambda = 65$: (a) LS vorticity; (b) SS vorticity.

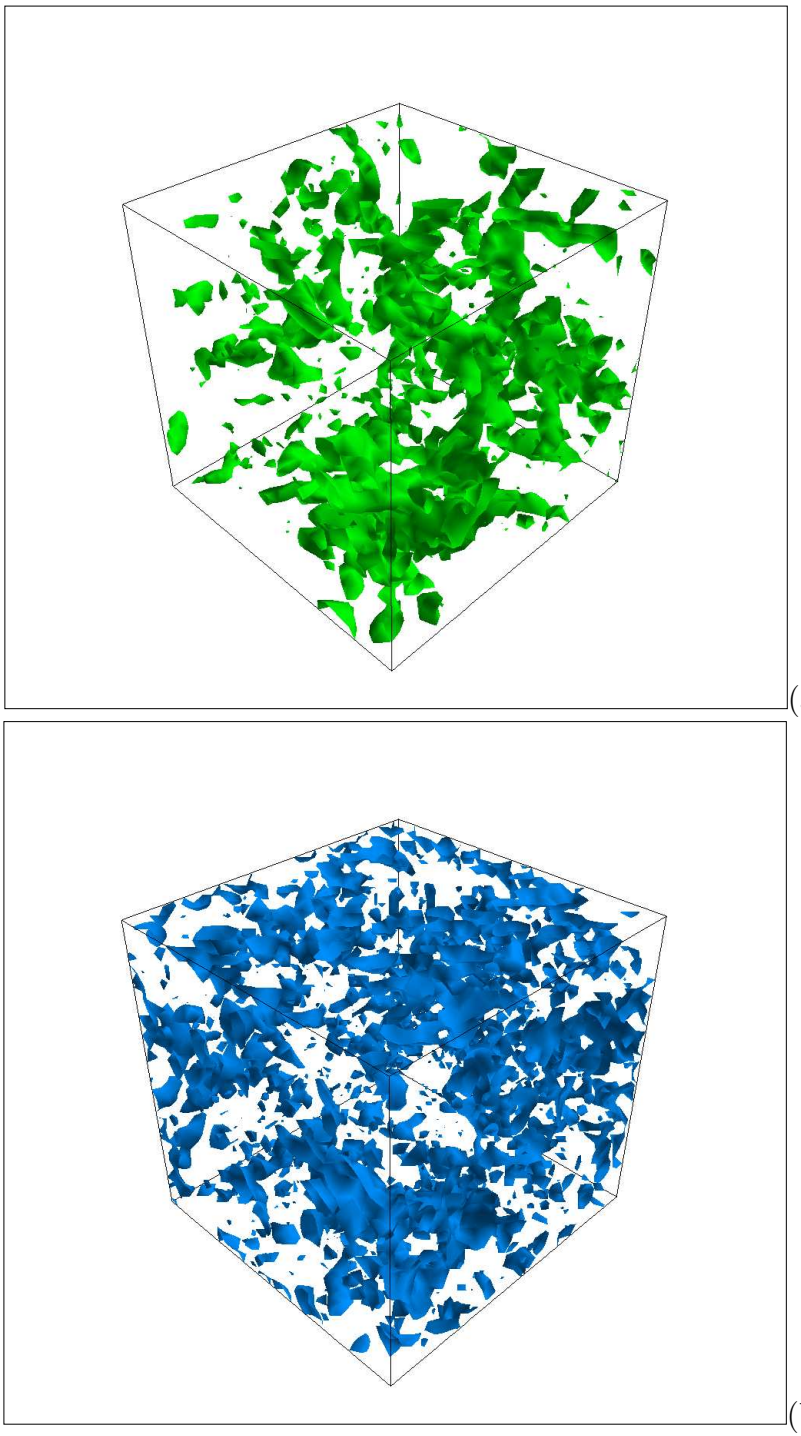

Figure 6.11: Isosurfaces of vorticity magnitude for $Re_\lambda = 114$: (a) LS vorticity; (b) SS vorticity.

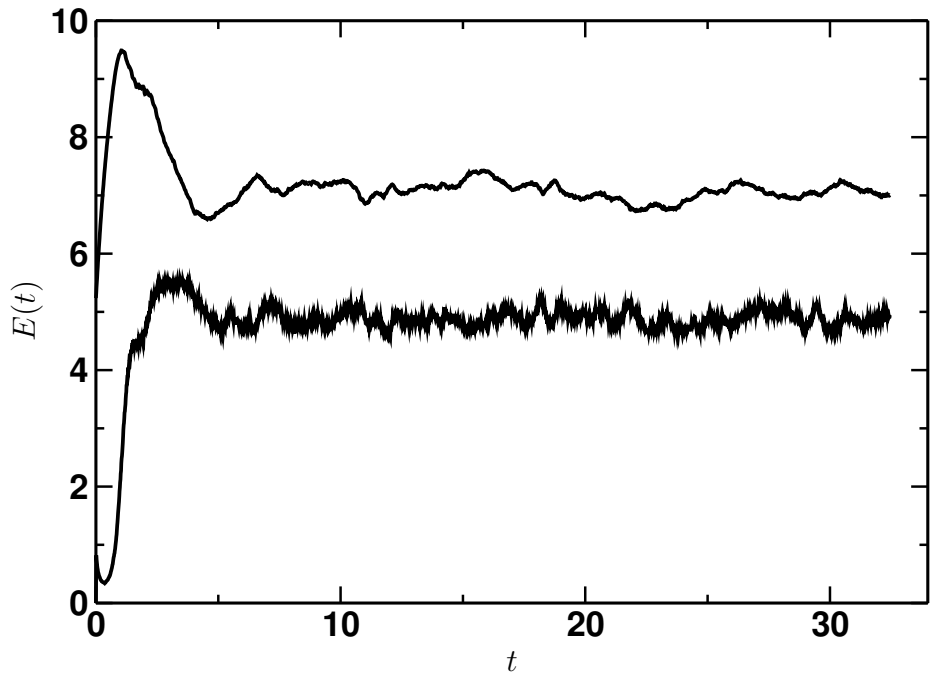

Figure 6.12: Time evolution of the turbulent kinetic energy for the LS $E^L(t)$ (upper line) and the SS $E^S(t)$ (lower line). $E^S(t)$ is multiplied by 150 to enable comparison.

burden of the accurate approximation of the total turbulent field is on the SS model. A uniform SS grid with 8 grid points per LS cell is employed for lines in the periodic directions. The wall normal lines use a non-uniform grid with variable number of grid points per LS cell, ranging from 12 near the wall to 4 in the centerline region of the channel, which gives the maximal near-wall resolution about $\Delta^S x_3^+ \approx 1.58$. So most near-wall dynamics is expected to be resolved on those lines. Statistical data are accumulated after the reaching turbulent stationary state.

The time evolution of the LS and SS turbulent kinetic energies is shown in Fig. 6.12. After initial transient period both the LS and the SS fields reach the stationary state at time $T \approx 6$. The SS turbulent kinetic energy E^S is computed by averaging of $u_i^S u_i^S/2$ over all SS lines. The values of the SS turbulent kinetic energy is multiplied by 150 to make visual comparison possible. The SS turbulent kinetic energy follows the pattern similar to the LS energy, however it is characterized by more intermittent, high-frequency fluctuations related to high-gradient, non-Gaussian SS events captured by the SS field.

Some limited qualitative information on the SS model behavior can be drawn from analysis of the SS velocity field on lines. The streamwise LS and SS velocity components along three different streamwise and spanwise lines are given in Figs. 6.13, 6.15. The lines are chosen in the following manner: near the wall ($x_3^+ = 9.4$), close to the centerline ($x_3^+ = 373$), and in the intermediate (buffer) region between the wall and the centerline ($x_3^+ = 138$). Note that profiles for the near-center line and the intermediate line SS velocity are shifted up-wards from zero to enable comparison.

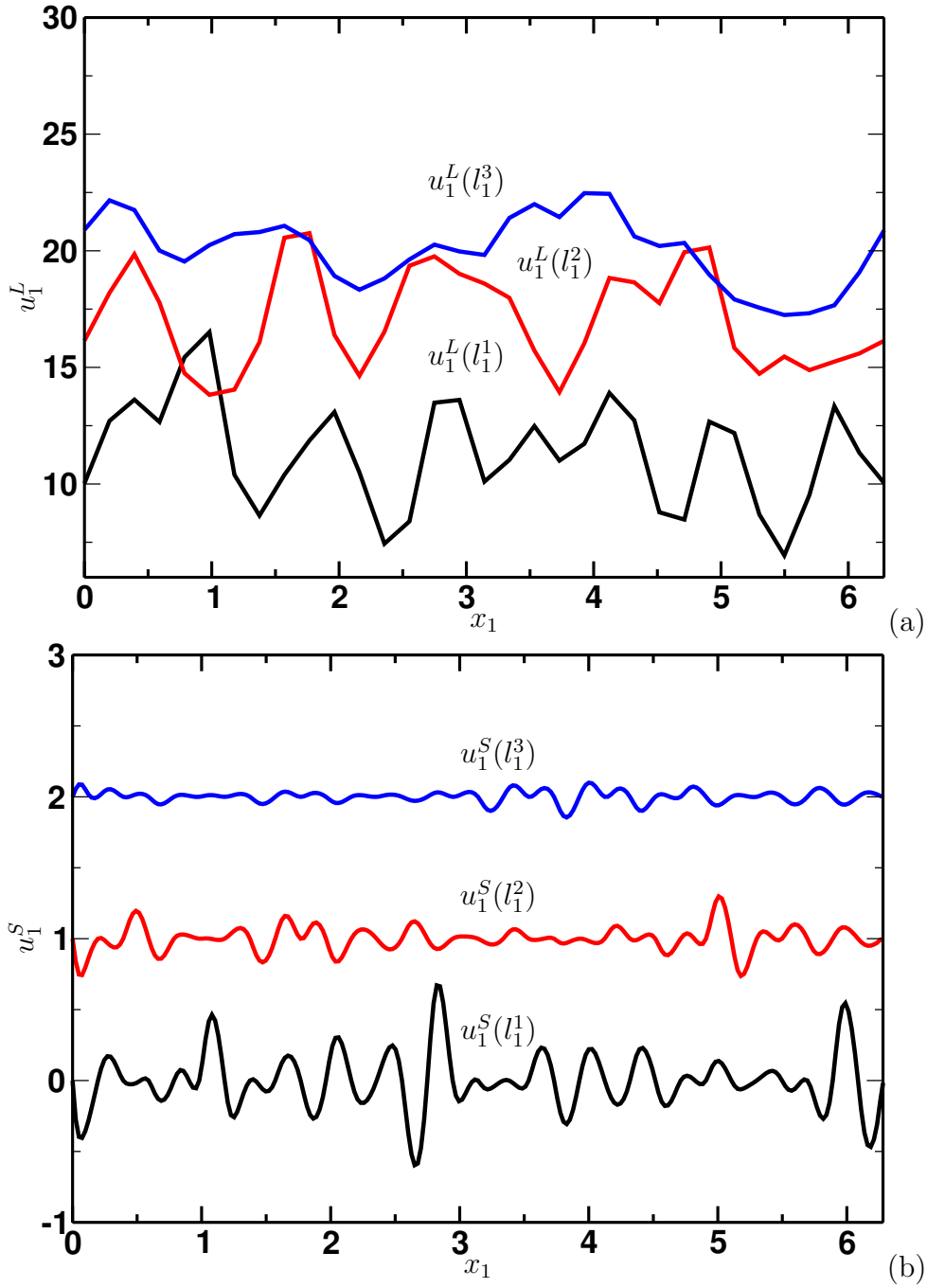

Figure 6.13: Typical instantaneous velocity profiles along streamwise lines at $x_3^+ = 9.4$, $x_3^+ = 138$, $x_3^+ = 373$: (a) LS streamwise velocity u_1^L; (b) SS streamwise velocity u_1^S. Two upper profiles of the SS velocity are shifted upwards by 1 and 2 respectively.

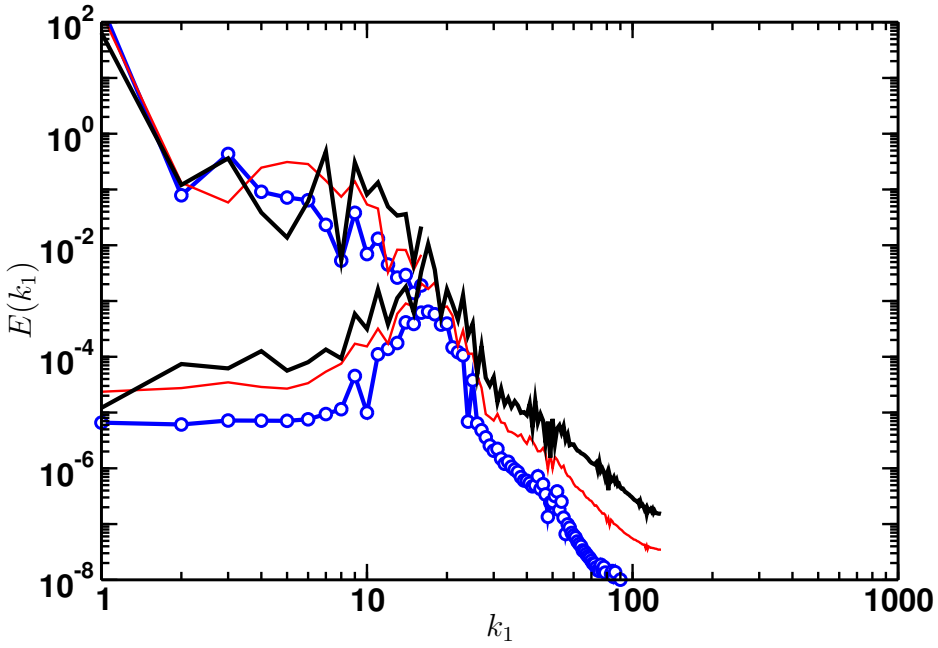

Figure 6.14: LS and SS line energy spectra for streamwise lines located at $x_3^+ = 9.4$ (thick solid line), $x_3^+ = 138$ (thin solid line), $x_3^+ = 373$ (circles).

The corresponding line energy spectra are shown in Figs. 6.14 and 6.16 respectively. These plots show that intensity and the spectral content of the SS velocity field is increasing toward the wall. The SS energy spectra are approximately matched with the corresponding LS energy spectra showing almost the same energy content at the smallest resolved LS level. The instantaneous profiles of the LS and SS streamwise velocities along three wall-normal lines are exhibited in Fig. 6.17. The SS field is characterized by strong fluctuations in the near-wall (buffer) region. These figures indicate that SS model equation (Eq. 4.26) has an ability to reconstruct the correct qualitative behavior of the SS velocity field including the near-wall region.

The SS velocity field features can be also visualized by considering streamwise vorticity. In TLS, the SS velocity can be used to compute derivatives at the LS grid nodes, and therefore, estimate the SS vorticity field. Typical contour lines of the LS and the SS streamwise vorticity in a cross-sectional x_2x_3 plane are shown in Figs. 6.18(a,b). Streamwise vortices are clearly discernible in both LS and SS fields. It is seen that the SS streamwise vortical structures have a tendency of clustering near the most intense LS vortices. This is further illustrated by Figs. 6.19(a,b) where isosurfaces of the LS and the SS streamwise vorticity are shown at the lower channel wall. Despite being reconstructed only at the LS grid level the SS streamwise vorticity demonstrates qualitatively correct near-wall pattern which is populated by counter-rotating streamwise vortices. However, visualization of high vorticity regions sometimes fails to represent vortical structures correctly, especially in regions with a strong mean shear like the near-wall flow region, due to sensitivity to sheet-like structures also. Usually, positive values of the second invariant of the velocity gradient

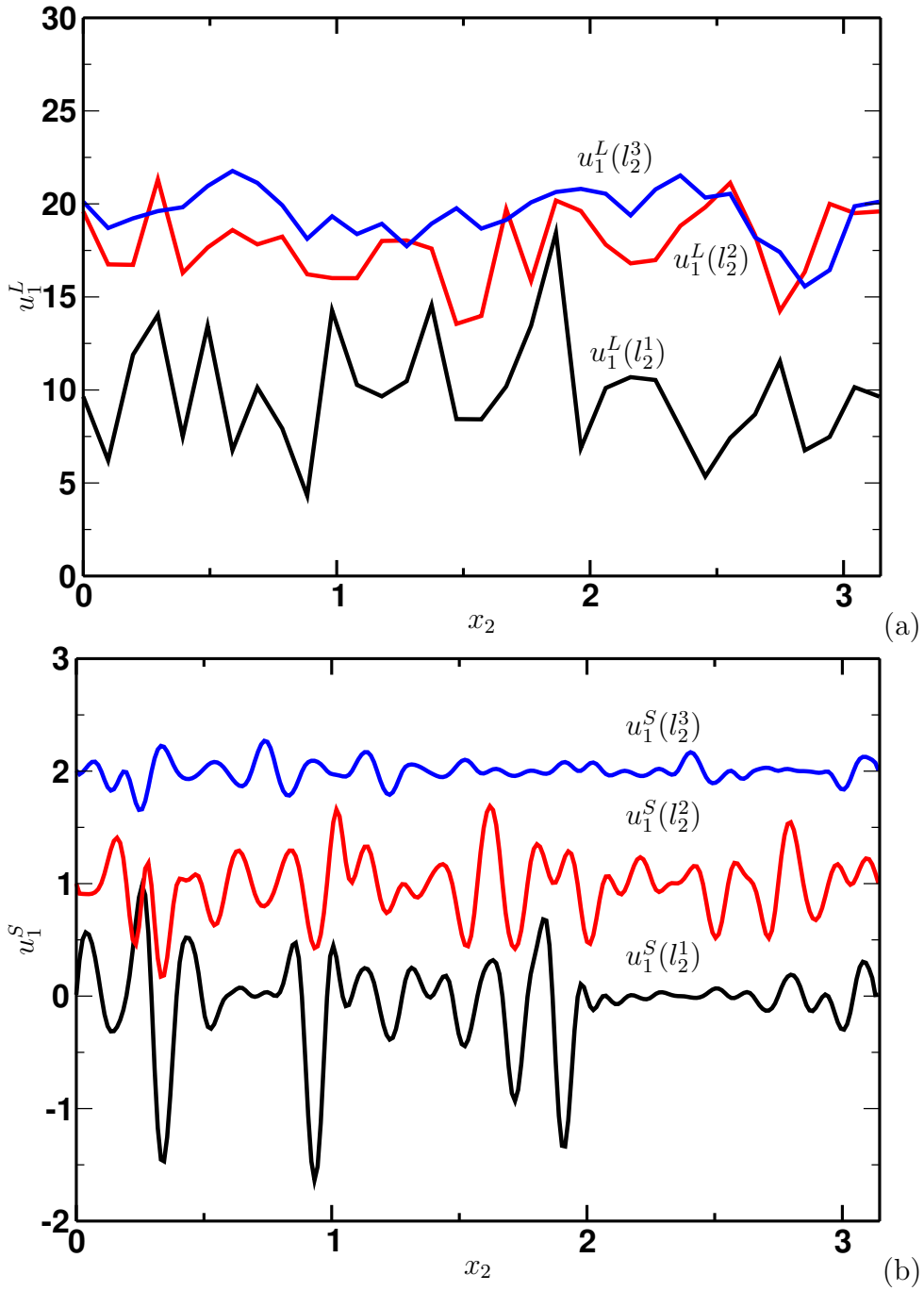

Figure 6.15: Typical instantaneous velocity profiles along spanwise lines at $x_3^+ = 9.4$, $x_3^+ = 138$, $x_3^+ = 373$: (a) LS streamwise velocity u_1^L; (b) SS streamwise velocity u_1^S. Two upper profiles of the SS velocity are shifted upwards by 1 and 2 respectively.

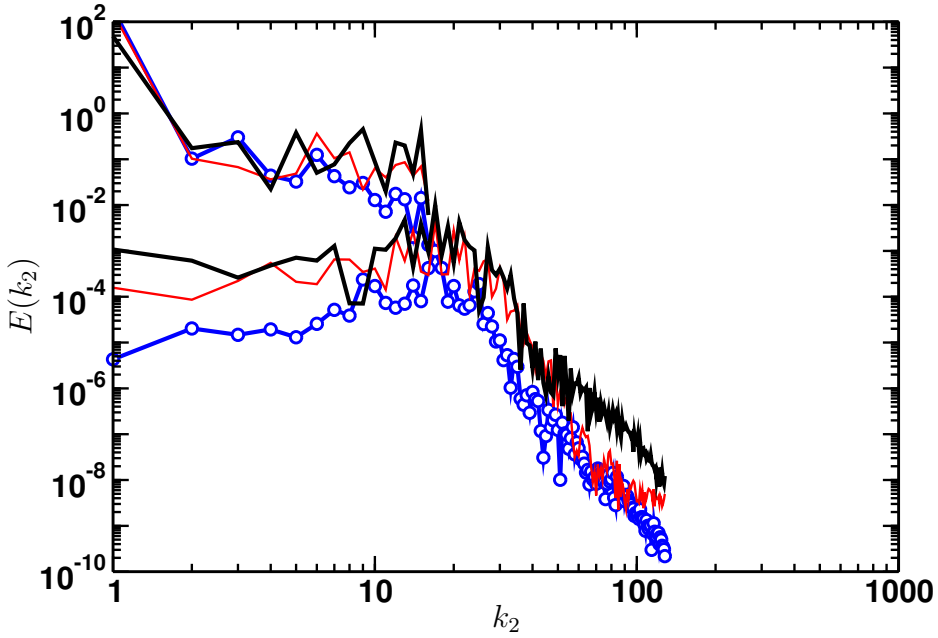

Figure 6.16: LS and SS line energy spectra for spanwise lines located at $x_3^+ = 9.4$ (thick solid line), $x_3^+ = 138$ (thin solid line), $x_3^+ = 373$ (circles).

tensor $Q > 0$ is employed to indicate the regions of intense enstrophy (rotation) and weak shear ([90]). The LS and the SS second invariants of $\partial u_i^L/\partial x_j$ and $\partial u_i^S/\partial x_j$ are:

$$Q^L = \frac{1}{2}(\Omega_{ij}^L \Omega_{ij}^L - S_{ij}^L S_{ij}^L), \quad Q^S = \frac{1}{2}(\Omega_{ij}^S \Omega_{ij}^S - S_{ij}^S S_{ij}^S), \tag{6.14}$$

$$\Omega_{ij}^{L,S} = \frac{1}{2}(\frac{\partial u_i^{L,S}}{\partial x_j} - \frac{\partial u_j^{L,S}}{\partial x_i}), \quad S_{ij}^{L,S} = \frac{1}{2}(\frac{\partial u_i^{L,S}}{\partial x_j} + \frac{\partial u_j^{L,S}}{\partial x_i}),$$

where Ω_{ij}^L, Ω_{ij}^S and S_{ij}^L, S_{ij}^S are the rate-of-rotation and rate-of-strain tensors of the LS and SS fields respectively. Isosurfaces of the positive second invariants Q^L, Q^S are shown in Figs. 6.20(a,b). They demonstrate numerous tube-like structures in the near-wall flow region for both LS and SS fields.

The self-sustaining mechanisms of the near-wall turbulence dynamics have been subject to numerous experimental and numerical studies but still pose significant challenges as theoretically well as computationally ([58]). However, some important structural features such as low-speed streaks, quasi-streamwise vortices have received much attention in early experimental works by [57], [91]. Later [92] identified the bursting process, where the low-momentum fluid from low-speed streaks that form near the wall is ejected upwards, as a principal mechanism for production of the turbulent kinetic energy. Therefore, an ability to reproduce correct qualitative physical behavior in the near-wall region would be an important attribute to validate the proposed TLS approach.

To study the LS near-wall dynamics the joint PDF of streamwise and wall normal LS velocity fluctuations was analyzed at three different locations from the wall, $x_3^+ =$

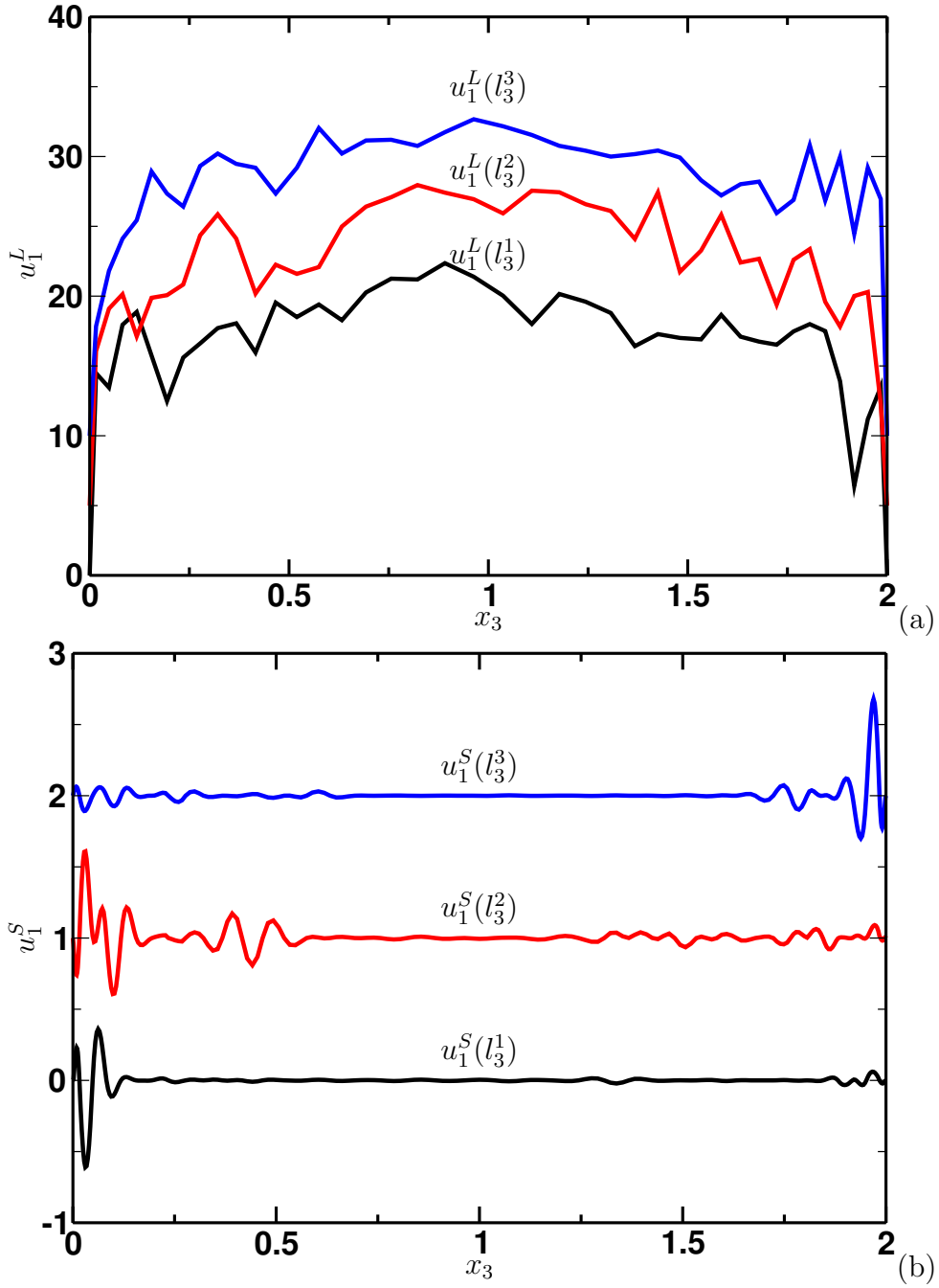

Figure 6.17: Typical instantaneous velocity profiles along different wall-normal lines l_3^1, l_3^2, l_3^3: (a) LS streamwise velocity u_1^L; (b) SS streamwise velocity u_1^S. Two upper profiles of the LS velocity are shifted upwards by 5 and 10, and two upper profiles of the SS velocity are shifted upwards by 1 and 2 respectively.

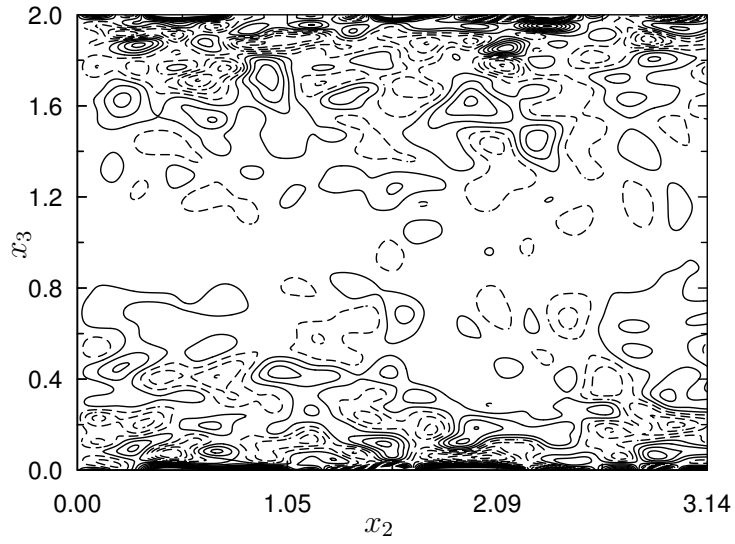

(a)

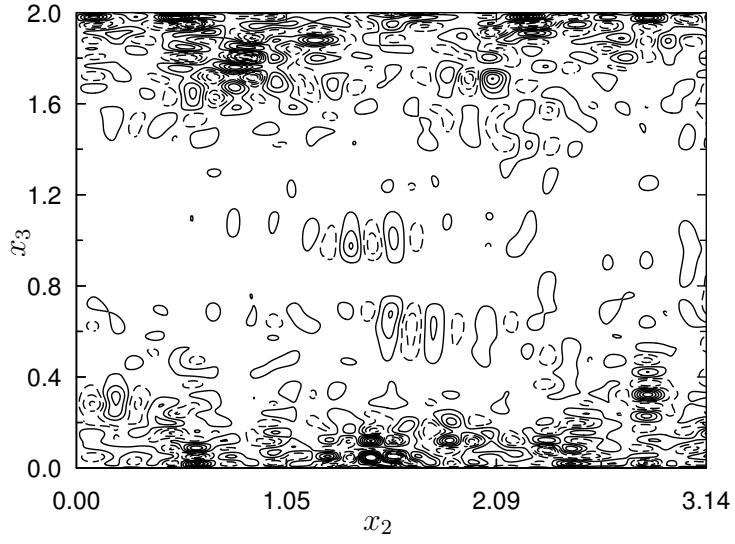

(b)

Figure 6.18: Contours of the streamwise vorticity in x_2x_3 plane: (a) $-120 < \omega_1^L < 120$ with increment of 12; (b) $-30 < \omega_1^S < 30$ with increment of 4. Solid and dashed lines indicate positive and negative vorticity respectively.

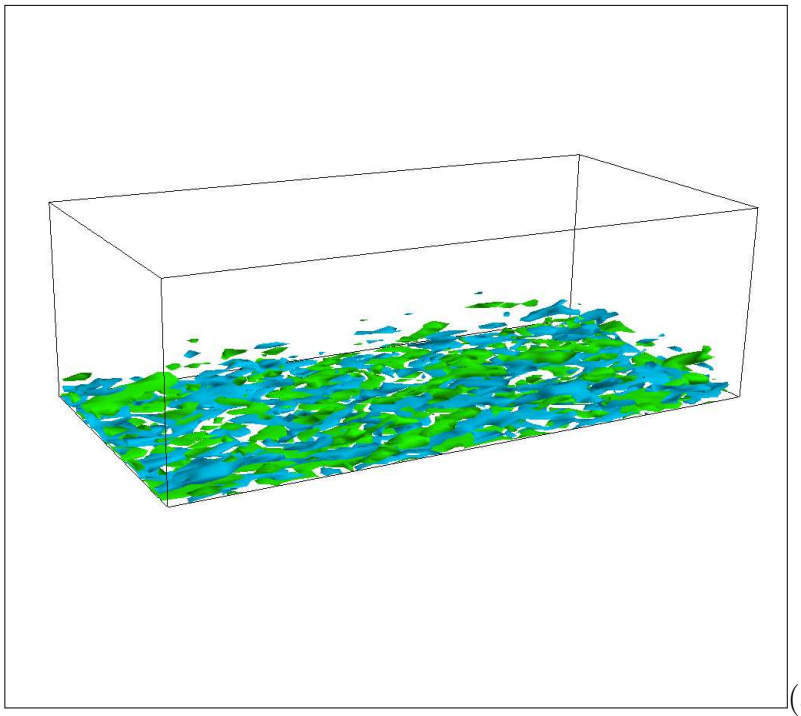

(a)

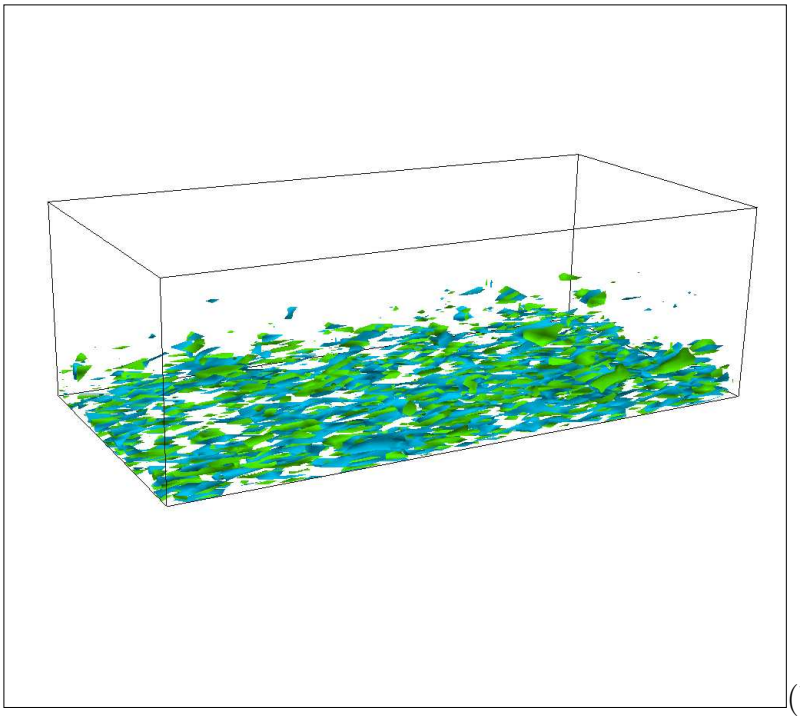

(b)

Figure 6.19: (a) Isosurfaces of the LS streamwise vorticity $\omega_1^L = +30$ (green), $\omega_1^L = -30$ (blue); (b) Isosurfaces of the SS streamwise vorticity $\omega_1^S = +6$ (green), $\omega_1^S = -6$ (blue). Vortical structures at the lower channel wall are shown.

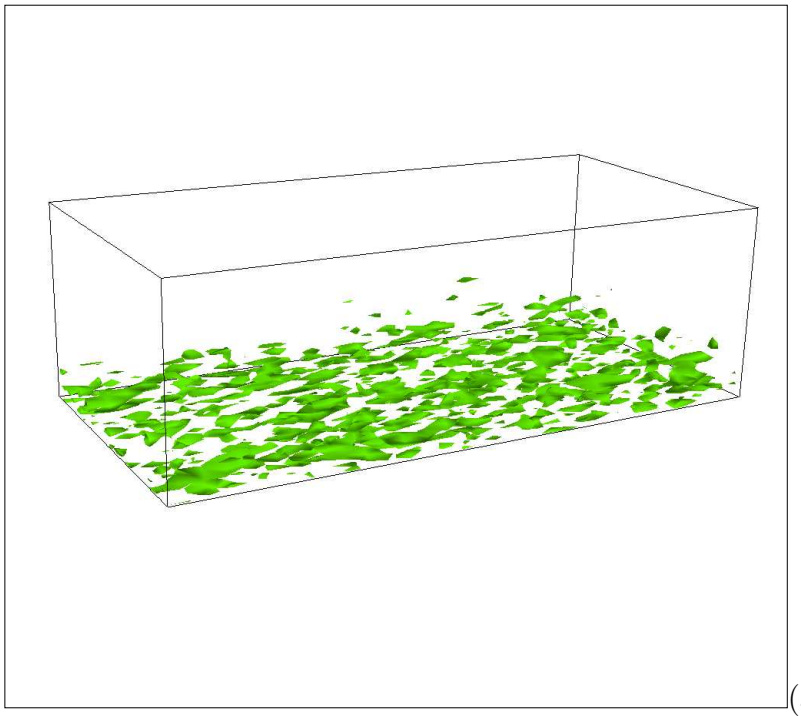

(a)

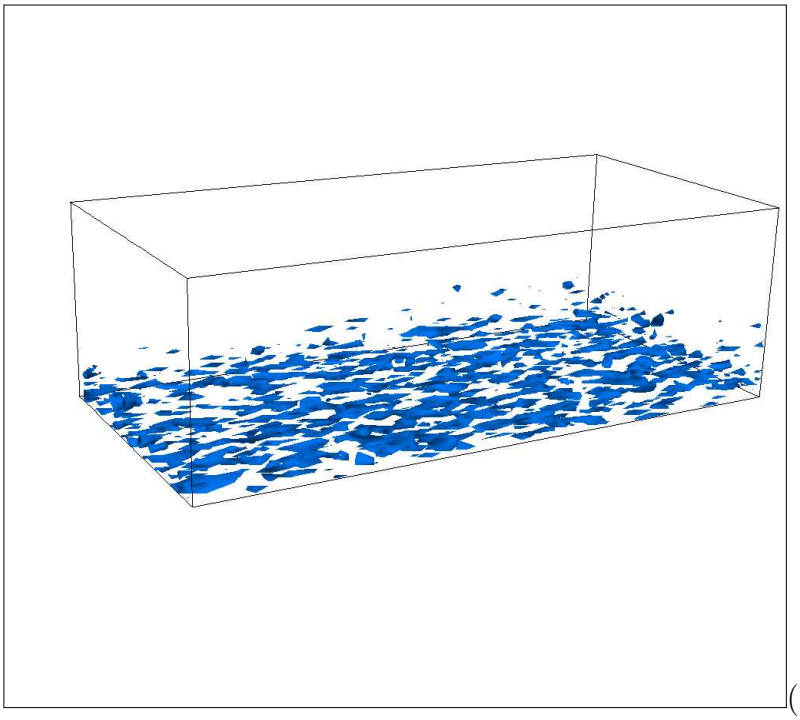

(b)

Figure 6.20: Isosurfaces of the second invariant of the LS and SS velocity gradient tensors: (a) $Q^L = 200$; (b) $Q^S = 20$. Vortical structures at the lower channel wall are shown.

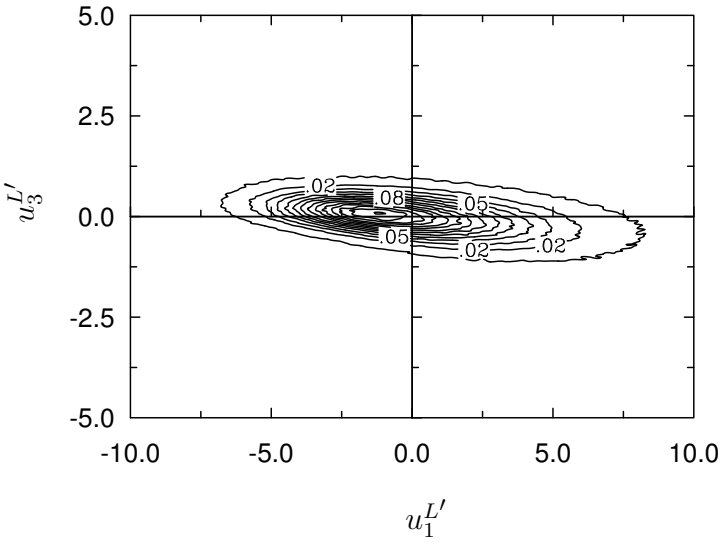

(a)

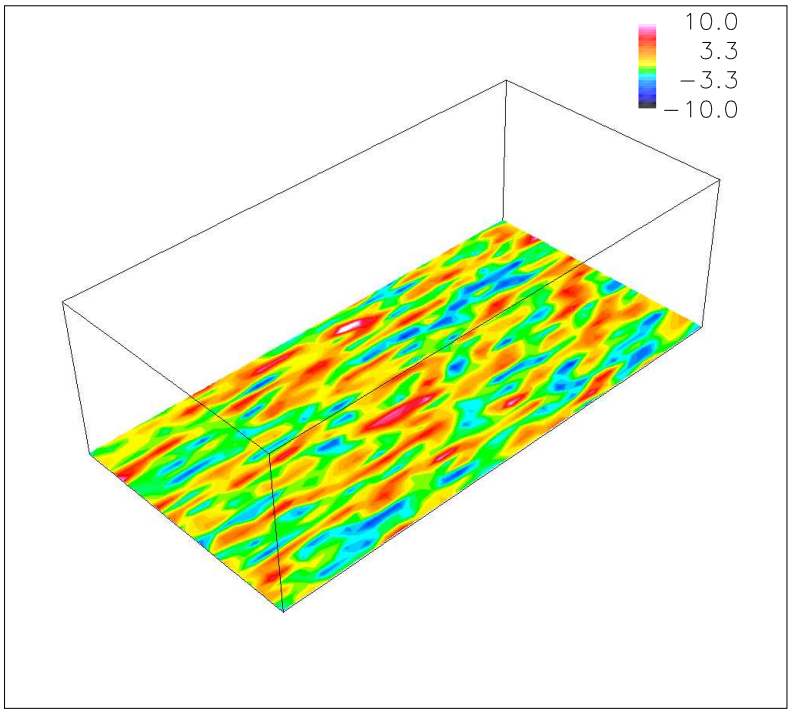

(b)

Figure 6.21: (a) Contour plot of the joint PDF of the streamwise and wall-normal velocity fluctuations at $x_3^+ = 9.5$; (b) Contours of streamwise velocity fluctuations $u_1^{L'}$ at $x_3^+ = 9.5$.

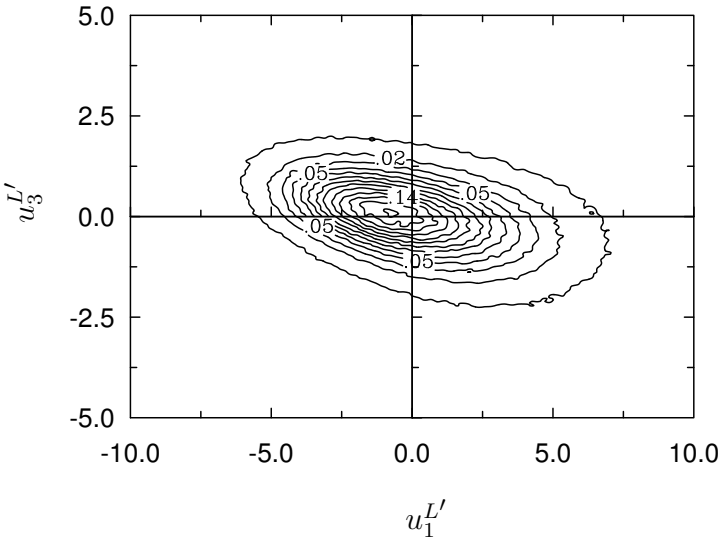

(a)

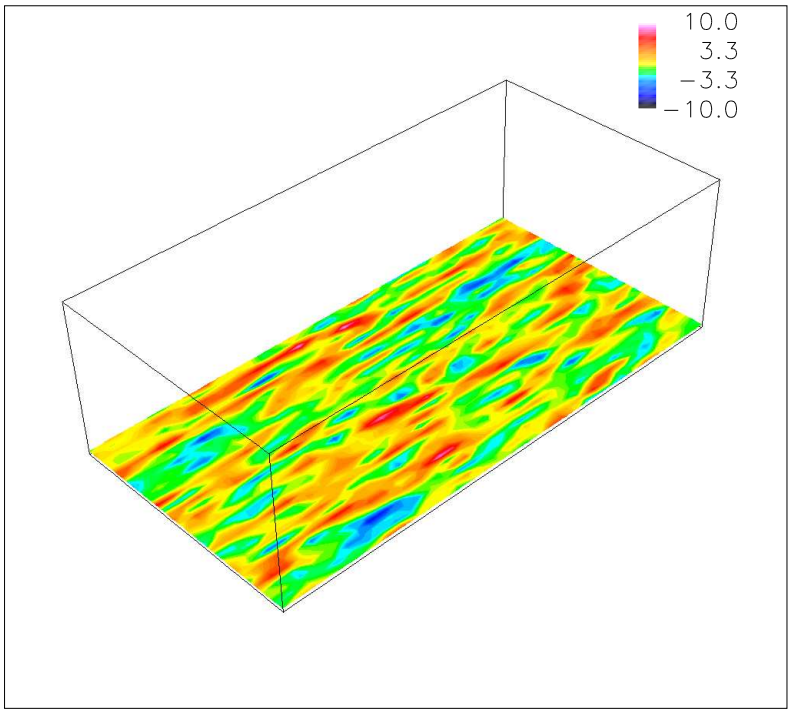

(b)

Figure 6.22: (a) Contour plot of the joint PDF of the streamwise and wall-normal velocity fluctuations at $x_3^+ = 19$; (b) Contours of streamwise velocity fluctuations $u_1^{L'}$ at $x_3^+ = 19$.

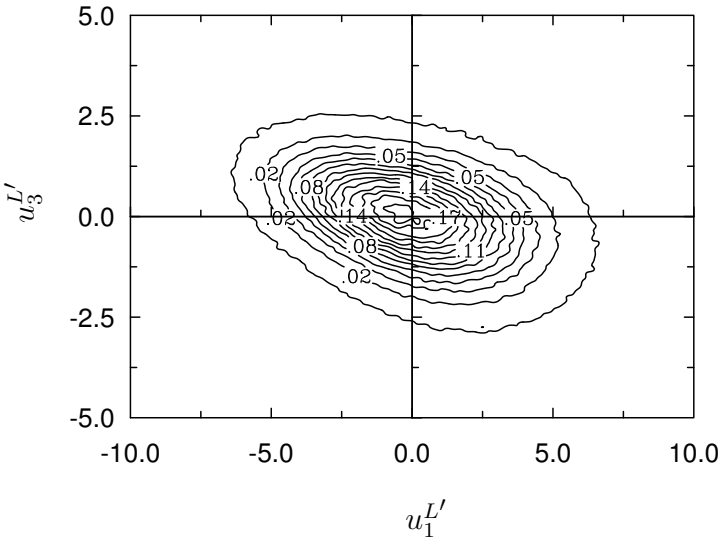

(a)

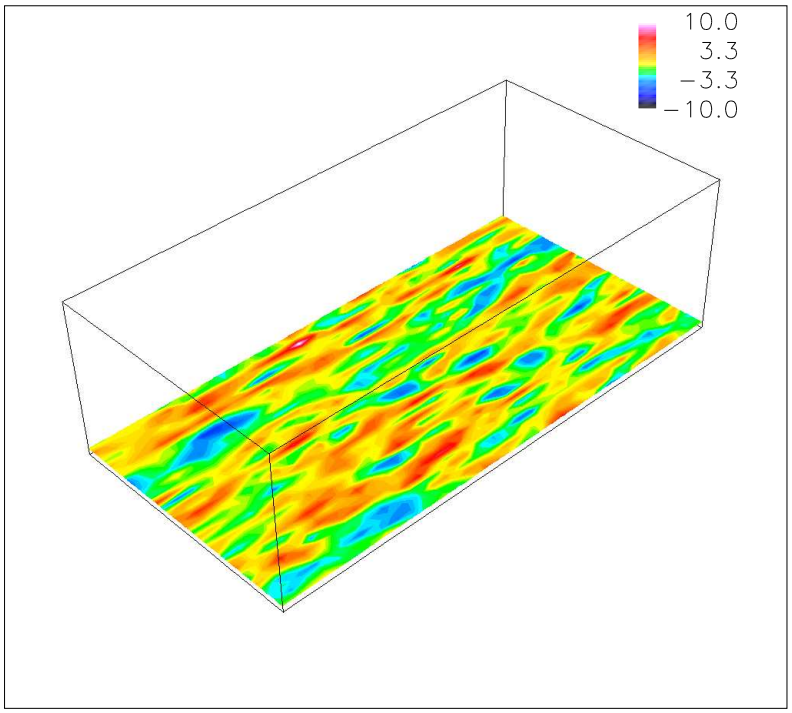

(b)

Figure 6.23: (a) Contour plot of the joint PDF of the streamwise and wall-normal velocity fluctuations at $x_3^+ = 38.5$; (b) Contours of streamwise velocity fluctuations $u_1^{L'}$ at $x_3^+ = 38.5$.

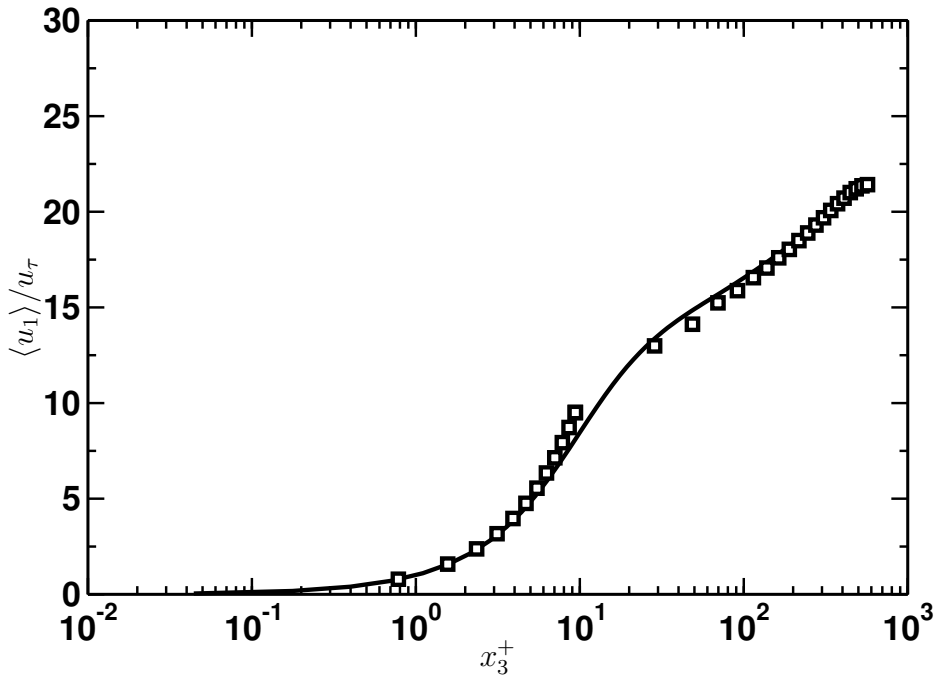

Figure 6.24: Comparison of the normalized mean streamwise velocity obtained from TLS (square symbols) and from DNS (solid line)

9.5, 19 and 38.5. The results are shown in Figs. 6.21(a)-6.23(a). It is seen that the ejection events, which are associated with the second quadrant ($Q2 : u_1^{L\prime} < 0, \quad u_3^{L\prime} > 0$), and the sweep events, which are associated with the fourth quadrant ($Q2 : u_1^{L\prime} > 0, \quad u_3^{L\prime} < 0$), provide major contribution to the PDF. The larger extent of PDF in wall-normal velocity coordinate $u_3^{L\prime}$ at $x_3^+ = 19$ and 38.5 indicates the low-speed streak lift-up in the bursting event. The contours of the streamwise LS velocity fluctuations are shown in Figs. 6.21(b)-6.23(b) and exhibit a characteristic high-speed and low-speed streak pattern.

Finally, the statistical properties of TLS results are compared with results of the DNS of [89], which employed $384 \times 257 \times 384$ grid. Figure 6.24 shows the mean profile of the LS streamwise velocity with respect to the wall-normal coordinate. In general, the TLS profile is very similar to the DNS results especially in the near-wall viscous sublayer and the core region. However, away from the wall, close to the beginning of the buffer layer, the mean streamwise LS velocity is slightly higher magnitudes. The root-mean-square of the LS velocity components and the LS Reynolds stress are plotted in Figs. 6.25(a,b) respectively. The streamwise velocity rms demonstrates the correct behavior in the near-wall region, though it is a little overestimated compared to DNS results. The magnitude of the LS Reynolds stress is a little overestimated also near the wall, but overall, there is a good agreement with DNS results, taking into account significantly coarser resolution than that of DNS. The reasonable accuracy in predicting the peak location and the magnitude of components of the LS Reynolds stress suggests that the TLS approach is able to reproduce some physically consistent

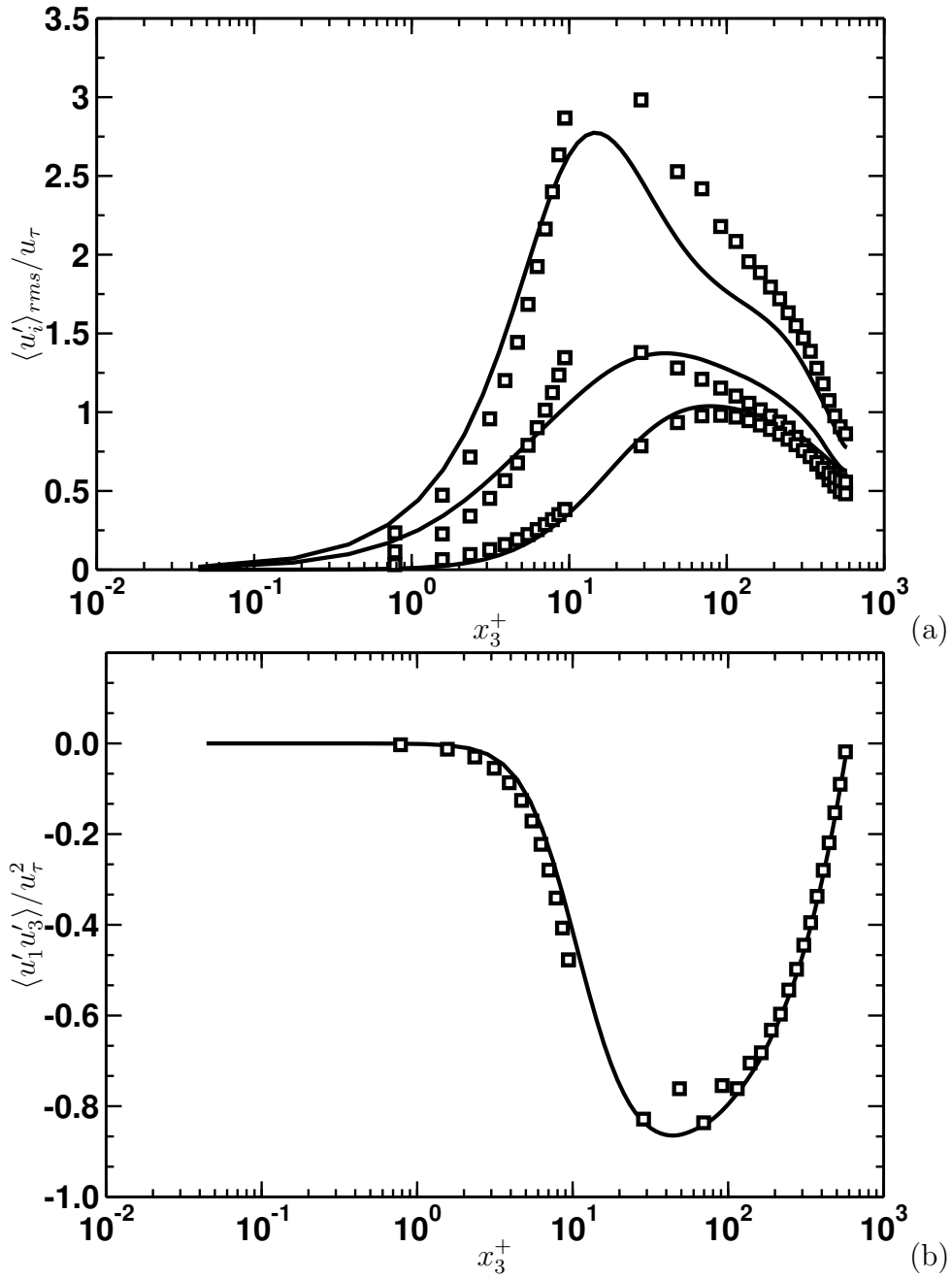

Figure 6.25: Comparison of the normalized rms velocities $\langle u_i' \rangle_{rms}(x_3^+)/u_\tau$ (a) (in descending order: streamwise, spanwise, wall-normal), and the normalized Reynolds stress $\langle u_1' u_3' \rangle(x_3^+)/u_\tau^2$ (b) obtained from TLS (square symbols) and from DNS (solid lines).

features of a wall bounded turbulent flow.

6.4 Temporary Mixing Layers

Temporally evolving mixing layers are simulated primarily with the goal of evaluating performance of TLS approach away from the wall in presence of the LS coherent vortical structures. This type of the flow configuration significantly simplifies numerical implementation since specification of inflow-outflow boundary conditions is avoided, and substituted by the requirement of spatial periodicity in the streamwise (x_1) and spanwise directions (x_2) as well as the free-slip boundary condition in the transverse direction (x_3).

The uniform 32^3 LS grid is employed to discretize a cubic domain of $[0, L] \times [-L/2, L/2] \times [0, L]$ with $L = 4\pi$. All SS lines have uniform resolution of 128 grid points (4 grid points per LS cell). The initialization of the flow velocity field defined as a sum of the mean velocity with the perturbations to the mean. The initial mean velocity is a function of the transverse coordinate only and is given by the hyperbolic tangent profile:

$$U_0^L(x_3) = \frac{1}{2}\Delta U \tanh(x_3/\delta_\omega^0), \tag{6.15}$$

where ΔU is the maximum velocity difference across the mixing layer and δ_ω^0 is the initial vorticity thickness.

Two simulations are performed by superimposing different initial perturbations on the mean velocity profile. In Case 1, the two-dimensional perturbations are imposed on the two-dimensional fundamental and subharmonic modes, derived from the linear Orr-Sommerfeld equation ([93]), along with the three dimensional modes, as used by [94]. Both amplitudes of the two-dimensional fundamental $A_{(1,0)}$ and subharmonic (pairing) modes $A_{(1/2,0)}$ are equal to 0.1 to allow rapid growth of these modes. In this representation, (m, n) is a single mode with the amplitude $A_{(m,n)}$, where m and n are the streamwise and spanwise specific wave-numbers respectively. In the presence of the initial perturbation of the unstable subharmonic mode $(1/2, 0)$, the fundamental instability mode experiences the roll-up with successive vortex pairing ([94]). The initial amplitude of the three dimensional perturbation $A_{(1,1)}$ is 0.001, and typically chosen to be small ($A_{(1,1)} \ll A_{(1,0)}$) but also large enough to introduce three-dimensionality in the flow in reasonable time. In Case 2, three-dimensional broadband random perturbations with intensity $\epsilon_{3D} = 0.01$ are imposed on the mean velocity profile. For both cases the initial Reynolds number based on the initial vorticity thickness $Re_\omega = \Delta U \delta_\omega^0/\nu$ is approximately equal to 468.

To study the development of the two-dimensional modes and the three-dimensionality, one must define corresponding modal energies $E_{(m,n)}$. Energy of the fundamental $(1, 0)$ and subharmonic $(1/2, 0)$ modes as well as the total energy in the three-dimensional modes (E_{3D}) are:

$$E_{(1,0)} = \int_{-L/2}^{L/2} \widehat{u_i^L}(1, 0, x_3)\widehat{u_i^L}^*(1, 0, x_3)\mathrm{d}x_3, \tag{6.16}$$

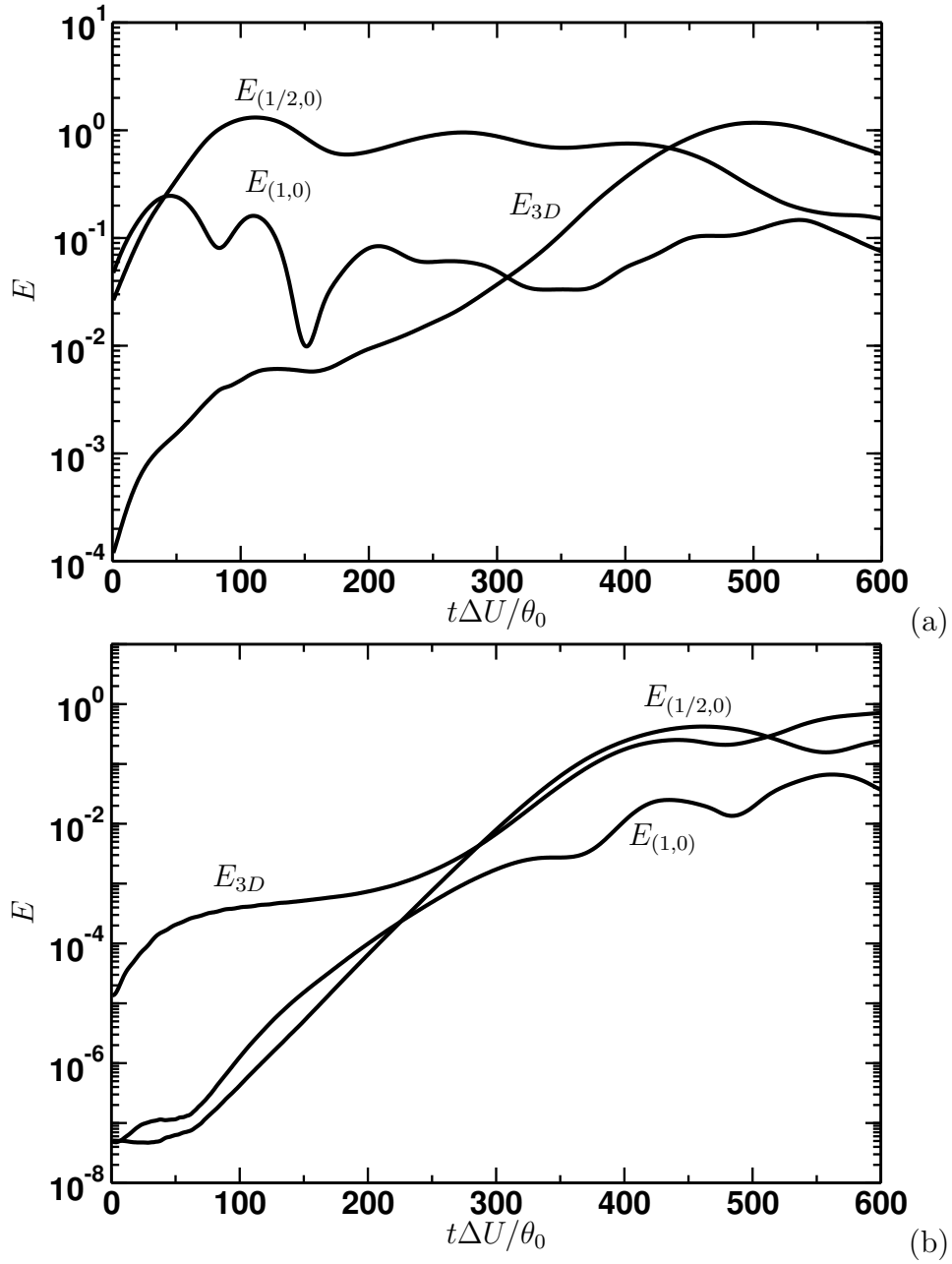

Figure 6.26: Energy growth of the fundamental modes $E_{(1,0)}$, the subharmonic modes $E_{(1/2,0)}$ and the 3D disturbances E_{3D}: (a) Case 1; (b) Case 2.

$$E_{(1/2,0)} = \int_{-L/2}^{L/2} \widehat{u_i^L}(1/2,0,x_3)\widehat{u_i^L}^*(1/2,0,x_3)\mathrm{d}x_3, \tag{6.17}$$

$$E_{3D} = \sum_{n\neq 0}\sum_{m}\int_{-L/2}^{L/2} \widehat{u_i^L}(m,n,x_3)\widehat{u_i^L}^*(m,n,x_3)\mathrm{d}x_3 \tag{6.18}$$

Here, $\widehat{u_i^L}(m,n,x_3)$ is the Fourier coefficient of the mode (m,n) in the Fourier series representation of the LS velocity u_i^L with respect to the streamwise (x_1) and the spanwise (x_2) directions, and $\widehat{u_i^L}^*$ is the complex conjugate. Time evolution of the modal energy for both cases is exhibited in Fig. 6.26 (a,b). The fundamental mode grows first and saturates before the subharmonic modes. In Case 1, the non-dimensional rollup time (the time needed for the energy $E_{(1,0)}$ to reach its first maximum value) is about 50. The pairing time (the time when the energy of two-dimensional subharmonic modes reaches the first maximum) is about twice the rollup time. The momentum thickness θ, which is defined as

$$\theta = \int_{-L/2}^{L/2}\left[\frac{1}{4} - \Big(\frac{U^L}{\Delta U}\Big)^2\right]\mathrm{d}x_3, \quad U^L(x_3) = \frac{1}{L^2}\int_0^L\int_0^L u_1^L \mathrm{d}x_1\mathrm{d}x_2, \tag{6.19}$$

also attains its local maximum around the pairing time as shown in Fig. 6.27. Further growth of the mixing layer ends with the completion of the vortex pairing process. These results agree very well with past DNS studies [95, 96]. In Case 2, on the contrary, the growth of the momentum thickness is delayed significantly due to the absence of the two-dimensional perturbations in initial velocity field. After the long slow-growth transient period the momentum thickness demonstrates a much higher growth rate when the non-dimensional time T exceeds value of 300. At that time the energy of the subharmonic modes overcomes the energy of the three-dimensional modes and starts playing dominant role in growth of the mixing layer. After the modal energy $E_{(1/2,0)}$ reaches the maximum value at the time of 450, the growth of the momentum thickness slows down. After this time, the further growth in the momentum thickness is primarily due to evolution of the three dimensional modes which become energetically dominant, and as a result, significantly distort the LS vortical structures as shown in Fig. 6.29(e).

Some qualitative features of the LS and SS vortical structures is often visualized by considering the spanwise vorticity component. Because of the adopted coarse 32^3 resolution of the LS grid, the dynamics of the SS structures can not be correctly captured based on their LS values only. However, the SS vorticity field can be estimated based on the reconstructed SS velocity along the SS lines.

Figures 6.28(a-f) and 6.29(a-f) show the contours of the spanwise vorticity component at three consecutive instants of the non-dimensional time $T^I = 36, 110, 184$ and $T^{II} = 323, 416, 560$ for Case 1 and Case 2 respectively. The contours of the LS spanwise vorticity for Case1 (Figs. 6.28(a,c,e)) exhibit the rollup, the pairing and the post-pairing stages of the mixing layer development. During the pairing, two well-developed vortices generated by the roll-up of the fundamental mode come together and merge to form a new bigger vortex core. The contour plots of the SS spanwise vorticity are shown in Figs 6.28(b,d,f) and demonstrate clusters of small counterrotating

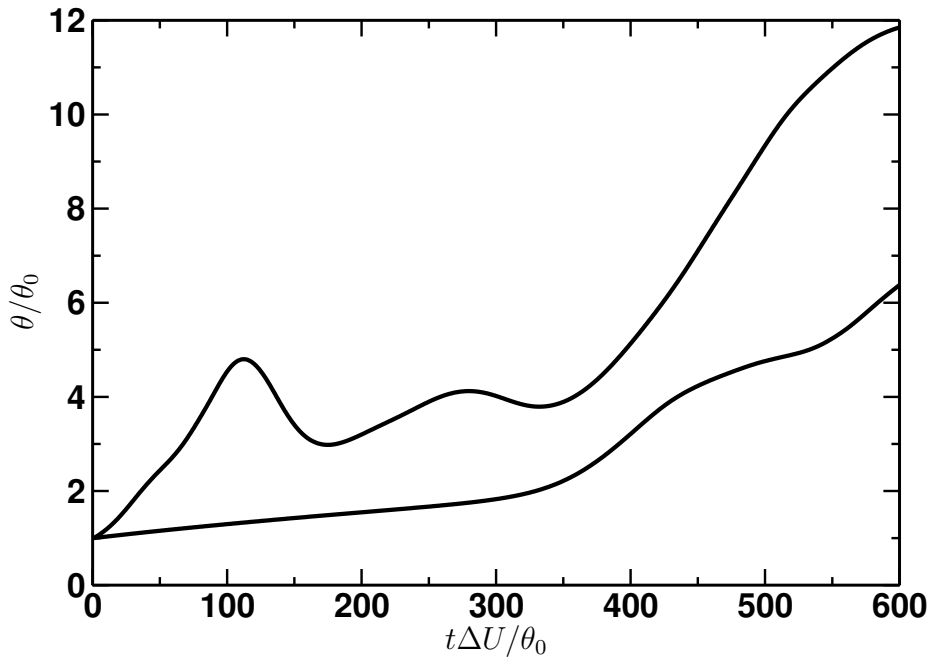

Figure 6.27: Evolution of the momentum thickness: Case 1 - upper line, Case 2 - lower line.

vortices which exist in high gradient regions of the LS spanwise vorticity. The peak intensities of the SS spanwise vorticity steadily decrease as the LS two-dimensional vortical structures develop absorbing energy from the SS field. At $T^I = 184$ the maximum (minimum) value of the SS spanwise vorticity is 2.07 (-2.32) respectively, and is down from the corresponding values of 2.52 (-2.72) at $T^I = 36$. In Case 2, the SS vortices are still created in regions where the large spatial changes of the LS vorticity prevail as shown in Figs. 6.29(b,d,f). However, the peak intensities of the SS spanwise vorticity constantly grows from $max(\omega_2^S) = 1.69$ ($min(\omega_2^S) = -1.95$) at $T^{II} = 323$ to $max(\omega_2^S) = 4.46$ ($min(\omega_2^S) = -4.46$) at $T^{II} = 560$, suggesting the forward cascade of energy from the LS to the SS as the three-dimensional modes prevails and the flow loses its initial two-dimensional structure and becomes completely turbulent.

The qualitative difference of the LS vortical structures in Case 1 and Case 2 is further evident if one considers the second invariant of the velocity-gradient tensor which is often used to identify vortex regions which exhibit significant rotational motions.

Isosurfaces of the second invariant of the LS and the SS velocity-gradient tensors for both Cases are exhibited in Figs. 6.30 and 6.31, respectively. The positive regions of the LS invariant Q^L are shown at two levels equal to 0.12 and 11.0. Figure 6.30(a) demonstrates the basic 3D structure in the mixing layers. Pairing of two spanwise vortices is highlighted by the isosurface of the higher value of Q^L. In mixing layers, two dimensional LS structures are subject to three-dimensional instabilities, which is manifested by existence of counter-rotating streamwise "rib" vortices, and have been studied extensively in the past ([94]). These vortices are developed in the braid region

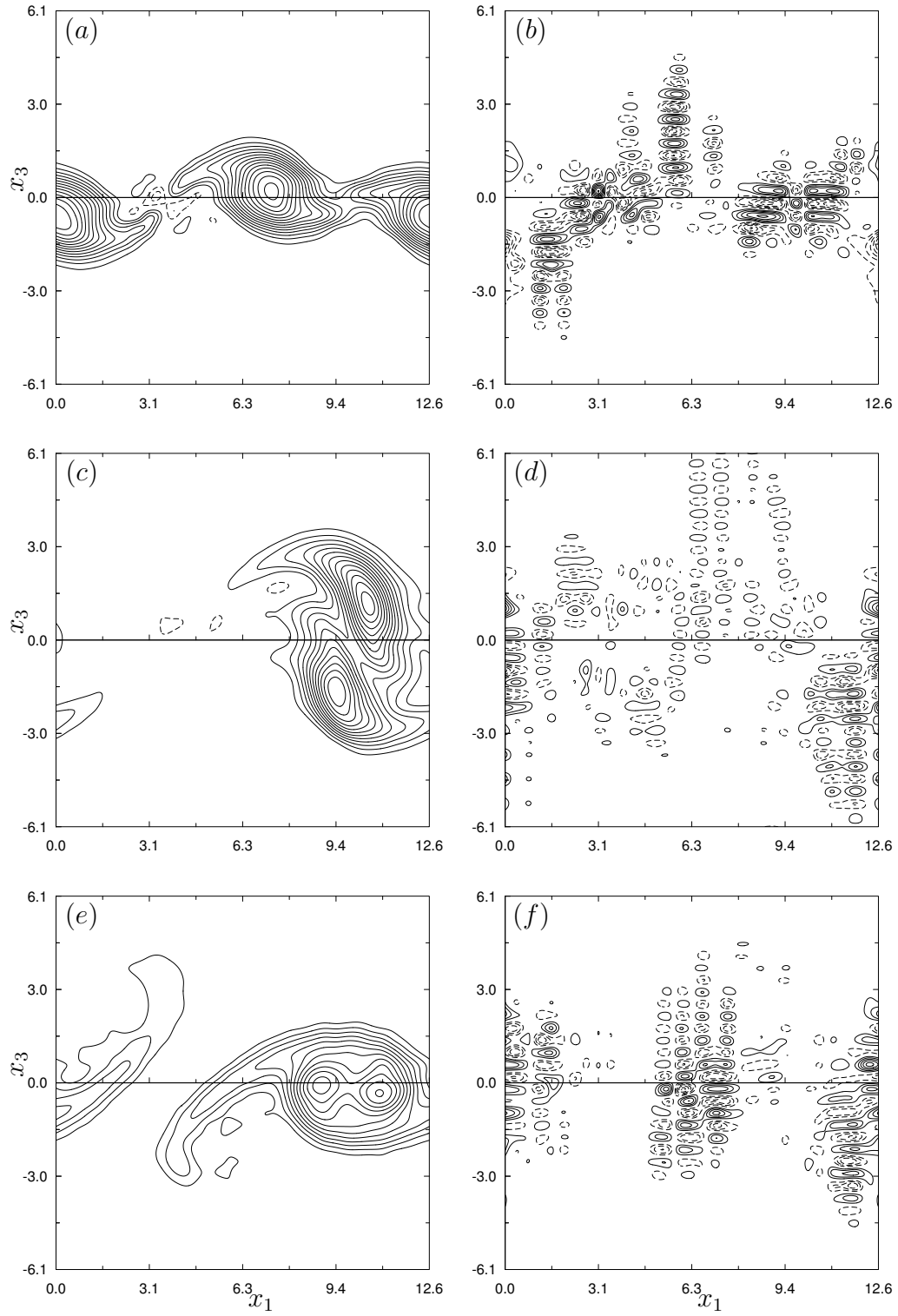

Figure 6.28: Contours of the LS and SS spanwise vorticity for Case 1 at $T = 36$, 110, 184, $x_2 = 0.75L$: (a), (c), (e) $-16 < \omega_2^L < +8$, contour interval is 0.8; (b), (d), (f) $-4.5 < \omega_2^S < +4.5$, contour interval is 0.45. Positive and negative vorticity is indicated by dash and solid lines.

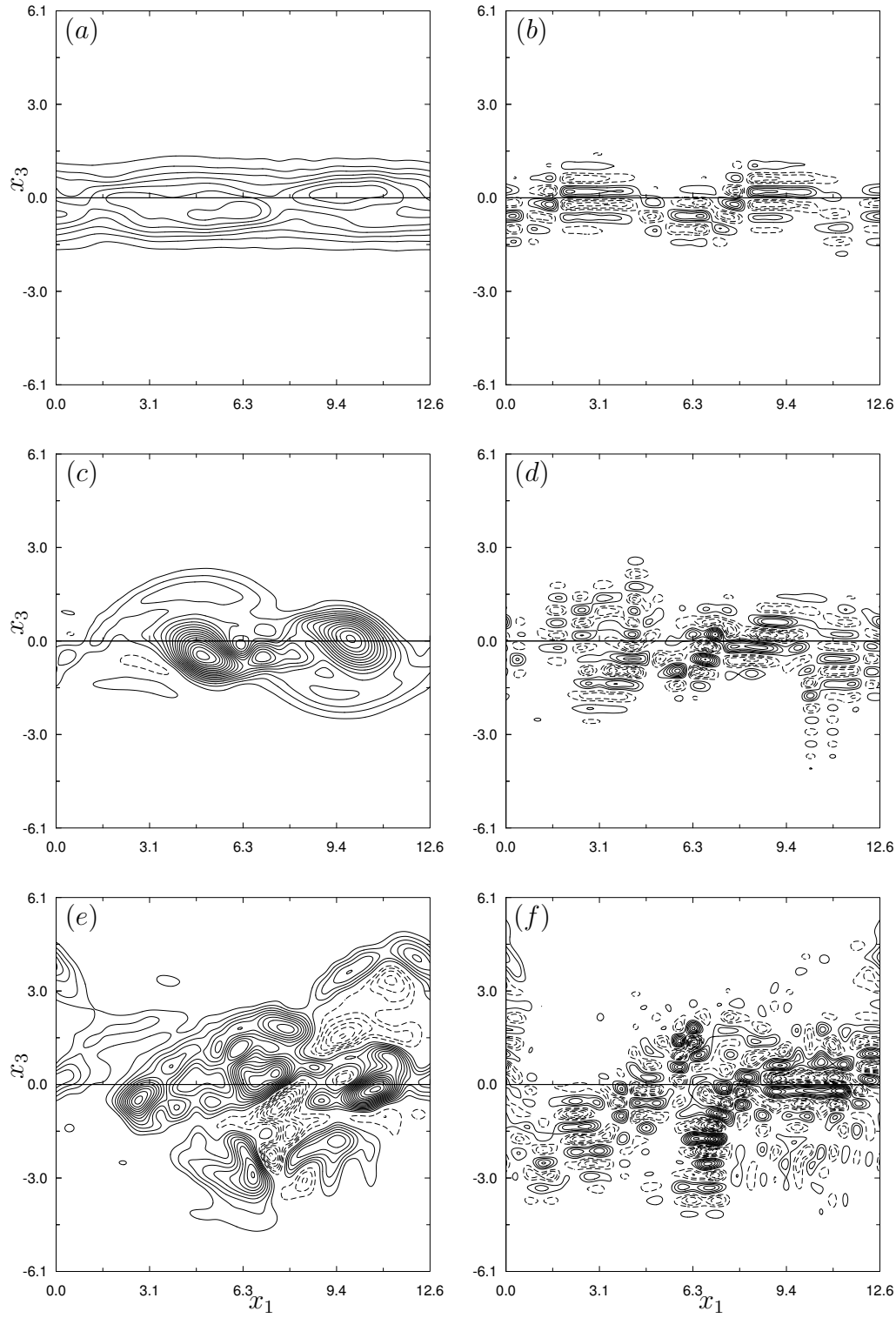

Figure 6.29: Contours of the LS and SS spanwise vorticity for Case 2 at $T = 323$, 416, 560, $x_2 = 0.75L$: (a), (c), (e) $-16 < \omega_2^L < +8$, contour interval is 0.8; (b), (d), (f) $-4.5 < \omega_2^S < +4.5$, contour interval is 0.45. Positive and negative vorticity is indicated by dash and solid lines.

and extend from the bottom of one vortex core to the top of the next. This structure is clearly visualized by lower value of Q^L. Figure 6.31(a) shows the LS vortical structure for the Case 2 at later time $T^{II} = 560$, when the two dimensional subharmonic and the counter-rotating streamwise vortices are already significantly distorted. These LS vortical structures strongly affect the corresponding SS field. In Case 1 (Fig. 6.30(b)), the SS invariant exhibits an approximate, quasi-two-dimensional pattern, while Case 2 is characterized by almost structureless, random SS vorticity regions as shown in Fig. 6.31(b). Structural features of the LS and SS streamwise vorticity components in the cross-sectional plane are shown in Figs. 6.32 and 6.33. In Case 1 the LS streamwise vortical ribs consists of the counter-rotating vortices. It is interesting to note that the corresponding SS vorticity exhibits repeatable pattern with a period equals to that of the LS vorticity.

Finally, turbulent statistics is examined to determine whether the development of the mixing layer reaches the self-similar stage. The well-known property of the turbulent mixing layer is the self-similar evolution after an initial transient stage, provided the sufficiently large computational domain and the high Reynolds number. The notion of the self-similarity of turbulent mixing layers has been widely addressed in literature by both experimental ([97, 98]) and computational ([99, 100]) studies. The self-similarity regime is usually characterized by the linear growth of the layer momentum thickness in time and by coinciding profiles of the normalized turbulent intensities for different times (or downstream locations for spatially evolving mixing layers). However, the non-dimensional times of the beginning and the end of the self-similar regime are strongly depend in the initial conditions which makes the meaningful comparison of experimental and numerical (DNS or LES) results somewhat difficult. In addition, the experimental and numerical findings ([101, 102]) suggest that the turbulent statistics as well as the flow structure are strongly affected by the initial conditions and the computational domain size. The significant differences exist in all stages of the mixing layer development including the self-similar regime leading to multiple, non-unique self-similar states. As a result, any validative conclusions drawn on routinely compared data from the different numerical (DNS or LES) and experimental configurations are based on implicit assumption of the unique self-similar state and, therefore, should taken with caution.

The purpose of the current simulation is not to study self-similar states of the turbulent mixing layer (which would require a large domain allowing more successive vortex pairing) but rather to establish general applicability of the TLS approach to a turbulent flow with persistent LS coherent structures. Therefore, despite the significant difference in the initial conditions, it is instructive to compare qualitatively the TLS results of Case 2 with DNS results of [99] and experimental results of [98]. A Galerkin spectral method was employed in the DNS with resolution of $512 \times 210 \times 192$ modes and the initial vorticity thickness Reynolds number Re_ω of 1370. Initial velocity field was generated by bringing together two turbulent boundary layer realizations with their respective free streams moving in opposite directions. In the experimental work of [98] a mixing layer originated from two tripped splitter-plate boundary layers with the momentum thickness Reynolds numbers Re_θ equal to 804 and 567 respectively.

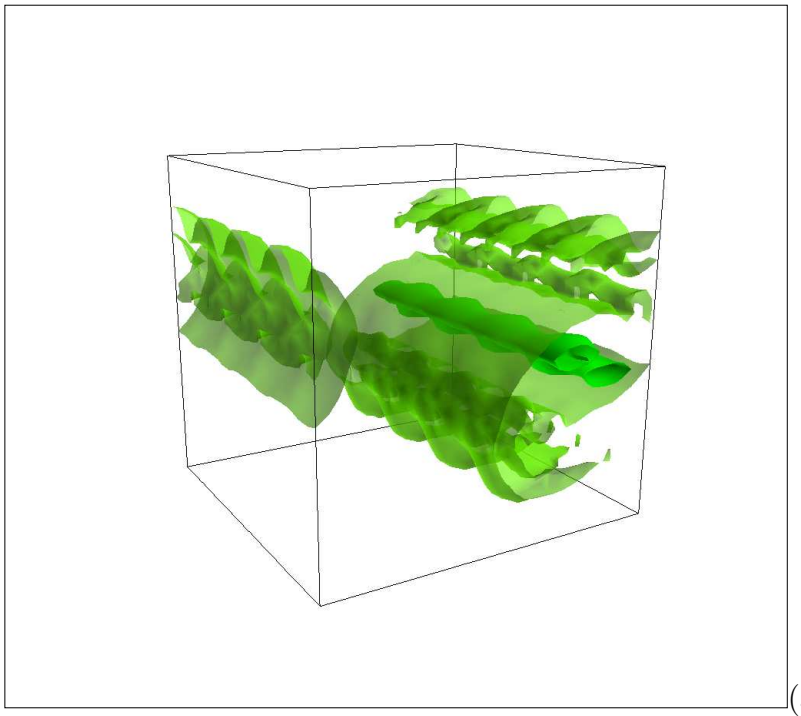

(a)

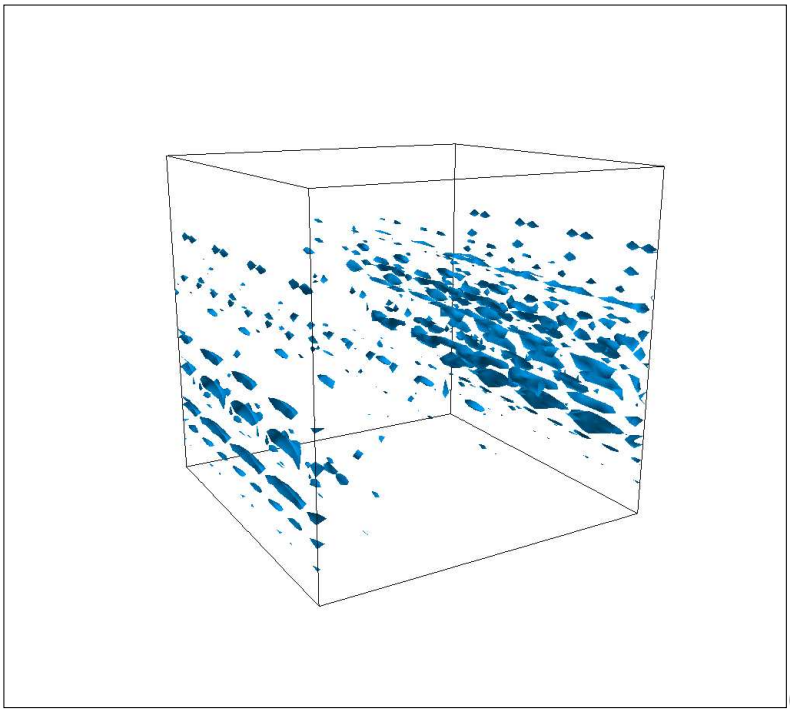

(b)

Figure 6.30: (a) Isosurfaces of the second invariant $Q^L = 0.12$ (light, transparent) and $Q^L = 11$ (dark) at $T = 147$; (b) Isosurfaces of the second invariant $Q^S = 0.12$ at $T = 147$.

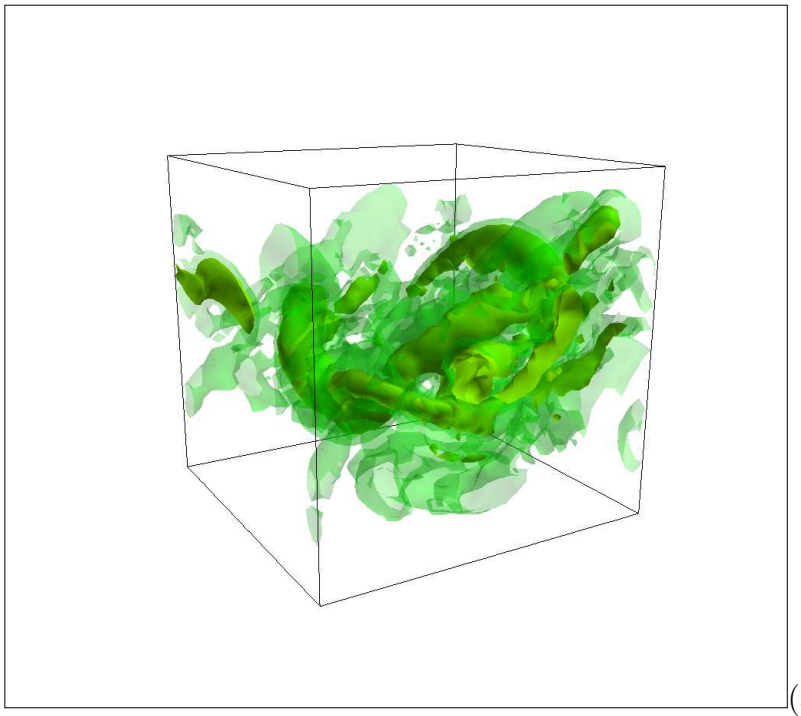
(a)

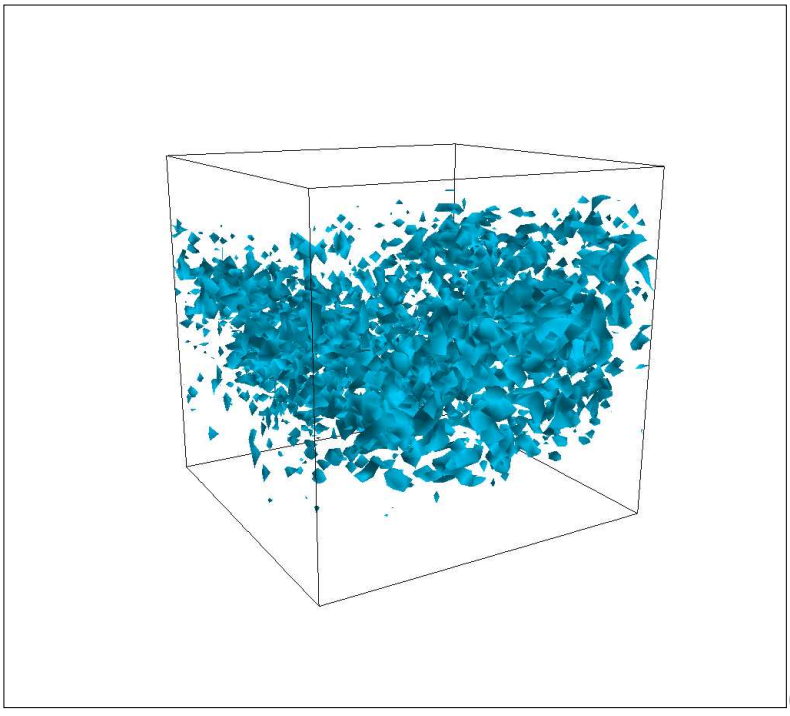
(b)

Figure 6.31: (a) Isosurfaces of the second invariant $Q^L = 0.12$ (light, transparent) and $Q^L = 11$ (dark) at $T = 560$; (b) Isosurfaces of the second invariant $Q^S = 0.12$ at $T = 560$.

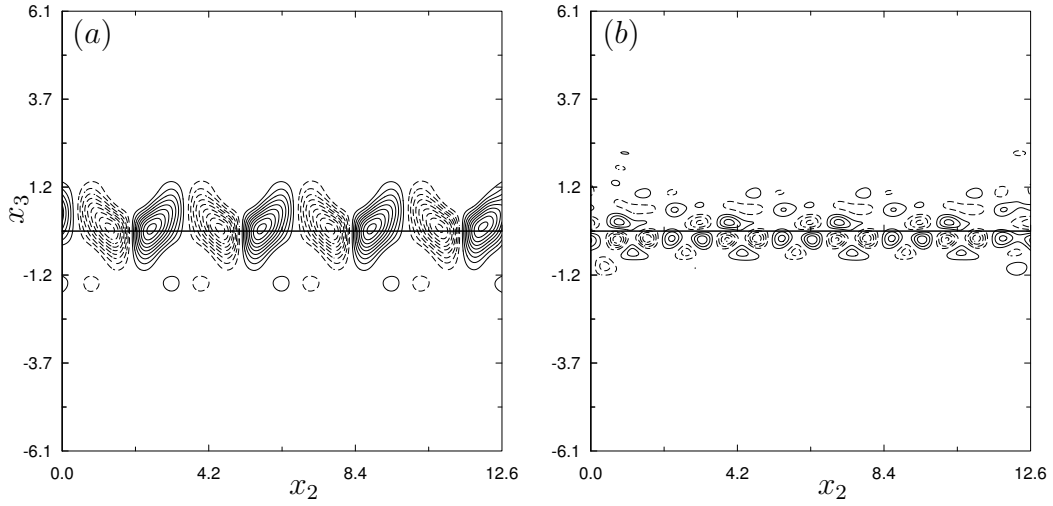

Figure 6.32: Contours of the streamwise vorticity for Case 1 at $T = 110$ and $x_1 = 0.31L$: (a) LS vorticity $-1.6 < \omega_1^L < +1.6$, contour interval is 0.16; (b) SS vorticity $-1.0 < \omega_1^S < +1.0$, contour interval is 0.1. Positive and negative vorticity is indicated by dash and solid lines, respectively.

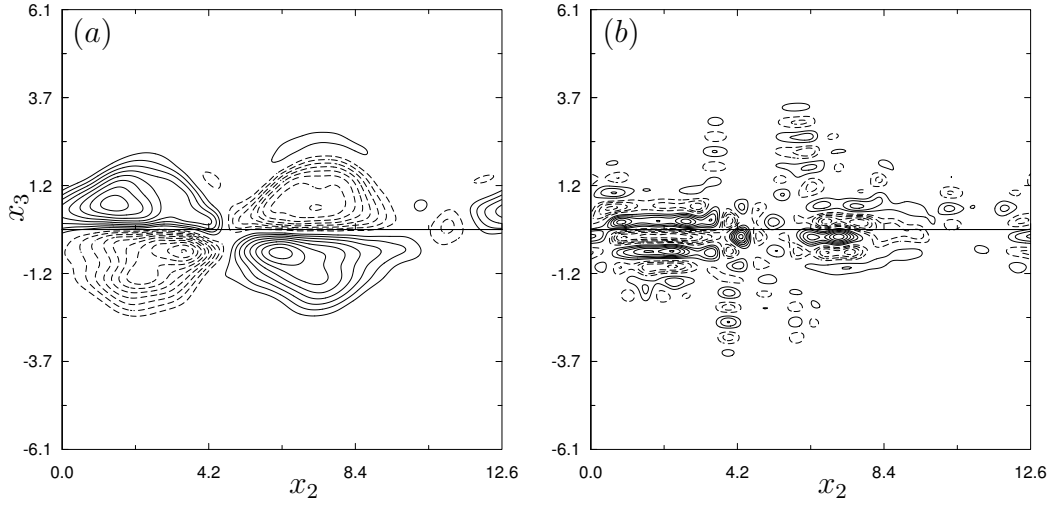

Figure 6.33: Contours of the streamwise vorticity for Case 2 at $T = 416$ and $x_1 = 0.6L$: (a) LS vorticity $-7 < \omega_1^L < +7$, contour interval is 0.7; (b) SS vorticity $-3.5 < \omega_1^S < +3.5$, contour interval is 0.5. Positive and negative vorticity is indicated by dash and solid lines, respectively.

Figure 6.27 shows that the evolution of the momentum thickness is not fully linear in the turbulent regime, except a small time interval around $T^{II} = 500$. However, the exact estimation of the starting point of the self-similarity is difficult. The momentum thickness is based on integration of the mean LS velocity and therefore, numerical estimations that are based on the explicit calculation of the momentum thickness higher derivatives bear an unavoidable degree of arbitrariness. More transparent estimation can be obtained by considering evolution of statistical quantities such as the integrated dissipation or the resolved turbulent kinetic energy $E^L = \langle u_i^{L\prime} u_i^{L\prime} \rangle / 2$ at $x_3 = 0$, which should not depend on time during the self-similar period ([99, 103]). Here, $u_i^{L\prime}$ denotes the fluctuating LS velocity field. Time evolution of the LS and the SS turbulent kinetic energies at $x_3 = 0$ are shown in Fig. 6.34. It appears that an approximate self-similar regime is reached for the non-dimensional times greater then 460. Note that the corresponding SS turbulent kinetic energy, computed as the total SS energy averaged over the lines belonging to $x_3 = 0$ plane, also demonstrates the similar trend until about $T^{II} = 530$. Due to the finite size of the computational domain the statistics eventually decay.

Space averaged mean velocity profile is shown in Fig. 6.35 and agrees well with DNS and experimental results. Figures 6.36 demonstrates RMS of the LS velocity fluctuations. Despite very different initial conditions adopted in both DNS and experimental studies as well as the coarse LS resolution of the TLS case, turbulent intensities of the LS field shows qualitatively good agreement with DNS and experimental results. Some differences in predicting peak values of the turbulent intensities may be also attributed to insufficient statistical sample due to the limited and approximate existence of the self-similar stage. Here, the role of the computational domain is particular important. As reported by [102], who recently conducted the high resolution LES study of the self-similar regimes in turbulent mixing layers, the combined effect of different initial conditions and domain sizes can result in up to 83% difference in predicting peak values of turbulent intencities, where the spanwise velocity component is the most affected.

Overall, these results suggest that the SS velocity field generated by the simplified SS Eq.(4.26) is capable to capture physically relevant details of turbulent flow pattern in the presence of the LS coherent structures which makes the TLS approach feasible for extension to treat complex, massively separated flows.

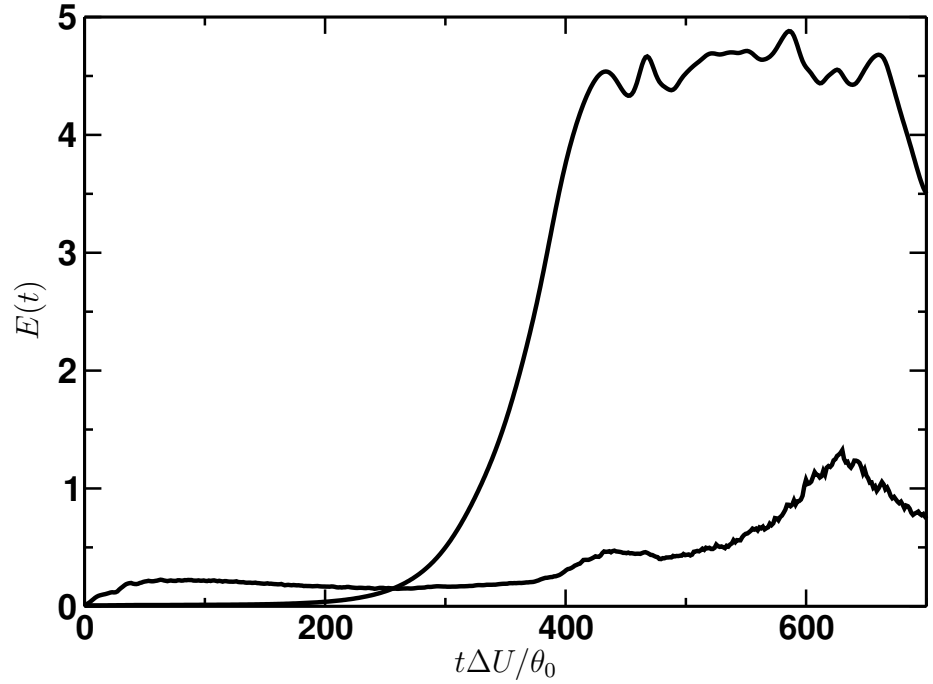

Figure 6.34: Evolution of the LS $E^L(t)$ (upper line) and the SS $E^S(t)$ (lower line) turbulent kinetic energies at $x_3 = 0$. $E^S(t)$ is multiplied by 20 to enable comparison.

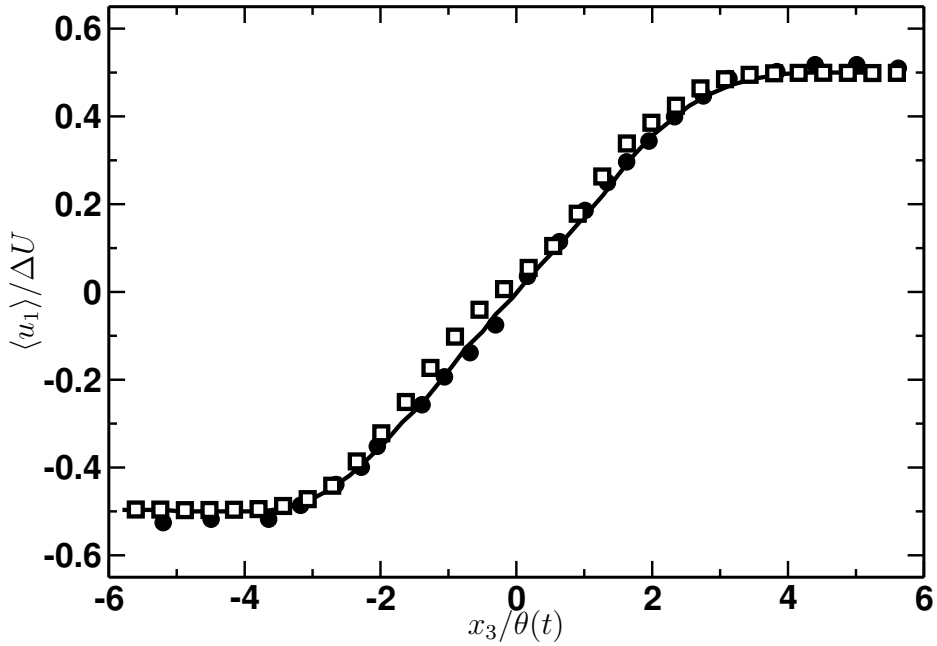

Figure 6.35: Space-averaged LS streamwise velocity at $T = 510$ (open squares) compared with the mean streamwise velocity for the self-similar state obtained in DNS (line), [99] and experimental studies (circles), [98].

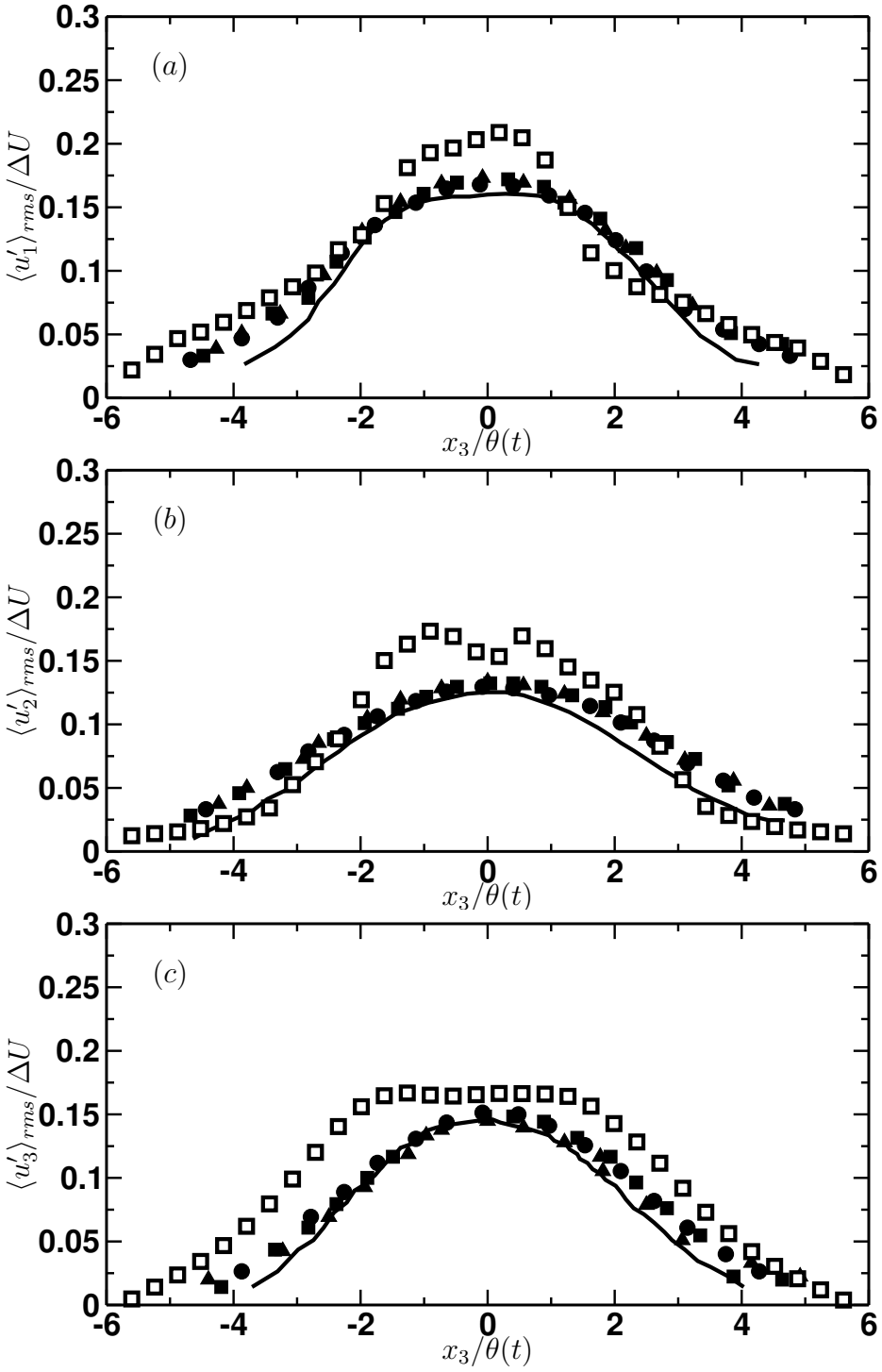

Figure 6.36: Space-averaged LS rms velocities at $T = 510$ (open squares): streamwise (a), spanwise (b), normal (c), compared with the rms velocities for the self-similar state obtained in DNS (line) and experimental studies (symbols).

CHAPTER VII

HYBRID TLS-LES MODEL

7.1 Description of the Scale Separation Problem

Both LES and TLS approaches are rely on scale separation procedure. In the case of LES, it is obtained by applying a filter to the actual field, yielding

$$\phi(x,t) = \overline{\phi}(x,t) + \phi''(x,t) \tag{7.1}$$

with

$$\overline{\phi}(x,t) = \int \phi(x',t) G(x,x' : \overline{\Delta}) dx' \tag{7.2}$$

where ϕ is a space- and time- dependent variable, G is the filter function, and $\overline{\Delta}$ is the cut-off filter width.

In the case of TLS, scale separation is obtained via a LS function leading to:

$$\phi(x,t) = \phi^L(x,t) + \phi^S(x,t) \tag{7.3}$$

with

$$\phi^L(x,t) = L^{\triangle}\phi(x,t) \tag{7.4}$$

where operator $L^{\triangle}$ is analogous to underlying LS grid.

7.2 Governing Equations for Resolved Motion

The equations for resolved motion for compressible flows can be obtained by applying the one of the two scale separation procedures (here represented by superscript L) to the NS equations. From this application, the evolution of the resolved motion can be represented by the following equations:

$$\begin{aligned}
\frac{\partial \rho^L}{\partial t} &+ \frac{\partial}{\partial x_i}(\rho u_i)^L = 0 \\
\frac{\partial}{\partial t}(\rho u_i)^L &+ \frac{\partial}{\partial x_j}\Big[(\rho u_i)^L u_j^L + p^L \delta_{ij} - \tau_{ij}^L\Big]^L = R_1 \\
\frac{\partial}{\partial t}(\rho E)^L &+ \frac{\partial}{\partial x_i}\Big[(\rho E)^L u_i^L + (p^L u_i^L)^L + q_i^L - (\tau_{ij}^L u_j^L)^L\Big]^L = R_2 + R_3 + R_4
\end{aligned} \tag{7.5}$$

The viscous stress tensor τ_{ij}^L and the heat flux vector q_i^L is defined as

$$\tau_{ij}^L = \mu\left(\frac{\partial u_i^L}{\partial x_j} + \frac{\partial u_j^L}{\partial x_i}\right) - \frac{2}{3}\mu \frac{\partial u_k^L}{\partial x_k}\delta_{ij} \tag{7.6}$$

$$q_i^L = -k\frac{\partial T^L}{\partial x_i}. \tag{7.7}$$

The ideal gas law is

$$p^L = \rho^L R T^L. \tag{7.8}$$

The unresolved terms appearing in the momentum and energy equation are defined as follows:

$$\begin{aligned} R_1 &= -\frac{\partial}{\partial x_i}\Big[(\rho u_i u_j)^L - (\rho u_i)^L u_j^L\Big] \\ R_2 &= -\frac{\partial}{\partial x_i}\Big[(\rho E u_j)^L - (\rho E)^L u_j^L\Big] \\ R_3 &= -\frac{\partial}{\partial x_i}\Big[(p u_j)^L - p^L u_j^L\Big] \\ R_4 &= -\frac{\partial}{\partial x_i}\Big[(\tau_{ij} u_j)^L - \tau_{ij}^L u_j)^L\Big] \end{aligned} \tag{7.9}$$

The specific closures for these terms associated with LES and TLS approaches are described in the following sections.

7.3 LES Closure

The most common way of representing the unresolved motion is based on eddy viscosity type of models. From this definition, we get:

$$R_1 = -\frac{\partial \tau_{ij}^{LS}}{\partial x_i}, \quad R_2 + R_3 = -\frac{\partial H_{ij}^{LS}}{\partial x_i}, \quad R_4 = -\frac{\partial \sigma_{ij}^{LS}}{\partial x_i}. \tag{7.10}$$

where the subgrid stress tensor (with superscript LS referring to the LES approach) $\tau_{ij}^{LS} = (\rho u_i u_j)^{LS} - (\rho u_i)^{LS} u_j^{LS}$ is modeled by

$$\tau_{ij}^{LS} == -2\nu_t(\overline{S}_{ij} - \frac{\delta_{ij}}{3}\overline{S}_{kk}) \tag{7.11}$$

where $\overline{S}_{ij} = \frac{1}{2}(\frac{\partial \overline{u}_i}{\partial x_j} + \frac{\partial \overline{u}_j}{\partial x_i})$ is the resolved strain rate.

The subgrid eddy viscosity ν_t can be determined by using the k-equation model. This model is based on isotropy at the subgrid scales and tracks the subgrid kinetic energy on the subgrid scales by introducing a new transport equation for the energy. From this model, eddy viscosity can be expressed as

$$\nu_t = C_\nu \overline{\Delta}(k^{sgs})^{1/2} \tag{7.12}$$

where C_ν is the model coefficient which can be evaluated based on the turbulence thoery as $C_\nu = 0.067$ or adjusted dynamically as part of the solution using a localized dynamic procedure for the subgrid kinetic energy (LDKM).

7.4 TLS Closure

Unlike the LES, where the closure employed is based on the definition of an eddy-viscosity, the TLS closure is based on direct simulation of the unresolved terms. The terms R_1, $R_2 + R_3$, and R_4 can be represented as the same form given in LES closure. The large scale stress tensor (with superscript L referring to the TLS approach) $\hat{\tau_{ij}}^L = (\rho u_i u_j)^L - (\rho u_i)^L u_j^L$ is written as

$$\hat{\tau_{ij}}^L = \Big[(\rho u_i)^L u_j^S + (\rho u_i)^S u_j^L + (\rho u_i)^S u_j^S\Big]^L. \tag{7.13}$$

Similarly large scale enthalpy flux $\hat{H_i}^L$ and large scale viscous work $\hat{\sigma_i}^L$ can be defined as follows

$$\begin{aligned}
\hat{H_i}^L &= \Big[(\rho E) u_i\Big]^L - \Big[(\rho E)^L u_i^L\Big]^L + \Big[(p u_i) - (p^L u_i^L)\Big]^L \\
&= \Big[(\rho E)^L u_i^S + (\rho E)^S u_i^L + (\rho E)^S u_i^S\Big]^L + \Big[p^L u_i^S + p^S u_i^L + p^S u_i^S\Big]^L \\
\hat{\sigma_i}^L &= (\tau_{ij} u_j)^L - (\tau_{ij}^L u_j^L)^L \\
&= \Big[\tau_{ij}^L u_j^S + \tau_{ij}^S u_j^L + \tau_{ij}^S u_j^S\Big]^L
\end{aligned} \tag{7.14}$$

Here, the small scales are obtained by solving the small scale equations which are defined as follows:

$$\begin{aligned}
\frac{\partial \rho^S}{\partial t} + \frac{\partial}{\partial x_i}(\rho u_i)^S &= 0 \\
\frac{\partial}{\partial t}(\rho u_i)^S + \frac{\partial}{\partial x_j}\Big[\Big((\rho u_i)^L + (\rho u_i^S)\Big)(u_j^L + u_j^S)\Big]^S &= -\frac{\partial p^S}{\partial x_i} + \frac{\partial \tau_{ij}^S}{\partial x_j} \\
\frac{\partial}{\partial t}(\rho E)^S + \frac{\partial}{\partial x_i}\Big[\Big((\rho E)^L + (\rho E)^S\Big)(u_i^L + u_i^S)\Big]^S &= -\Big[\frac{\partial}{\partial x_i}(p^L + p^S)(u_i^L + u_i^S)\Big]^S \\
-\frac{\partial q_i^S}{\partial x_i} + \Big[\frac{\partial}{\partial x_i}(\tau_{ij}^L + \tau_{ij}^S)(u_j^L + u_j^S)\Big]^S.
\end{aligned} \tag{7.15}$$

7.5 TLS-LES Coupling

In the hybrid TLS-LES approach, the TLS equations are used in the high-gradient near-wall region, while standard LES equations are use in the outer flow region. One of the advantage of such hybrid TLS-LES approach is no need for interface boundary conditions for the LS velocity field. Note that, while all zonal approaches (RANS-LES) use some form of domain decomposition, in TLS-LES functional decomposition is introduced according to the Eqn 7.3. Since the represented resolved motion equations have the same functional form for TLS and LES, the implentation of hybrid TLS-LES approach is easy to achieve by switching from the explicit SS reconstruction to subgrid stress closure in the outer layer.

However, it is important to note that this functional decomposition raises a question which needs to be adressed. The end points of the wall-normal lines are lying

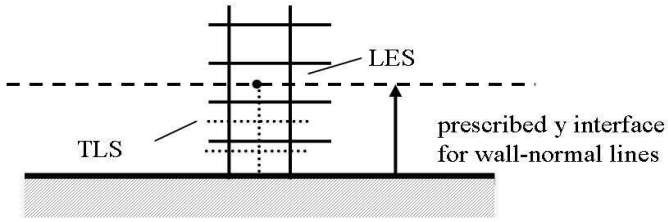

Figure 7.1: Illustration of Near-wall TLS-LES model.

inside the flow domain where the SS boundary conditions are not known. It is expected that the reconstructed SS velocity field would be rather insensitive to the boundary conditions at the interior endpoint since it is mostly defined by the LS velocity gradients. However further analysis is needed. For this purpose, we propose two different boundary conditions. The first one is a zero gradient boundary condition for the small scale velocities and the second one is the direct calculation of the small scale velocities in terms of the local subgrid kinetic energy k^{sgs} (obtained from the K-eqn). This approach assumes that small scales are isotropic at the edge of the inner region.

Boundary conditions at $y = 0$:

$u_i^s = 0$, $i = 1, 2, 3$

and at $y = Y$:

Zero gradient boundary condition

$$\partial u_i^s / \partial y = 0, \qquad i = 1, 2, 3$$

or fluctuating boundary condition

$$u_i^s = \sqrt{\tfrac{2}{3} k^{sgs}} W_i, \qquad i = 1, 2, 3$$

where W_i is a random number with zero mean.

The wall-normal TLS lines can also be extended to another LES cell to improve the boundary condition for the small scale equation in the overlapping region.

CHAPTER VIII

APPLICATION OF HYBRID TLS-LES TO WALL-BOUNDED FLOWS

8.1 Turbulent Channel Flow

The fully developed channel flow has been widely studied in the past, and both experimental and DNS data are available for comparison purposes. Pure TLS results of Kemenov and Menon [26, 104] show the capability of the model for capturing the near-wall flow energetics of 3D turbulent flow. Here, the results based on the new hybrid TLS-LES approach are presented.

The fully developed channel flow of width $2h$, where h is the channel half-width, is simulated by applying periodic boundary conditions in the streamwise and spanwise directions and no-slip conditions in the cross-stream direction. Calculations are performed for Reynolds numbers based on friction velocities of 590, 1200 and 2400. Near-wall TLS-LES results for statistically steady flow are compared to Moser's[89] DNS data for $Re_\tau = 590$ and Wei's [105] experimental data for $Re_\tau = 1200$. Here $Re_\tau = u_\tau h/\nu$, where $u_\tau = \sqrt{\nu du/dy|_{y=0}}$ is the friction velocity.

The computational domain is discretized by $32 \times 40 \times 32$ LS grid cells for $Re_\tau = 590$ and $Re_\tau = 1200$ with uniform grid in the periodic directions (streamwise and spanwise) and nominal stretched grid in the wall normal direction. As the Reynolds number increases, only a smaller portion of kinetic energy can be captured on the LS grid. Thus, for the high Reynolds number ($Re_\tau = 2400$) case, the resolution was increased to $64 \times 50 \times 64$. In all cases, a uniform grid of 8 SS cells per LS cell is used in the periodic directions. A variable grid ranging from 12 near the wall to 10 in the last LS cell is used in the wall normal direction. The near-wall region for TLS-LES are represented by three LS cells extending up to $y^+ \approx 50$ ($y^+ = yu_\tau/\nu$). The near-wall SS grid spacing is kept approximately $y^+ \approx 1$. The standard LES with dynamic Germano subgrid model is used in the outer region. The simulation parameters and the mean flow variables are given in Table 8.1.

Table 8.1: Simulation parameters and mean flow variables for TLS-LES channel flow simulations

	Grid	Re_τ	$\triangle y^{+SS}$	$\triangle y^{+LS}$	C_f
DNS[89]	$384 \times 257 \times 384$	590		0.042	$5.76\text{x}10^{-3}$
TLS-LES	$32 \times 40 \times 32$	590	1.067	9.395	$5.66\text{x}10^{-3}$
TLS-LES	$32 \times 40 \times 32$	1200	1.320	15.861	$4.58\text{x}10^{-3}$
TLS-LES	$64 \times 50 \times 64$	2400	1.436	17.041	$3.89\text{x}10^{-3}$

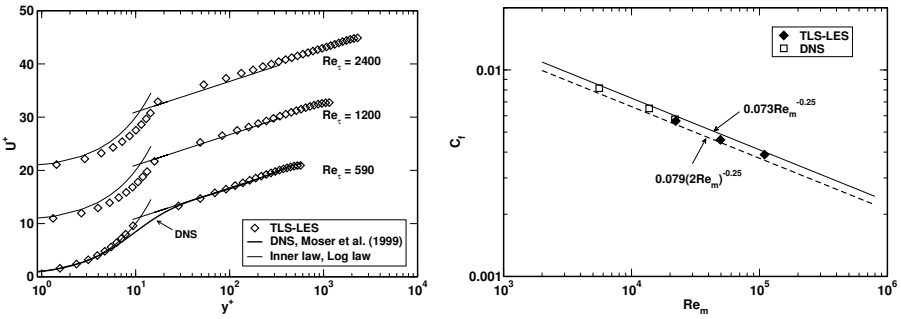

(a) Mean velocity $\langle U^+ \rangle$ (b) Friction coefficient C_f

Figure 8.1: Near-wall TLS-LES mean quantities.

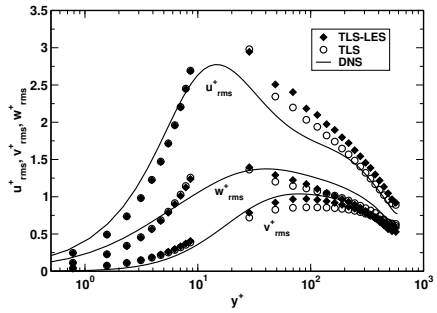

Figure 8.2: RMS velocity fluctuation profiles for $Re_\tau = 590$ computed from TLS-LES, pure TLS and DNS[89].

Figure 8.1 (a) presents the near-wall TLS-LES results for the mean velocity profiles over the Reynolds-number range indicated in Table 8.1. For $Re_\tau = 590$ the DNS data of Moser [89] is used for direct comparison. For all cases, the inner law $u^+ = y^+$, and log law, $u^+ = 2.44lny^+ + 5.2$, are also plotted for comparison. Near-wall TLS-LES model predicts slightly higher values in the buffer region ($10 < y^+ < 30$) for $Re_\tau = 590$ which might be caused by the coarse LS grid (which was chosen deliberately as a worst case scenario). The overall mean velocities are predicted quite well with the near-wall TLS-LES model. At all Reynolds numbers, the physically realistic viscous sublayer is captured reasonably well.

Figure 8.1 (b) shows the computed skin friction coefficients compared with the DNS data of Moser[89] and the turbulent correlation of Dean [106]. The Reynolds number used in this plot is based on the bulk velocity and the channel width, and the friction coefficient is defined as $C_f = 2(u_\tau/U_{ref})^2$. Good agreement is obtained with the DNS C_f value at $Re_\tau = 590$. Overall, the friction coefficient demonstrates the right trend.

Figures 8.2 and 8.3 show the rms velocity fluctuations predicted by the near-wall TLS-LES model. In Fig. 8.2 near-wall TLS-LES computed rms velocity fluctuation

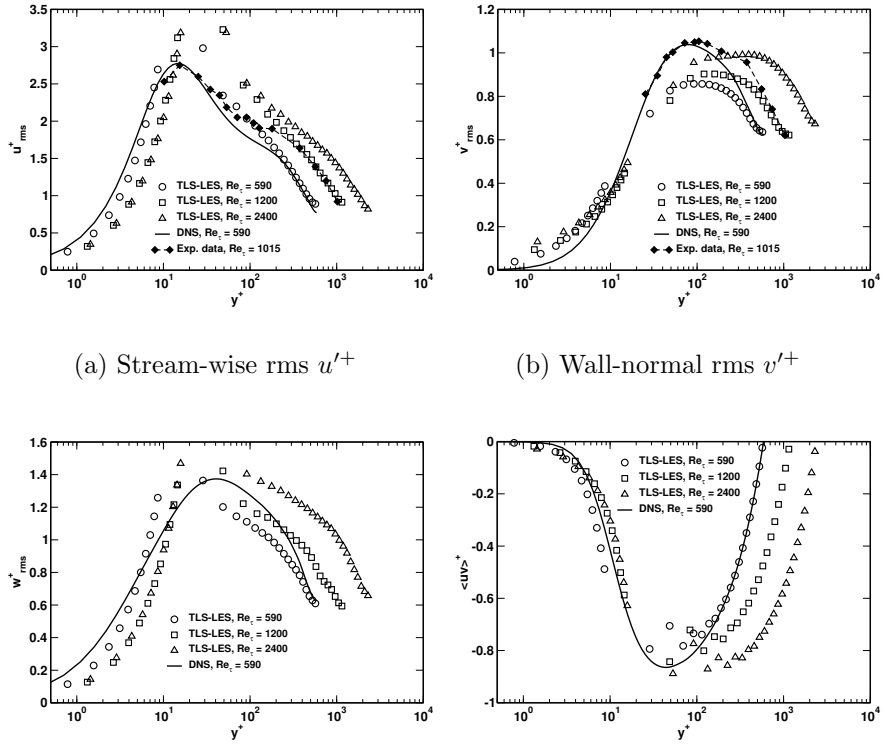

(a) Stream-wise rms u'^{+}

(b) Wall-normal rms v'^{+}

(c) Span-wise rms w'^{+}

(d) Reynolds stress

Figure 8.3: Near-wall TLS-LES rms quantities.

profiles for $Re_\tau = 590$ are compared with the DNS calculations of Moser [89] and results obtained by pure TLS calculations. TLS based models (pure TLS and near-wall TLS-LES) correctly predict the location and the peak value of the streamwise rms-velocity fluctuation for $Re_\tau = 590$, but produce a broader profile. However, the near-wall TLS-LES model underpredicts the rms-velocity fluctuations compared to the pure TLS result in the bulk flow. This is due to the highly dissipative behavior of the Germano model[107], which is used for the LES bulk flow computations. The effect of SGS model for outer flow will be investigated by using the one-equation model for the subgrid kinetic energy [108] later.

In Fig. 8.3, near-wall TLS-LES results for rms-velocity fluctuations are compared to the DNS result of Moser [89] and the data of Wei [105]. For two high Reynolds cases u^+_{rms} lead to very similar results, demonstrating universality of flow properties close to the wall at high Reynolds numbers.

Figures 8.4 (a), (b) and (c) show instantaneous streamwise energy spectra. 1D-line and plane-averaged spectra are plotted and compared to the slope of $k^{-5/3}$. It can be seen that the near-wall TLS-LES approach recovers both LS and SS spectras. Finally, high and low-speed streaks, shown in Fig. 8.4 (d) for $Re_\tau = 2400$ for near-wall TLS-LES case, exhibit a typical near-wall pattern.

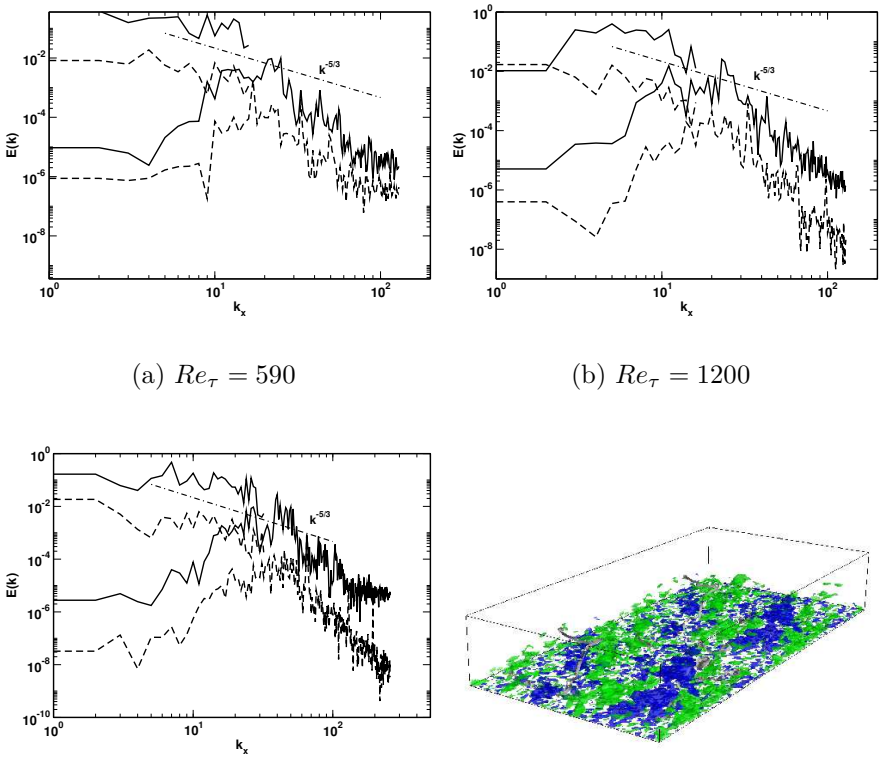

(a) $Re_\tau = 590$ (b) $Re_\tau = 1200$

(c) $Re_\tau = 2400$ (d) $Re_\tau = 2400$

Figure 8.4: Near-wall TLS-LES calculations: (a-c) Instantaneous (solid lines) and volume averaged (dashed lines) stream-wise spectra; (d) Isosurfaces of the streamwise velocity fluctuations: $u' = +3$ (blue) and $u' = -3$ (green).

Overall trend of the hybrid TLS-LES results show the capabilities of the model for near-wall applications using relatively coarse grids.

8.2 Three-dimensional Bump Flow

To show the capability of the hybrid TLS-LES model for complex geometries, a three-dimensional boundary layer flow, investigated experimentally by Simpson *et al.* [33], is chosen. This flow involves three-dimensional unsteady separation and reattachment. High Reynolds number of this types of flows are of considerable interest because of their relevance to practical flows. In one of the recent study [34], LES with the LDKM subgrid model have been applied to the same flow and complex flow pattern was predicted quite well. In this study, LES using LDKM subgrid model is revisited for completeness. Then, this flow is simulated with the hybrid near-wall TLS-LES model. The preliminary results are compared with Simpson *et al.*'s [33] experimental data.

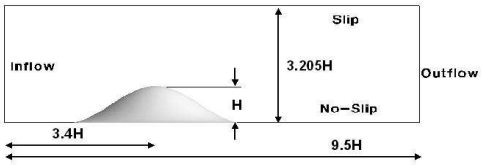

Figure 8.5: Geometry.

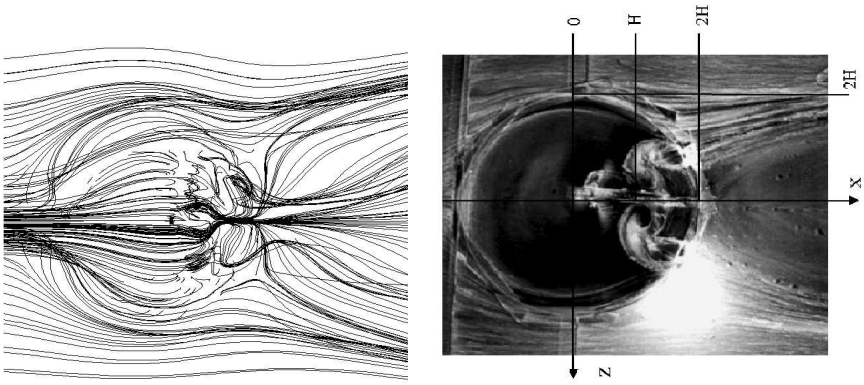

(a) Predicted with near-wall TLS-LES

(b) Experiments

Figure 8.6: Oil-flow visualizations and instantaneous streamlines in the near-wall region.

Figure 8.5 presents the geometry of the configuration in the streamwise and wall-normal directions. The hill height is $H = 0.078m$ with the circular base of radius $R = 2H$. The zenith of the hill is about $3.4H$ downstream from the inflow boundary. The computational domain extends $10.0H$ in the spanwise and $9.5H$ in the streamwise direction. The shape of the hill is defined as $y(r)/H = -1/6.04844[J_o(\Lambda)I_o(\Lambda r/R) - I_o(\Lambda)J_o(\Lambda r/R)]$ where $\Lambda = 3.1926$, J_o and I_o are the Bessel and modified Bessel function of the first kind, respectively. The Reynolds number based on height H and inflow velocity (U_{ref}=27.5 m/s), is approximately 130,000.

The computational domain is discretized with $192 \times 184 \times 144$ grid points, with a small stretching in the wall normal region and on the lee-side of the hill for LES-LDKM case. For this grid the minimum grid resolution in the wall-normal direction is about $y = 56\mu m$. The minumum grid resolution is estimated as (Δx^+, Δy^+, Δz^+) = (100, 4, 120) in terms of viscous wall units. For near-wall TLS-LES case, relatively coarse grid compared to full LES case is used. The computational domain is discretized by $48 \times 46 \times 36$ LS grid cells. The SS resolution for streamwise lines is 385, for spanwise lines 289 and for wall normal lines 51. The near-wall region for bottom wall is represented by five LS cells extending up to $y^+ \approx 40$. The near-wall grid spacing for LS is $y = 188\mu m$ and for SS is $y = 15.6\mu m$ in the wall-normal direction.

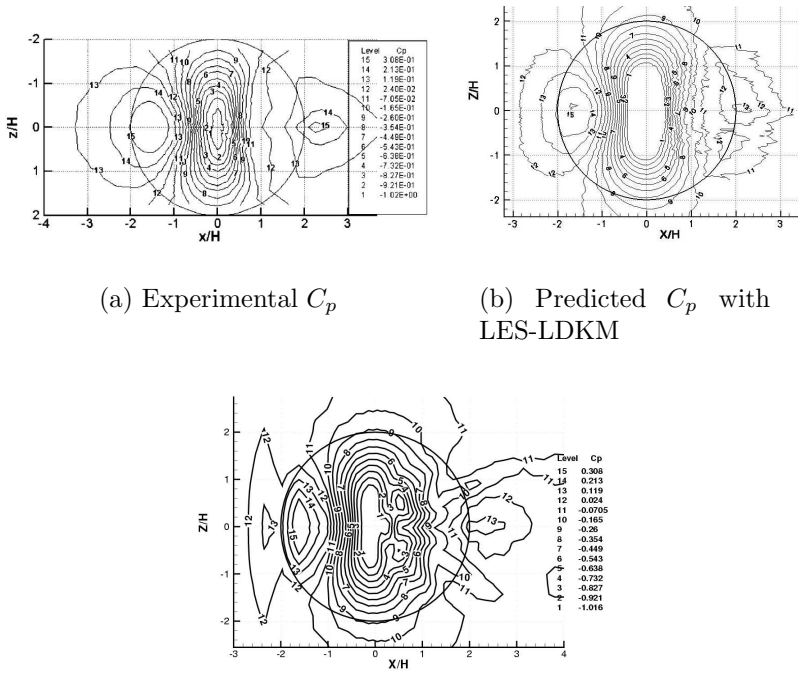

(a) Experimental C_p

(b) Predicted C_p with LES-LDKM

(c) Predicted C_p with near-wall TLS-LES

Figure 8.7: Static-pressure coefficient contours over the hill surface.

At the lower wall, no-slip conditions are enforced for velocity, whereas at the upper wall, slip boundary conditions are enforced. At the outlet, characteristic boundary conditions are applied to all variables. For near-wall TLS-LES case, initial LS velocity field was determined from the full LES-LDKM flow field.

Figure 8.6 presents a comparison of the predicted surface streamline pattern with the experimental oil-flow pattern. Based on surface streamline patterns, the flow on the lee side of the bump is very complex and shows 3D separation and reattachment because of both streamwise and spanwise pressure gradients on the lee side. Qualitative agreement is found between the near-wall TLS-LES results and experimental oil flow visualization.

Figure 8.7 presents the computed surface distribution of static pressure coefficients (C_p) and the corresponding experimental result. There is a good similarity in both features and magnitudes between the LES-LDKM computation and the experimental data. In the spanwise direction, both LES-LDKM and experiments show a symmetric pressure distribution.Figure 8.7 (c) presents the near-wall TLS-LES model results for the pressure coefficient. It is clear from this figure that the near-wall TLS-LES is capable of predicting approximately the correct pressure distribution around the bump. There are some discrepancies in the lee side where the flow is separating which will be adressed in the future. Both results show that as the boundary layer

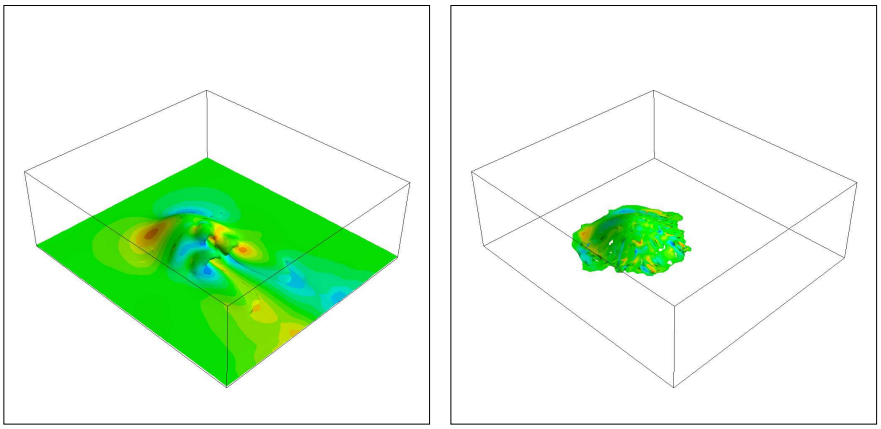

(a) LS (b) Resolved SS

Figure 8.8: Instantaneous LS (a) and resolved SS (b) vorticity magnitude isosurfaces predicted with near-wall TLS-LES model. Isosurfaces are colored with local spanwise velocity.

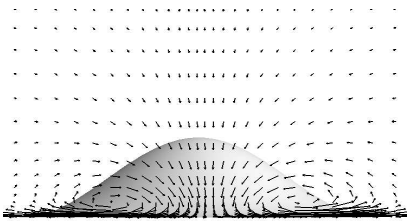

Figure 8.9: Secondary flow vector field predicted with near-wall TLS-LES model.

approaches the leading edge of the hill the pressure increases. The pressure then decreases at the zenith of the hill as the flow accelerates over the hill. The position of minumum pressure is predicted accurately by all (LES-LDKM and near-wall TLS-LES) simulations. Snapshots of the LS and SS vorticity magnitude isosurfaces at a level of $|\overline{w}^L| = 1100$ and $|\overline{w}^S| = 300$ are shown in Fig. 8.8. Isosurfaces are colored with local spanwise velocity. It is seen that the simulated SS field responds to the LS field by creating fine scale SS field at the high gradient LS regions.

Wake measurements are performed at $3.69H$ downstream of the zenith hill, where the flow has reattached on the wall and turbulent boundary layer has reformed. Figure 8.9 shows the instantaneous secondary flow vector field predicted with near-wall TLS-LES model at $x/H = 3.69$ plane. The presence of streamwise counter-rotating vortex pair, located at $y/H = 0.2$, is observed, which is consistent with the observations of Perrson *et al.*[109]. Figure 8.10 presents a comparison for time-averaged streamwise and spanwise velocities at $3.69H$ for various spanwise locations. LES-LDKM and near-wall TLS-LES results are compared with the experimental data.

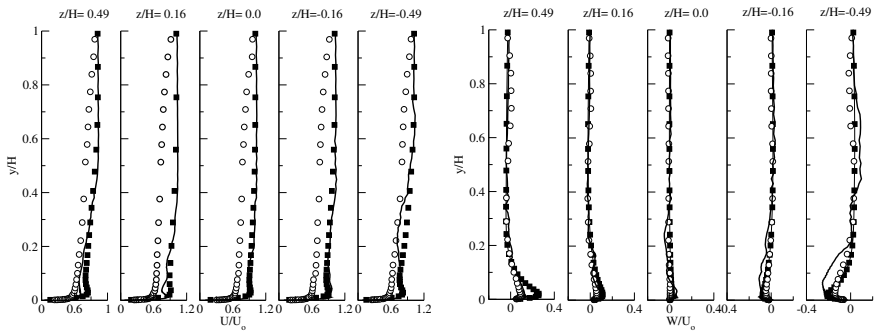

(a) U/U_{ref} (b) W/U_{ref}

Figure 8.10: Mean flow quantities predicted by LES-LDKM (solid lines) and near-wall TLS-LES model (square symbols).

All models overpredict the streamwise velocity, which can be related to the coarser spatial resolution used away from the wall. However, cross-stream velocity profiles are well predicted with both models as shown in Fig. 8.10 (b). From Fig. 8.10, overall agreement between predictions and experiments is reasonable.

Current results show the capability of LES, using LDKM subgrid model, for complex flows. The near-wall TLS-LES of this flow shows qualitative agreement with the experimental and LES results. Overall results looks reasonable for this kind of coarse resolution. A finer resolution is expected to provide better results and will be adressed in the near future.

CHAPTER IX

CONCLUSION

A novel Two Level Simulation approach, which is alternative to traditional LES, has been developed based on the explicit simulation of the SS velocity fields. A coupled system of the LS and the SS governing equations, that is not based on an eddy-viscosity type of assumptions and requires no adjustable parameters, has been derived based on the decomposition of flow fields into the LS and the SS components. To alleviate complexity of numerical simulation, the SS equation has been treated on a domain with a reduced dimension and representing a collection of 1D lines.

First, the exact SS equation has been studied by simulating randomly forced Burgers turbulence with primary reason for validating the ability to reconstruct the SS fields as well as the adopted numerical approach. Reconstruction of the SS field in 3D requires some modeling since the SS derivatives in the directions transverse to the line direction are not available. To validate the model assumptions statistical analysis of the SS derivatives has been performed based on DNS data sets including both homogeneous and non-homogeneous turbulent cases. It has been shown that the resulting simplified SS velocity equation is able to reconstruct the SS velocity based on the LS velocity field only, without invoking the eddy-viscosity hypothesis or using modeling constants.

Fully coupled implementation of TLS has been demonstrated by simulating several benchmarks cases of incompressible turbulent flows, including forced isotropic turbulence, well-developed turbulent channel flow and temporal mixing layers. The current approach is readily extendable to treat high-Re number non-homogeneous turbulent flows. *A priori* analysis of the SS derivatives for a high-Re turbulent channel DNS data shows strong similarity with the SS derivatives of the homogeneous and isotropic turbulence. This provides a certain level of justification to use the modeled SS equation for non-homogeneous turbulent flows.

Overall, the presented results suggest that TLS approach has a potential for capturing high-Re number turbulent flow behavior using rather coarse grids by explicitly simulating the SS fields. More importantly, TLS formulation provides a useful framework for treating complex turbulent flows by not resorting to the concept of the filtering. It provides a different perspective on turbulence modeling and offers certain potential advantages over existing LES approach, namely:

- TLS provides consistent computational framework to simulate both the large-scale and small-scale fields;
- TLS coupled system of large and small-scale equations does not involve any of eddy-viscosity type of assumptions and requires no adjustable model constants;

- TLS can be readily extended to non-homogeneous flows in complex geometries. Since the filtering is avoided, there is no commutativity restriction which formally requires adding to LES equations, and modeling extra terms when a non-homogeneous filter is present;

- The small-scale field reconstruction can be very effective on massively parallel computers making TLS approach computationally feasible for high-Re flow simulations.

A novel approach to simulate the high-Re number flows has been developed based on coupling the TLS equations near the wall with a more conventional LES approach in the far field. A coupled system of TLS and LES equations are implemented to simulate wall-bounded flows. Results for turbulent channel flow and three-dimensional separating- reattaching flow suggest that the hybrid TLS-LES approach has the potential for capturing the near-wall dynamics by using very coarse grids.

CHAPTER X

FUTURE WORK

In this concluding section, it is worth to outline several possible venues of continuation of the work presented in this report.

In the hybrid TLS-LES approach, since the endpoints of wall-normal lines are lying inside the flow domain, the SS boundary conditions are not known there. It is expected that the reconstructed SS velocity field would be rather insensitive to the boundary condition at the interior endpoint since it is mostly define by the LS velocity gradients, however further testing is needed. Also, it is important to estimate how coarse the LS resolution can be in wall normal direction to sustain the acceptable level of fluctuations in the SS velocity. In the test case studied in Section 6.3, the first LS grid point was at $x_3^+ = 19$ at $Re_\tau = 590$. Clearly, the coarsening of the LS grid may diminish the LS gradients which can adversely affect the reconstructed SS field. This work is currently underway and will be reported in the future.

The other area which is worth to explore in the context of TLS approach is how line placing affect the simulated SS fields. It is clear that "unstructured" line placing may increase computational effectiveness of the approach due to a possible reduction of the total number of lines needed to represent the SS velocity field. In principle, computational efficiency of the mixed TLS/LES approach can be achieved in TLS also, by clustering lines (for example, randomly) in the near-wall region and using fewer lines in the channel core. As a result, the physical consequences of the model assumptions (i) and (ii) have to be studied for a case of the arbitrarily positioned line l_k.

An extension of TLS approach to treat compressible flows as well as turbulent mixing and related combustion problems requires the introduction of additional field equations that describe evolution of density, species concentration and internal energy. Consequently, decomposition similar to Eq. (4.3) can be introduced to additional flow variables as well. As a first step of generalization of the proposed approach in this direction turbulent passively advected scalars can be studied. This, however, would require some additional model assumption relating the SS scalar dissipation and advection in directions orthogonal to line l_k. In principle, a physical insight of such SS scalar field behavior can be obtained from *a priori* analysis of the corresponding DNS data sets. Such work is currently underway and will be reported in the near-future.

CHAPTER XI

LIST OF PAPERS

This report is based on the following papers:

1. K. Kemenov, A.G. Gungor and S. Menon. Two level simulation of high-Re wall-bounded fLows and isotropic turbulence. *AIAA paper 2005-5318* , 2005.

2. A.G. Gungor and S. Menon. Direct simulation of subgrid turbulence in high-Re, wall-bounded flows. *AIAA paper 2006-3538*, 2006.

3. K. Kemenov and S. Menon. Explicit small-scale velocity simulation for high-Re turbulent flows. *Journal of Computational Physics*, 220:290–311, 2006.

4. K. Kemenov and S. Menon. Explicit small-scale velocity simulation for high-Re turbulent flows. Part II: Non-homogeneous flows *Journal of Computational Physics*, 222:673–701, 2007.

Bibliography

[1] P. A. Davidson. *Turbulence: An Introduction for Scientists and Engineers.* Oxford University Press, 2004.

[2] S. A. Orszag and G. S. Patterson, Jr. Numerical Simulation of Three-Dimensional Homogeneous Isotropic Turbulence. *Phys. Rev. Lett.*, 28:76–79, 1972.

[3] Y. Kaneda, T. Ishihara, M. Yokokawa, K. Itakura, and A. Uno. Energy dissipation rate and energy spectrum in high resolution direct numerical simulation of turbulence in a periodic box. *Physics of Fluids*, 15(2):L21–L24, 2003.

[4] H. Abe, H. Kawamura, and Y. Matsuo. Surface heat-flux fluctuations in a turbulent channel flow up to $Re_\tau = 1020$ with $Pr = 0.025$ and 0.71. *International Journal of Heat and Fluid Flow*, 25:404–419, 2004.

[5] M. Tanahashi, S.-J. Kang, T. Miyamoto, S. Shiokawa, and T. Miyauchi. Scaling law of fine scale eddies in turbulent channel flows up to $Re_\tau = 800$. *International Journal of Heat and Fluid Flow*, 25:331–340, 2004.

[6] U. Piomelli. Large-Eddy Simulation: achievements and challenges. *Progress in Aerospace Science*, 35:335–362, 1999.

[7] C. Meneveau and J. Katz. Scale-Invariance and Turbulence Models for Large-Eddy Simulation. *Annual Review of Fluid Mechanics*, 32:1–32, 2000.

[8] C. G. Speziale. Turbulence modeling for time-dependent RANS and VLES - A review. *AIAA Journal*, 36(2):173–184, 1998.

[9] J. A. Domaradzki and E. M. Saiki. A subgrid-scale model based on the estimation of unresolved scales of turbulence. *Physics of Fluids*, 9:2148–2164, 1997.

[10] S. Ghosal. Mathematical and physical constraints on large eddy simulation of turbulence. *AIAA Journal*, 37:425–433, 1999.

[11] C. Fureby and G. Tabor. Mathematical and Physical Constraints on Large-Eddy Simulations. *Theoretical and Computational Fluid Dynamics*, 9:85–102, 1997.

[12] G. S. Winckelmans, H. Jeanmart, and D. Carati. On the comparison of turbulence intensities from large-eddy simulation with those from experiment or direct numerical simulation. *Physics of Fluids*, 14(5):1809–1811, 2002.

[13] S. B. Pope. Ten questions concerning the large-eddy simulation of turbulent flows. *New Journal of Physics*, 6:35, 2004.

[14] R. S. Rogallo and P. Moin. Numerical Simulation of Turbulent Flows. *Annual Review of Fluid Mechanics*, 16:99–137, 1984.

[15] D. Carati, G. S. Winckelmans, and H. Jeanmart. On the modelling of the subgrid-scale and filtered-scale stress tensors in large-eddy simulation. *Journal of Fluid Mechanics*, 441:119–138, 2001.

[16] B. J. Geurts and A. Leonard. "Is LES ready for complex flows ?". In *Closure Strategies for Turbulent and Transitional Flows*. Cambridge University Press, 2002.

[17] T. S. Lund. The use of explicit filters in large eddy simulation. *Computers & Mathematics with Applications*, 46:603–616, 2003.

[18] G. De Stefano and O. V. Vasilyev. "Perfect" modeling framework for dynamic SGS model testing in large eddy simulation. *Theoretical and Computational Fluid Dynamics*, 18(1):27–41, 2004.

[19] Yu. V. Egorov and M. A. Shubin. *Foundations of the classical theory of partial differential equations*. Springer, 1998.

[20] O. V. Vasilyev, T. S. Lund, and P. Moin. A General Class of Commutative Filters for LES in Complex Geometries. *Journal of Computational Physics*, 146(1):82–104, 1998.

[21] S. Ghosal and P. Moin. The Basic Equations for the Large Eddy Simulation of Turbulent Flows in Complex Geometry. *Journal of Computational Physics*, 118(1):24–37, 1995.

[22] H. van der Ven. A family of large eddy simulation (LES) filters with nonuniform filter width. *Physics of Fluids*, 7(5):1171–1172, 1995.

[23] A. Marsden, O. Vasilyev, and P. Moin. Construction of Commutative Filters for LES on Unstructured Meshes. *Journal of Computational Physics*, 175:584–603, 2002.

[24] F. van der Bos and B. J. Geurts. Commutator errors in the filtering approach to large-eddy simulation. *Physics of Fluids*, 17:035108–20, 2005.

[25] D. R. Chapman. Computational aerodynamics, development and outlook. *AIAA Journal*, 17:1293–1313, 1979.

[26] K. Kemenov and S. Menon. A two-level simulation methodology for les of high reynolds number flows. In *Advances in Turbulence IX*, pages 203–206. CIMNE, 2002.

[27] K. Kemenov and S. Menon. Two Level Simulation of High-Re Turbulent Flows. In *Direct and Large-Eddy Simulation V, Proceedings of the fifth international ERCOFTAC workshop, Ercoftac Series*, volume 9, pages 49–56. Kluwer, 2004.

[28] K. Kemenov and S. Menon. Explicit small-scale velocity simulation for high-re turbulent flows. *Journal of Computational Physics*, 220:290–311, 2006.

[29] K. Kemenov and S. Menon. Explicit small-scale velocity simulation for high-re turbulent flows. part 2: Non-homogeneous flows. *Journal of Computational Physics*, 222:673–701, 2007.

[30] C. Fureby, N. Alin, N. Wikstrom, S. Menon, N. Svanstedt, and L. Persson. Large-eddy simulation of high-Reynolds-number wall-bounded flows. *AIAA Journal*, 42:457–468, 2004.

[31] K. Kemenov, A.G. Gungor, and S. Menon. Two level simulation of high-re wall bounded flows and isotropic turbulence. *AIAA paper 2005-5318*, 2005.

[32] A. G. Gungor and S. Menon. Direct simulation of subgrid turbulence in high-re, wall-bounded flows. *AIAA paper 2006-3538*, 2006.

[33] R. Simpson, C. Long, and G. Byun. Study of vortical separation from an axisymmetric hill. *International Journal of Heat and Fluid Flow*, 23:582–591, 2002.

[34] N. Patel and S. Menon. Large-eddy simulations of turbulent flow over an axisymmetric bump. *AIAA paper 2003-0967*, 2003.

[35] E.C. Hylin and J.M. McDonough. Chaotic small-scale velocity fields as prospective models for unresolved turbulence in an additive decomposition of the Navier-Stokes equation . *International Journal of Fluid Mechanics Research*, 26:539–567, 1999.

[36] T. Dubois, F. Jauberteau, and R. Temam. Incremental unknowns, multilevel methods and the numerical simulation of turbulence. *Computer Methods in Applied Mechanics and Engineering*, 159(2):123–189, 1998.

[37] T. Dubois and F. Jauberteau. A Dynamic Multilevel Model for the Simulation of the Small Structures in Homogeneous Isotropic Turbulence. *Journal of Scientific Computing*, 13(3):323–367, 1998.

[38] T. Dubois, F. Jauberteau, and R. Temam. *Dynamic multilevel methods and the numerical simulation of turbulence*. Cambridge University Press, 1999.

[39] T.J.R. Hughes, L. Mazzei, and K.E. Jansen. The large eddy simulation and variational multiscale method. *Computing and Visualization in Science*, 3:47–59, 2000.

[40] T.J.R Hughes, L. Mazzei, and A.A. Oberai. The multiscale formulation of Large-eddy simulation: Decay of homogeneous isotropic turbulence. *Physics of Fluids*, 13(2):505–512, 2001.

[41] T.J.R Hughes, A.A. Oberai, and L. Mazzei. Large eddy simulation of turbulent channel flows by variational multiscale method. *Physics of Fluids*, 13(6):1784–1799, 2001.

[42] J.-P. Laval, B. Dubrulle, and S. Nazarenko. Nonlocality of interaction of scales in the dynamics of 2D incompressible fluids. *Physical Review Letters*, 83(20):4061–4064, 1999.

[43] J.-P. Laval, B. Dubrulle, and S. Nazarenko. Nonlocality and intermittency in three-dimensional turbulence. *Physics of Fluids*, 13(7):1995–2012, 2001.

[44] B. Dubrulle, J.-P. Laval, S. Nazarenko, and N.K.-R. Kevlahan. A dynamic subfilter-scale model for plane parallel flows. *Physics of Fluids*, 13(7):2045–2064, 2001.

[45] J.-P. Laval, B. Dubrulle, and S. Nazarenko. Fast numerical simulations of 2D turbulence using a dynamic model for subfilter motions. *Journal of Computational Physics*, 196(1):184–207, 2004.

[46] C. Foias, O. Manley, and R. Temam. Modeling on the interaction of small and large eddies in two-dimensional turbulent flows. *Mathematical Modeling and Numerical Analysis*, 22:93–114, 1988.

[47] C. Foias, O. Manley, and R. Temam. Approximate inertial manifolds and effective viscosity in turbulent flows. *Physics of Fluids A*, 3(5):898–911, 1991.

[48] O. Manley, R. Temam, and W. Shouhong. Inertial manifolds, partially space-averaged equations, and the separation of scales in turbulent flows. *Physics of Fluids*, 7:1791–1793, 1995.

[49] F. Bouchon and F. Jauberteau. A multilevel method applied in the nonhomogeneous direction of the channel flow problem. *Applied Numerical Mathematics*, 36:1–34, 2001.

[50] S. S. Collis. Monitoring unresolved scales in multiscale turbulence modeling. *Physics of Fluids*, 13(6):1800–1806, 2001.

[51] B. Knaepen, O. Debliquy, and D. Carati. Large-eddy simulation without filter. *Journal of Computational Physics*, 205(1):98–107, 2005.

[52] P. K. Yeung and Y. Zhou. On the universality of the Kolmogorov constant in numerical simulations of turbulence. *Physical Review E*, 56:1746–1752, 1997.

[53] J.-L. Guermond, J. T. Oden, and S. Prudhomme. Mathematical Perspective on Large Eddy Simulation Models for Turbulent Flows. *Journal of Mathematical Fluid Mechanics*, 6:195–248, 2004.

[54] U. Piomelli and E. Balaras. Wall layer models for large eddy simulation. *Annual Review of Fluid Mechanics*, 34:349–374, 2002.

[55] H. Abe, H. Kawamura, and Y. Matsuo. Direct Numerical Simulation of a Fully Developed Turbulent Channel Flow With Respect to the Reynolds Number Dependence. *ASME Journal of Fluids Engineering*, 123:382–393, 2001.

[56] C. Beck. Superstatistics in hydrodynamic turbulence. *Physica D*, 193:195–207, 2004.

[57] S. Kline, W. Reynolds, F. Schraub, and P. Rundstadler. The structure of turbulent boundary layers. *Journal of Fluid Mechanics*, 30:741–773, 1967.

[58] R. L. Panton. Overview of the self-sustaining mechanisms of wall turbulence. *Progress in Aerospace Science*, 37:341–383, 2001.

[59] J. Jimenez, A. A. Wray, P. G. Saffman, and R. S. Rogallo. The structure of intense vorticity in isotropic turbulence. *Journal of Fluid Mechanics*, 255(4):65–90, 1993.

[60] F. Moisy and J. Jimenez. Geometry and clustering of intense structures in isotropic turbulence. *Journal of Fluid Mechanics*, 513:111–133, 2004.

[61] S. Kida. Vortical Structure of Turbulence. In *Mechanics for a New Millennium*, pages 445–456. Kluwer Academic Press, 2001.

[62] P. M. Gresho and R. L. Sani. *Incompressible flow and the finite element method* . John Wiley & Sons, 1998.

[63] M. Hafez. *Numerical simulation of incompressible flows*. World Scientific, 2002.

[64] T. Quartapelle. *Numerical Solution of the Incompressible Navier-Stokes Equations*. Birkauser, 1993.

[65] C. G. Speziale. On the advantages of the velocity-vorticity formulation of the equations of fluid dynamics. *Journal of Computational Physics*, 73(2):476–480, 1987.

[66] F. L. Ponta. The kinematic Laplacian equation method. *Journal of Computational Physics*, 207(2):476–480, 2005.

[67] C. Tenaud, S. Pellerin, A. Dulieu, and L. Ta Phuoc. Large Eddy Simulation of a spatially developing incompressible 3D mixing layer using $v - \omega$ formulation. *Computers & Fluids*, 34:67–96, 2005.

[68] A. J. Chorin. A numerical method for solving incompressible viscous flow problems. *Journal of Computational Physics*, 2:12–26, 1967.

[69] P. Tamamidis, G. Zhang, and D. N. Assanis. Comparisson of Pressure-Based and Artificially Compressibility Methods for Solving 3D Steady Incompressible Viscous Flows. *Journal of Computational Physics*, 124:1–13, 1996.

[70] F. H. Harlow and J. E. Welch. Numerical calculation of time-dependent viscous incompressible flow of fluid with free surface. *Physics of Fluids*, 8:2182–2189, 1965.

[71] S. V. Patankar. *Numerical heat transfer and fluid flow*. Hemisphere Publishing, 1980.

[72] D. Kwak, C. Kiris, and C. S. Kim. Computational challenges of viscous incompressible flows. *Computers & Fluids*, 34:283–299, 2005.

[73] A. J. Chorin. Numerical solutions of the Navier-Stokes equations. *Mathematics of Computation*, 22:745–762, 1968.

[74] R. Temam. Sur l'approximation de la solution des équations de Navier-Stokes par la méthode des fractionnarires. *Archive for Rational Mechanics and Analysis*, 33:377–385, 1969.

[75] W. E and J.-G. Liu. Projections Methods I: Convergence and Numerical Boundary Layers. *SIAM Journal on Numerical Analysis*, 32:1017–1057, 1995.

[76] J. Kim and P. Moin. Application of a fractional-step method to incompressible Navier-Stokes equations. *Journal of Computational Physics*, 59:308–323, 1985.

[77] S. A. Orszag, M. Israeli, and M. O. Deville. Boundary conditions for incompressible flows. *Journal of Scientific Computing*, 1:75–111, 1986.

[78] J. B. Bell, P. Colella, and H. M. Glaz. A second-order projection method for the incompressible Navier-Stokes equations. *Journal of Computational Physics*, 85:257–283, 1989.

[79] J. van Kan. A second-order accurate pressure-correction scheme for viscous incompressible flow. *SIAM Journal of on Scientific and Statistical Computing*, 7(3):870–891, 1986.

[80] W. E and J.-G. Liu. Projections Methods II: Godynov-Ryabenki Analysis. *SIAM Journal on Numerical Analysis*, 33:1597–1621, 1996.

[81] D. L. Brown, R. Cortez, and M. L. Minion. Accurate Projection Methods for the Incompressible Navier-Stokes Equations. *Journal of Computational Physics*, 168:464–499, 2001.

[82] P. M. Gresho and R. L. Sani. On pressure boundary condition for the incompressible Navier-Stokes equations. *International Journal for Numerical Methods in Fluids*, 7:1111–1145, 1987.

[83] J. H. Williamson. Low-storage Runge-Kutta schemes. *Journal of Computational Physics*, 35:48–56, 1980.

[84] A. Harten. High resolution schemes for hyperbolic conservation laws. *Journal of Computational Physics*, 49:357–393, 1983.

[85] H. Yu and Y.P. Liu. A Second Order Accurate, Component-Wise TVD Scheme for Nonlinear, Hyperbolic Conservation Laws. *Journal of Computational Physics*, 173:1–16, 2001.

[86] T. Gotoh and R. Kraichnan. Steady-state Burgers turbulence with large-scale forcing. *Physics of Fluids*, 10(11):2859–2866, 1998.

[87] V. Eswaran and S. B. Pope. An examination of forcing in direct numerical simulations of turbulence. *Computers and Fluids*, 16:257–278, 1988.

[88] C. Fureby, G. Tabor, H. G. Weller, and A. D. Gosman. A comparative study of subgrid scale models in homogeneous isotropic turbulence. *Physics of fluids*, 9:1416–1429, 1997.

[89] R. D. Moser, J. Kim, and N. N. Mansour. Direct numerical simulation of turbulent channel flow up to $Re_\tau = 590$. *Physics of Fluids*, 11:943–945, 1999.

[90] J. Zhou, R. J. Adrian, S. Balachandar, and T. M. Kendall. Mechanisms for generating coherent packets of hairpin vortices. *Journal of Fluid Mechanics*, 387:353–396, 1999.

[91] E. R. Corino and R. S. Brodkey. A visual investigation of the wall region in turbulent flow. *Journal of Fluid Mechanics*, 37:1–30, 1969.

[92] D. G. Bogard and W. G. Tiederman. Characteristics of ejections in turbulent channel flow. *Journal of Fluid Mechanics*, 179:1–19, 1987.

[93] A. Michalke. On the inviscid instability of the hyperbolic tangent velocity profile. *Journal of Fluid Mechanics*, 19:543–556, 1964.

[94] R. W. Metcalfe, S. A. Orszag, M. E. Brachet, S. Menon, and J. J Riley. Secondary instability of a temporally growing mixing layer. *Journal of Fluid Mechanics*, 184:207–243, 1987.

[95] R.D. Moser and M. M. Rogers. The three-dimensional evolution of a plane mixing layer: pairing and transition to turbulence. *Journal of Fluid Mechanics*, 247:275–320, 1993.

[96] W. Ling, J. Chung, T. R. Troutt, and C. T. Crowe. Direct numerical simulation of a three-dimensional temporal mixing layer with particle dispersion. *Journal of Fluid Mechanics*, 358:61–85, 1998.

[97] G. L. Brown and A. Roshko. On density effects and large structure in turbulent mixing layers. *Journal of Fluid Mechanics*, 64:775–816, 1974.

[98] J. H. Bell and R. D. Mehta. Development of a Two-Stream Mixing Layer from Tripped and Untripped Boundary Layers. *AIAA Journal*, 28:2034–2042, 1990.

[99] M. M. Rogers and R. D. Moser. Direct simulation of a self-similar turbulent mixing layer. *Physics of Fluids*, 6:903–923, 1994.

[100] A. W. Vreman, N. D. Sandham, and K. H. Luo. Compressible mixing layer growth rate and turbulent characteristics. *Journal of Fluid Mechanics*, 320:235–258, 1996.

[101] G. L. Dimotakis and G. L. Brown. The mixing layer at high Reynolds number: large-structure dynamics and entrainment. *Journal of Fluid Mechanics*, 78:535–560, 1976.

[102] E. Balaras, U. Piomelli, and J. M. Wallace. Self-similar states in turbulent mixing layers. *Journal of Fluid Mechanics*, 446:1–24, 2001.

[103] B. Vreman, B. Geurts, and H. Kuerten. Large-eddy simulation of the turbulent mixing layers. *Journal of Fluid Mechanics*, 339:357–390, 1997.

[104] K. Kemenov and S. Menon. Two level simulation of high-Re number non-homogeneous turbulent flows. *AIAA paper 2003-0084*, 2003.

[105] T. Wei and W.W. Willmarth. Reynolds-number effects on the structure of a turbulent channel flow. *Journal of Fluid Mechanics*, 204:57, 1989.

[106] R. B. Dean. Reynolds number dependence of skin friction and other bulk flow variables in two-dimensional rectangular duct flow. *Journal of Fluids Engineering*, 100:215–228, 1978.

[107] M. Germano, U. Piomelli, P. Moin, and W. H. Cabot. A dynamic subgrid-scale eddy viscosity model. *Physics of Fluids A*, 3(11):1760–1765, 1991.

[108] W.-W. Kim and S. Menon. An unsteady incompressible navier-stokes solver for large-eddy simulation of turbulent flows. *International Journal of Numerical Fluid Mechanics*, 31:983–1017, 1999.

[109] T. Persson, M. Liefvendahl, R.E. Bensow, and C. Fureby. Numerical investigation of the flow over an axisymmetric hill using les, des, and rans. *Journal of Turbulence*, 7(4):1–17, 2006.